INDOOR OPTICAL WIRELESS SYSTEMS WITH RELAY NODES

Yu Zeng

Submitted in accordance with the requirements for the degree of

Doctor of Philosophy

The University of Leeds

School of Electronic and Electrical Engineering

November 2023

The candidate confirms that the work submitted is his own, except where work which has formed part of jointly-authored publications has been included. The contribution of the candidate and the other authors to this work has been explicitly indicated below. The candidate confirms that appropriate credit has been given within the thesis where reference has been made to the work of others.

Chapter 4 and **Chapter 5** are based on the work from:

Y. Zeng, S. H. Mohamed, T. E. H. El-Gorashi and J. M. H. Elmirghani, "Delay Adaptation Method for Relay Assisted Optical Wireless Systems," 2020 22nd International Conference on Transparent Optical Networks (ICTON), 2020.

This paper has been published jointly with my PhD supervisor Prof. Jaafar Elmirghani, my co-supervisor Dr Taisir Elgorashi and Dr Sanaa Mohamed. Prof. Elmirghani proposed the work and revised the paper. I generated the simulation environments and the results and prepared the paper. Dr Elgorashi and Dr Mohamed revised the work and the paper.

Yu Zeng, Sanaa H. Mohamed, Ahmad Qidan, Taisir E.H. El-Gorashi and Jaafar M.H. Elmirghani, “Optimizing the locations and density of different relay terminals in relay-assisted OWC systems” to be submitted to IEEE Access.

This paper has been prepared jointly with my PhD supervisor Prof. Jaafar Elmirghani, my co-supervisor Dr Taisir Elgorashi, Dr Sanaa Mohamed and Dr Ahmad Qidan. Prof. Elmirghani proposed the work and revised the paper. I generated the simulation environments, developed the optimization model, generated the results and prepared the paper. Dr Elgorashi, Dr Mohamed and Dr Qidan revised the work and the paper.

Chapter 6 is based on the work from:

Y. Zeng, S. H. Mohamed, Ahmad Qidan, T. E. H. El-Gorashi and J. M. H. Elmirghani, "multiuser beam steering OWC system based on NOMA," IEEE International Conference on Transparent Optical Networks (ICTON) 2023.

This paper has been prepared jointly with my PhD supervisor Prof. Jaafar Elmirghani, my co-supervisor Dr Taisir Elgorashi, Dr Sanaa Mohamed, and Dr Ahmad Qidan. Prof. Elmirghani proposed the work and revised the paper. I studied the new idea of applying NOMA to beam steering OWC systems and completed the simulation environment and results. Dr Elgorashi, Dr Mohamed and Dr Ahmad Qidan revised the work and the paper.

Y. Zeng, S. H. Mohamed, Ahmad Qidan, T. E. H. El-Gorashi and J. M. H. Elmirghani, “Relay Assisted multiuser OWC system with Human Blockage " IEEE International Conference on Transparent Optical Networks (ICTON) 2023.

This paper has been prepared jointly with my PhD supervisor Prof. Jaafar Elmirghani, my co-supervisor Dr Taisir Elgorashi, Dr Sanaa Mohamed, and Dr Ahmad Qidan. Prof. Elmirghani proposed the work and revised the paper. I worked on the simulation environment for human blockage, generated the simulation results and prepared the paper. Dr Elgorashi, Dr Mohamed and Dr Ahmad Qidan revised the work and the paper.

Acknowledgments

This thesis presented here could not have been achieved without the help and encouragement of my supervisors, Professor Jaafar Elmirghani and co-supervisor Dr Taisir Elgorashi. I am grateful for their teaching, guidance and friendship. I would like to thank all my colleagues in the Communication Systems and Networks group at University of Leeds, especially Dr Sanaa Mohamed. Her guidance, encouragement and inspiration are an indispensable part for completing this thesis. I feel very honoured to have had the chance to work with them. Finally, I would like to express my deepest gratitude to my parents and my wife Qing Qing Wan, for their love, patience, and encouragement.

Abstract

Optical wireless communication (OWC) systems are proposed as candidates for future indoor communication systems as they offer a number of advantages over radio frequency wireless communication systems. However, OWC systems face challenges including background noise, multipath propagation, and signal blockage.

This thesis investigates deploying relay terminals, beam steering technology and Non-orthogonal Multiple Access (NOMA) technology in single-user and multi-user OWC systems. Firstly, we consider a single-user OWC system with Infrared APs and introduce optoelectronic (O-E-O) amplify-and-forward. Here we introduce Semiconductor Optical Amplifier (SOA) amplify-and-forward and decode-and-forward relay terminals. A novel delay adaptation method is proposed to balance the signals arrival time of multiple relay terminals and hence reduce the delay spread of the received signal. Secondly, to find the best relay terminal deployment scheme, an Optimum Relay Terminal Allocation (ORTA) method based on Mixed Integer Linear programming (MILP) is proposed. The best downlink and uplink Signal-to-noise (SNR) results of the ORTA method are on average 19% and 127%, respectively better than fixed non-optimum relay terminal deployment schemes.

Finally, we investigate the use of beam steering technology to reduce the impact of multipath dispersion and improve the SNR of users. The proposed beam steering OWC system is applied in a multi-user environment based on NOMA technology. Relay terminal deployment is investigated to reduce the influence of signal blockage. The results show that the outage probability of relay-based cooperative communication mode is two orders of magnitude lower than direct communication on average.

Table of Contents

List of Figures

List of Tables

Abbreviations

ADM	Add and Drop Multiplexer
AF	Amplify-and-Forward
AM	Angle Magnifier
AP	Access Point
APDs	Avalanche Photodiodes
BER	Bit Error Rate
CDMA	Code Division Multiple Access
CDS	Conventional Diffuse System
CGH	Computer Generated Hologram
CNN	Convolutional Neural Network
CPC	Compound Parabolic Concentrator
CSI	channel state information
CSMA	carrier sense multiple access
DCO-OFDM	Direct Current biased Optical-OFDM
DF	Decode-and-Forward
DFB	Distributed Feedback
DMT	Discrete Multitone
EA	Evolutionary Algorithms
EGC	Equal Gain Combining.
FOV	Field Of View
FTTH	Fibre To The Home
FZP	Fresnel Zone Plate
GRPA	Gain Ratio Power Allocation
IM/DD	Intensity Modulation and Direct Detection
IoT	Internet of Things
IRC	Infrared communication
ISI	Inter Symbol Interference
LD	Laser Diode

LED	Light Emitting Diode
LiFi	Light-fidelity
LOS	Line-Of-Sight
LSMS	Line Strip Multi-beam System
MEMS	Micro-Electro-Mechanical System
MILP	Mixed Integer Linear Programming
MRC	Maximum Ratio Combining
NLOS	Non-Line Of Sight
NRZ-OOK	Non-Return to Zero-OOK
O-E-O	Optoelectronic
OFDM	Orthogonal Frequency Division Multiplexing
OFDMA	Orthogonal Frequency Division Multiple Access
OOK	On-Off Keying
ORTA	Optimum Relay Terminal Allocation
OWC	Optical Wireless Communication
PAM	Pulse Amplitude Modulation
PFDR	Pyramidal Fly-eye Diversity Receiver
PIM	Pulse Interval Modulation
PIN	Positive-Intrinsic-Negative
PIN-BJT	Positive-Intrinsic Negative-Bipolar Junction Transistor
PPM	Pulse Position Modulation
PWM	Pulse Width Modulation
RCE-PD	Resonant Cavity-Enhanced Photoelectric Detector
RFC	Radio Frequency Communication
RGB-LDs	Red-Green-Blue Light Diodes
RIS	Reconfigurable Intelligent Surface
RMS	Root-Mean-Square
RWP	Random Way Point
SCM	Subcarrier Modulation
SIC	Successive Interference Cancellation
SINR	Signal-to-Interference and Noise Ratio

SNR	Signal to Noise Ratio
SL-APD	Super lattice Avalanche Photodiode
SLM	Spatial Light Modulator
SOA	Semiconductor Optical Amplifier
TDMA	Time Division Multiple Access
VCSEL	Vertical-Cavity Surface-Emitting Laser
VLC	Visible Light Communication
WFOV	Wide-Field-of-View
WGPD	Waveguide Photodetector

Chapter 1: Introduction

1.1 The Advent of Indoor Optical Wireless System

In the last decade, the demand for wireless communication has grown exponentially. The data intensive applications of smartphone, laptop and IoT Internet of Things (IoT) devices were the major sources of wireless communication growing demands [1]. According to Cisco, Internet users are predicted to grow from 3.9 billion users in 2018 to 5.3 billion users by 2023 [2]. With this constant exponential increase in wireless network traffic, conventional Radio Frequency Communication (RFC) system including 4G networks, 5G networks and Wireless Fidelity (WiFi) may not be able to meet future traffic demands due to scarce radio spectrum resources. Numerous technologies, such as Multiple Input and Multiple Output (MIMO), advanced modulation and multiple access, and adaptive antennas were proposed to expand the capacity of current RFC system [3], [4]. However, given that the future data rates will be in the range of Tbps, the research efforts are being shifted towards exploiting the free spectrum bands beyond the millimetre waves [5]-[7]. The optical band in the electromagnetic spectrum has the potential to provide huge bandwidth. Therefore, Optical Wireless Communication (OWC) systems have received extensive attention. In addition to the huge bandwidth, OWC systems offer other advantages including energy efficiency, low start-up cost, low operational costs and improved security.

Indoor wireless communication is a major application of OWC. In current indoor OWC system, visible light and infrared are leveraged as the prevalent communication medium [8]. Light Fidelity (LiFi), as a representative of OWC systems, encompasses a broader research field that goes beyond visible light communication (VLC) immediate applications. LiFi based on VLC use Light Emitting Diode (LED) to realise fully networked wireless systems [9]. The study of LiFi involves various aspects such as networking and protocols, interference mitigation and security, media access control protocols, link level algorithms, channel models, and device and component deployment for VLC systems [9]. Compared with conventional indoor RFC systems, indoor OWC systems provide many favourable properties. The implementation and operational cost

of indoor OWC are evidently lower than traditional RFC system [10]-[13]. Inheriting the transmitter (LED or LD) and detectors of optical fibre communication, indoor OWC infrastructures can be integrated with current Fibre To The Home (FTTH) systems. Due to the impenetrability of light, channels in neighbouring rooms are immune to interference in indoor OWC systems [14]-[17]. This feature of OWC brings the possibility of channel reuse in different rooms in a building, improving the usage efficiency of the optical spectrum [18], [19].

Conventional Diffuse Systems (CDSs) are typical infrared OWC systems. A CDS consists of a diffuse LED/LD as the transmitter and a wide Field of view (FOV) photodetector as the receiver [18], [19]. The FOV of OWC system indicates the extent of the monitored area or the range over which the photodetector can detect optical signal. CDS system faces several challenges that need to be addressed for its widespread adoption and implementation. Some of these challenges include:

(1) In CDS, the signal dispersion caused by multipath propagation and reflections results in signal spread, leading to therefore inter symbol interference (ISI) [17]-[21].

(2) Photon diode of the OWC photodetector is sensitive to the spectrum of the sunlight and artificial light, such as fluorescent lamp, incandescent lighting and other solid-state light source. They are considered as the major background noise sources in indoor OWC systems.

(3) The diffraction ability of OWC system is weaker than that of RFC system. The Shadowing and blockage due to furniture and humans moving in the room may result in communication outage.

(4) The transmitted optical power is restricted by eyes and skin safety regulations for infrared communication (IRC) [20], [21].

Relay-based communication, widely used in RFC systems to improve the channel, is also proposed for the use in OWC systems. In this thesis, we focus on the use of relay technologies to solve the drawbacks of indoor OWC systems. The impact of the type, location and number of relay terminals is evaluated. We also address integrating relay

technologies with other technologies including Non-orthogonal Multiple Access (NOMA) and beam steering to enable multi-user indoor OWC systems that support mobility.

1.2 Research Objectives

The aim of the work in this thesis is to overcome some of the drawbacks of indoor OWC system via optimising the deployment of relay terminals and designing a beam steering multi-user indoor OWC system that supports mobility. The main objectives are as follows:

1. To investigate the impact of the type, number and location of relay terminals on the performance of an indoor CDS OWC system.
2. To optimise the location and type of relay terminals in an indoor CDS OWC system.
3. To investigate the use of beam steering based on spatial light modulators for downlink communication to reduce the ISI in an OWC system.
4. To study the use of Non-orthogonal Multiple Access (NOMA) technology to achieve multiuser access in a beam steering OWC system.
5. To study the use of relay terminals to reduce the influence of the signal blockage due to moving humans in a multiuser indoor OWC system based on NOMA.

1.3 Original Contributions

The author in this thesis has:

1. Modelled and analysed the characteristics of the indoor optical wireless channel by developing a ray-tracing algorithm that considers direct line-of-sight (LOS) (Lambertian and Gaussian light source) and first and second order reflections (Lambertian reflection). The outputs of the ray tracing algorithm are the channel impulse response, the delay spread, signal-to-noise ratio (SNR), signal-to-interference and noise ratio (SINR) and the outage probability. The ray tracing algorithm is also used to evaluate the background noise due to artificial light sources.

2. Verified the performance of the ray tracing algorithm by comparing its results to results of basic OWC systems in the literature including CDS and Line Strip Multi-beam System (LSMS).
3. Investigated the characteristics and performance of three different types of relay terminals including Optoelectronic (O-E-O) amplify-and-forward relay terminals, Semiconductor Optical Amplifier (SOA) amplify-and-forward relay terminals and Decode-and-Forward (DF) relay terminals.
4. Applied a delay adaptation method to balance the signal arrival time at relay terminals.
5. Proposed an Optimum Relay Terminal Allocation (ORTA) method based on a comprehensive MILP model to optimise the location and type of relay terminals at the side walls and ceiling in a CDS system. The SNR results of the ORTA method are compared with fixed relay terminals allocation schemes and with a system without relay terminals.
6. Proposed the use of NOMA to achieve multiuser access in a beam steering OWC system and investigated the influence of varying power allocation factor on SINR and Bit Error Rate (BER) of this system.
7. Proposed a relay assisted NOMA beam steering system to design a multi-user OWC system to reduce the blockage due to moving humans and demonstrated the reduced outage probability of this system.

1.4 Related Publications

The work in this thesis resulted in the following journals and conference papers:

1. Y. Zeng, S. H. Mohamed, T. E. H. El-Gorashi and J. M. H. Elmirghani, "Delay Adaptation Method for Relay Assisted Optical Wireless Systems," 2020 22nd IEEE International Conference on Transparent Optical Networks (ICTON), 2020.
2. Yu Zeng, Sanaa H. Mohamed, Ahmad Qidan, Taisir E.H. El-Gorashi and Jaafar M.H. Elmirghani, "Optimizing the locations and density of different relay terminals in relay-assisted OWC systems" to be submitted to IEEE Access.

3. Y. Zeng, S. H. Mohamed, Ahmad Qidan, T. E. H. El-Gorashi and J. M. H. Elmirghani, "Multiuser Beam Steering OWC System based on NOMA," 23rd International Conference on Transparent Optical Networks (ICTON), 2023
4. Y. Zeng, S. H. Mohamed, Ahmad Qidan, T. E. H. El-Gorashi and J. M. H. Elmirghani, “Relay Assisted Multiuser OWC system under Human Blockage, " 23rd International Conference on Transparent Optical Networks (ICTON), 2023.

1.5 Thesis Organisation

This thesis is organised as follows: Chapter 2 presents a review of OWC systems. The review covers the transmitter and receiver components and modulation and multi access technologies. Moreover, the design challenges of indoor OWC systems, such as optical safety regulations, ambient noise, multi-path dispersion and blockage due to human movement in the room are outlined.

Chapter 3 presents the tools that are used to model and simulate the OWC channel in an indoor environment including Lambertian and Gaussian light beam models. The ray tracing model for simulating the impulse response is introduced. Background noise is explained. The SNR, root mean square (RMS) delay spread, and outage probability evaluations are presented and used to analyse the impact of ambient noise on the indoor OWC system’s performance.

Chapter 4 introduces the characteristics and the structures of three different types of relay terminals including O-E-O amplify-and-forward relay terminal, SOA amplify-and-forward relay terminal and decode-and-forward relay terminal. These three different typess of relay terminals are applied in different CDS systems. To balance the signal arrival time of different relay terminals, a delay adaptation method is proposed. The performance of different relay terminal deployment schemes in a CDS system in terms of SNR is investigated and compared with the CDS system without relay terminals.

Chapter 5 introduces an Optimum Relay Terminal Allocation (ORTA) method based on a MILP model to optimise the location of relay terminals placed at serval locations at the side walls and ceiling under several scenarios in the CDS system. The SNR results

of the ORTA method are compared with fixed relay terminals communication schemes and to a system without relay terminals.

Chapter 6 introduces the use of beam steering based on the spatial light modulator and phased Fresnel plate in the relay assisted in the OWC system. A beam steering multi-user OWC system based on NOMA is proposed. The influence of varying the power allocation factor on the SINR and BER of this system is investigated. Considering the blockage due to human movement, a relay terminal assisted communication method is introduced to reduce the outage probability of this system.

The thesis is finally concluded in Chapter 7 where the major contributions of this work are presented, and the future directions are discussed.

Chapter 2: Review of OWC Systems

2.1 Introduction

Using light for communication is not a new concept. Hundreds of years ago, fire, smoke, mirrors and semaphore were used by our ancestors to send signals. Due to the high frequency of the optical band in the electromagnetic spectrum, the optical signals experience high path loss as the path loss increases as the frequency increases according to Friis free space formulation ($path\ loss \propto f^2$). The path loss is influenced by the territorial shadowing and impediments [22]. Therefore, modern OWC systems are typically suitable candidates to provide the last mile connectivity in mobile access networks where the distance between the transmitter and the receiver is considered to be short-range, and where the optical beams can be focused, longer distances can be achieved. Modern OWC research started in the 1960s with the advent of laser technology. However due to the low efficiency and high cost of optical devices at the time, OWC research has not attracted extensive attention and deployment. Until the 1990s, with the fabrication process improvement of solid luminescent material and semiconductors, the luminous and light perception efficiency of OWC devices witnessed significant growth and reduction in deployment costs [23].

In this chapter, we will review the characteristics of OWC systems and present the components and modulation techniques as well as the challenges of OWC systems. Section 2.2 gives an overview of indoor OWC systems. In Section 2.3, the merits and limitations of different types of OWC transmitters are discussed. The structure and materials of different types of OWC receivers are reviewed in Section 2.4. The modulation techniques and the challenges including ambient light noise, ISI, and human blockage of OWC systems are discussed in Section 2.5 and Section 2.6, respectively. Finally, the chapter is summarised in Section 2.7.

2.2 Indoor OWC systems

Fig. 2-1 shows the block diagram of a basic OWC indoor system. This system mainly consists of the transmitter, propagation medium (free-space) and the receiver. At the transmitter, the input data is converted into a digital signal and used to modulate one of the parameters of the optical signal such as the amplitude of the optical signal generated by a suitable light source (LED or LD). The main difference between LED and LD is the lighting principle.

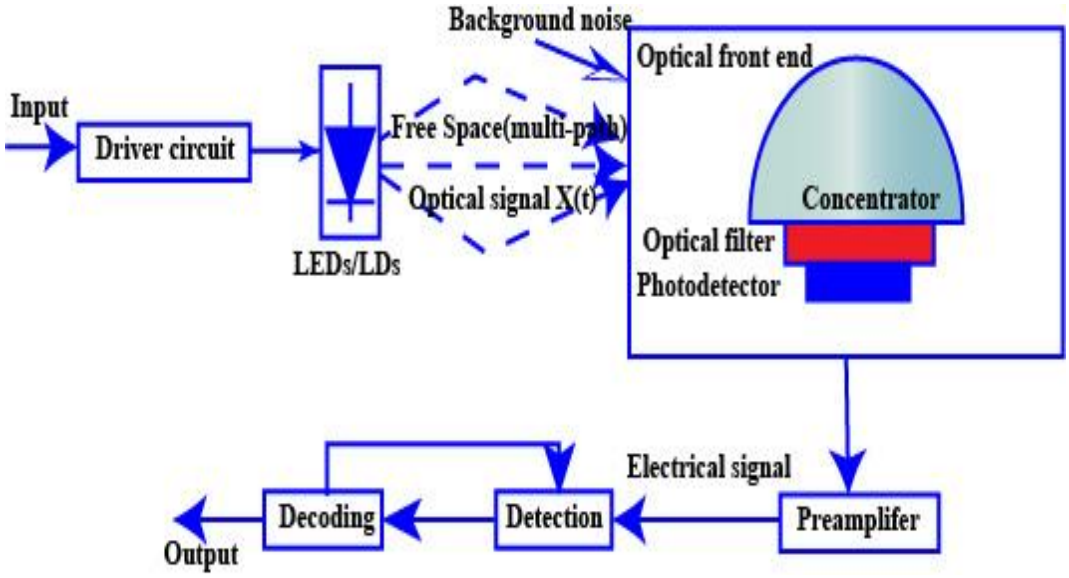

Figure 2- 1 An indoor OWC system block diagram.

The light emitted by a LD is coherent while the light emitted by an LED is incoherent. The optical signal travels through the free-space and is collected by photodetectors (Positive-Intrinsic-Negative (PIN) photodiodes or Avalanche Photodiodes (APDs)) which are the core component of the receiver. An optical signal is converted into electrical signal by the photodetector and is amplified before detection. The receiver usually includes a concentrator and an optical filter to increase the Field Of View (FOV) and mitigate the ambient noise. Intensity Modulation and Direct Detection (IM/DD) is used in the most of OWC systems due to its reduced cost and complexity [24], [25]. IM can be achieved by varying the LED or LD bias current. To avoid transmitter flickering especially for transmitters working in the visible spectrum, an extra bias current is required to ensure that the LED or LD is working on the positive area [26].

In addition to the light source, most OWC transmitters include an optical telescope (for long distance) [11], an optical diffuser (for mobile short distance) and other optical systems (Optical lens, Spatial Light Modulator (SLM) or Micro-Electro-Mechanical System (MEMS) [22] that steers the beam before propagation into the channel.

Atmospheric loss along the propagation path has a significant impact on the link budget for an OWC system [26], [28]. While the environmental degradation (i.e., fog, mist, clouds, particulate matter, etc.) is not considered in an indoor environment, indoor OWC systems still suffer from free-space loss. Free-space loss refers to the amount of transmitted power that is lost due to propagation through space or not captured by the receiver. The average free space loss for a point-to-point indoor OWC system operating with a slightly diverging beam is around 20dB whereas the average free-space loss for an indoor OWC system employing a wide beam angle is 40dB or more [27], [28].

To improve the channel between the transmitter and the receiver, active devices (i.e., devices that require several electronic components) such as relays (including amplify-and-forward (AF) and decode-and-forward (DF)) [26] and passive (devices that require minimal electronic components) such as reconfigurable intelligent surface (RIS) [27] nodes were proposed.

2.3 The classification and the structure of light sources in OWC systems

Table 2-1 compares typical transmitters used in Infrared Communication (IRC) with typical transmitters used in VLC.

Table 2- 1 Comparison between IRC and VLC [23]

Transmitter type	VLC	IRC
Reach	Short-medium (few meters) LoS expected.	Short-medium (<10 m) LoS expected.
Energy	High (Watts); Illumination	Low (<10 mW) on demand

consumption	needs to be on.	only.
Bandwidth	400nm-700nm 320THz	S-C-L 1460–1625 nm 20.9 THz or 780nm to 950 nm 70 THz
Safety	Penetrate eyes safely if collimated:<1 mW Flicker may be observed by eye.	Not safe to penetrate eyes if collimated:<10 mW No flicker may be observed by eye.
Privacy	Medium Contained by walls and ceiling. May leak through the windows and doors.	High Contained by walls and ceiling. IR reflection coating can prevent signal leaking from the window.
Infrastructure	Share with illumination infrastructure.	Extra infrastructure is needed.

VLC transmitters reuse the indoor ubiquitous lighting infrastructure. With the improvement in the fabrication process of solid luminescent material and semiconductors, the illuminous intensity and efficiency of LED and LD are constantly improving, almost substituting traditional fluorescent lamp and incandescent lighting. However, to guarantee the normal operation of illumination as well as communication, VLC transmitters as well as LEDs for LiFi require extra dimming control, flicker mitigating and chromaticity control. This results in the need for a complex structure and control algorithm which impairs the reuse advantage of the VLC transmitter. In the following chapters, we focus on IR OWC systems to avoid the extra structure for dimming control, flicker mitigating and chromaticity control.

In the following we will review the two types of light sources used in OWC systems.

2.3.1 LEDs

The core structure of an LED is the PN conjunction between P-type Semiconductor and N-type Semiconductor [29]. The electronic excitation is achieved by applying a forward bias voltage across the p–n junction. This excitation energises electrons within the material into an 'excited' state which is unstable. When the energised electrons return to the stable state in a process known as radiative recombination, they release energy spontaneously and this energy is given in the form of photons. The radiated photons could be in the UV, visible or IR part of the electromagnetic spectrum depending on the energy band-gap of the semiconductor material. Alternatively, nonradiative recombination occurs when the falling electron only gives out phonons (heat) and not photons. The external efficiency η measures the LED photoelectric efficiency. It is defined as [25], [29]:

$$\eta = \frac{No.\ of\ photons\ emitted\ externally}{No.\ of\ carrier\ passing\ the\ junction} \tag{2-1}$$

Based on the geometry and external efficiency of LEDs, they can be categorised as planar, dome and edge emitting LED as shown in Fig. 2-2 (a), (b) and (c). The planar LED is the typical LED structure which emits light from all surfaces and the emission is referred as typical Lambertian radiation. The incident energy of a Lambertian point source uniformly radiate in all directions within the hemisphere [25]. Compared with planar LED, the geometry of the dome LED possesses much larger recombination area. It provides a greater effective emission area which improves the external efficiency of the dome LED. Fig. 2-2(c) shows the geometry of a double heterojunction AlGaAs edge-emitting LED [29]. The edge-emitting LED confines the light in a thin narrow stripe in the plane of the $p{-}n$ junction. It results in a high external efficiency and narrow beam divergency (half power angle =30 degrees) [30].

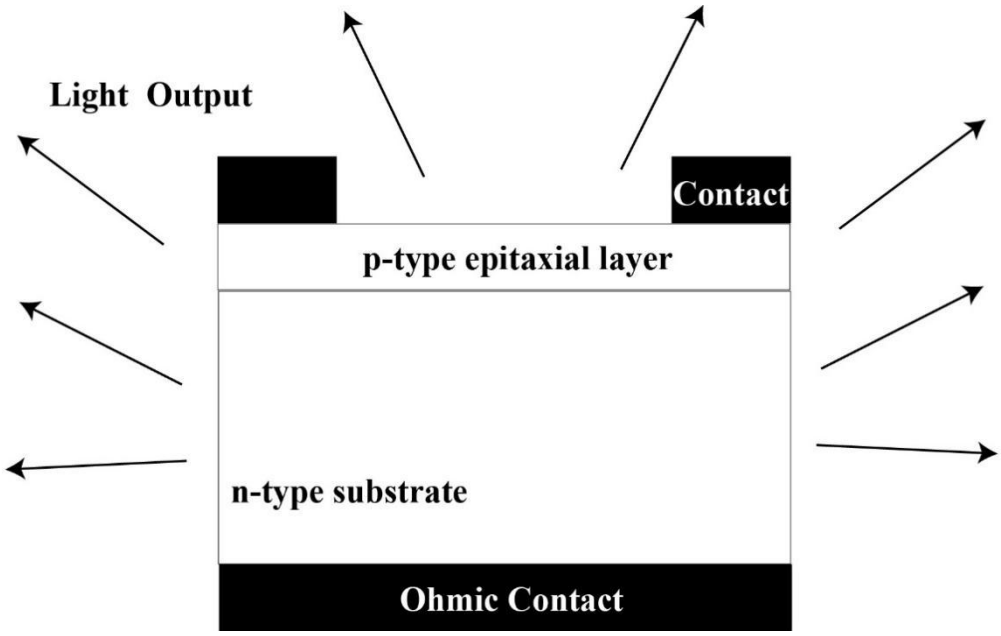

(a) Planar LED

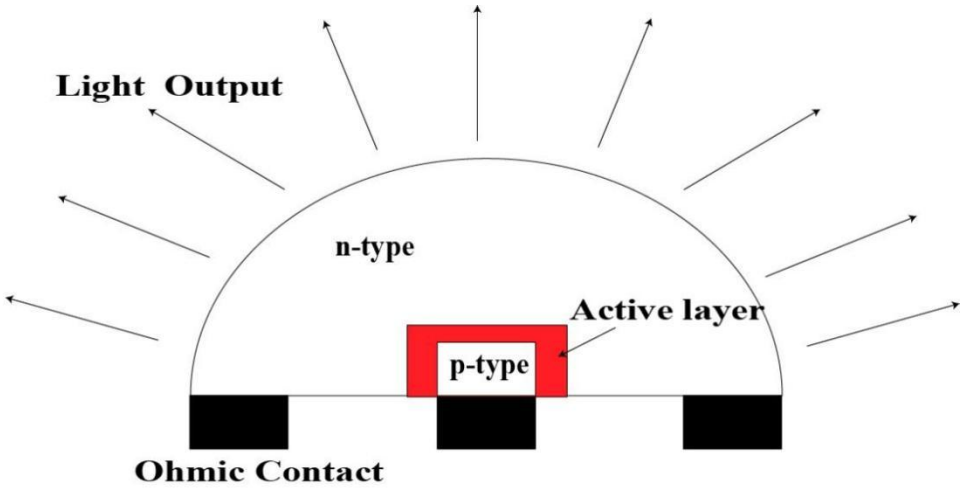

(b) Dome LED

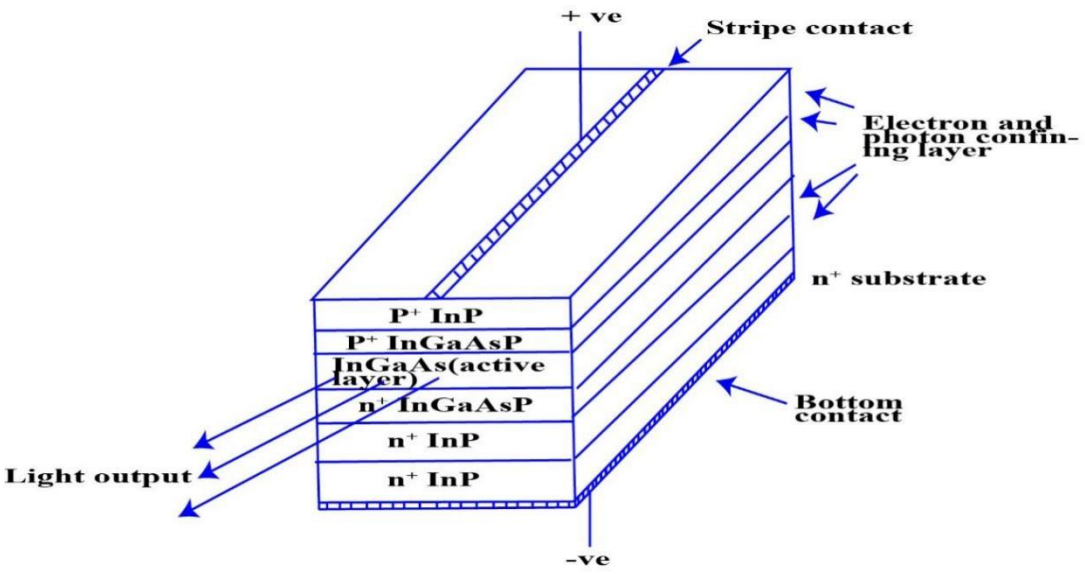

(c) Edge emitting led [44]

Figure 2- 2 PLANAR, dome and edge emitting LED [44].

The inherent modulation bandwidth of an LED is essentially limited by the minority carrier lifetime [32], [33]. One way to reduce carrier lifetime and increase the modulation bandwidth of the LED is to increase the doping level of LEDs. However, increasing the doping level results in excessive nonradiative recombination that degrades the external efficiency level of LED [33]-[35]. The second approach is to increase the carrier density [36]. LD have considerably higher modulation bandwidth because the radiative lifetime is further shortened by the stimulated emission process [37], [38].

2.3.2 LD

Stimulated emission is the core of LD operation [39]. An external incident signal with energy ($hv = E2 - E1$) will force the atom in the upper level $E2$ to transit to the lower level $E1$. The change in energy involved in this process is emitted as a photon that has the same phase and frequency as the incident (exciting) photon. Therefore, stimulated emission is coherent. The light emitted by a LD is the result of stimulated emission. The rise time of LED is in accordance to the inherent spontaneous emission lifetime of relevant material, while the rise time of LD is proportional to the stimulated radiation lifetime. Therefore, LD prevails over LED on the response time and

modulation bandwidth as well as in providing narrow beam divergency [25]. However, the potential health hazard, high cost, narrow spectral emission linewidth (for VLC) and colour mix complexity (for VLC) are limitations of using LD as the OWC transmitter [40], [41].

There are three common structures of LDs. The first structure is the Fabry–Perot laser (FPL). The essential feature of FPL is a resonating cavity. The cavity mirrors are formed by the boundary between the high refractive index semiconductor crystal and the lower refractive index air. FPL faces an undesirable problem called mode-hopping. It happens as the refractive index changes with temperature, and this results in changing the central wavelength. The second structure is the distributed feedback (DFB) laser which is a special type of edge-emitting lasers optimised for single-mode (single-frequency) operation [25]. The single-mode operation is achieved by incorporating a periodic structure or a Bragg grating near the active layer to reflect the desire wavelength in the active region. This results in an extremely narrow spectrum for the DFB laser. The third structure is the vertical-cavity surface-emitting laser (VCSEL). VCSEL is not an edging emitting laser. The resonant cavity is vertical and perpendicular to the active layer [25]. Above and below the active layer, in the vertical direction, are narrow band mirror layers and the light beam emerges from the surface of the wafer. VCSELs have been widely used in optical fibre and OWC systems due to their stability and low cost.

2.4 The classification and the structure of receivers in OWC systems

The optical signal travelling through the free-space channel is converted back to an electrical signal by the optical receiver. The optical receivers of VLC and IRC systems have similar structure. A typical optical receiver comprises of a pre-amplifier circuit and photodetector with an optical concentrator and optical filter [34]. The structure of the receiver is depicted in Fig.2-3. The main function of the optical front end is enhancing the collected signals power and mitigating the ambient light influence. For an IM/DD OWC system, the optical signal from the transmitter is captured by the pre-processing of the optical front end. The arriving optical pulse, which represents logic 1 or 0, is

converted to electric current by a photodetector. Then, the electrical signal is amplified by a pre-amplifier circuit and is detected by a clock driven detection system.

In the following we will look into the different components of the receiver:

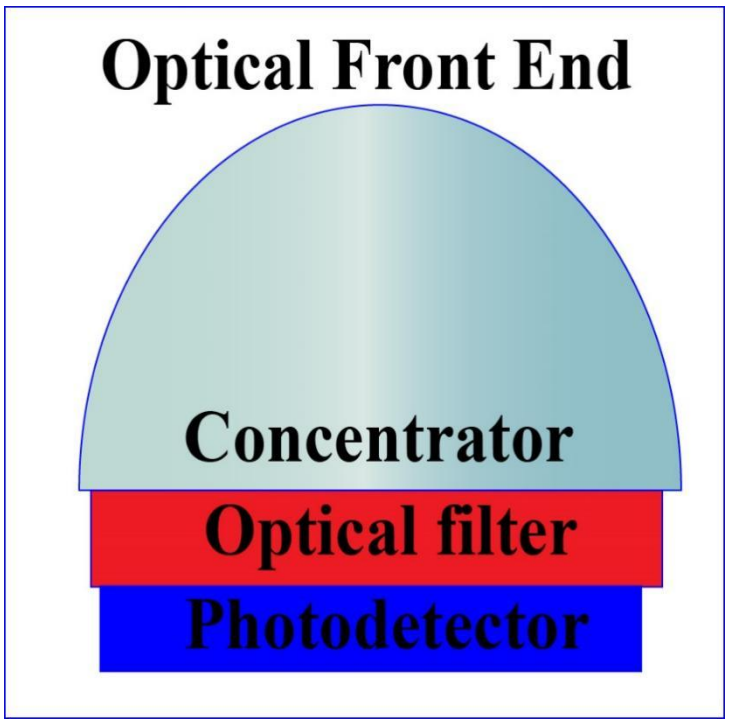

Figure 2- 3 Typical receiver structure of VLC systems.

2.4.1 Concentrator and optical filter

In the optical receiver design, a large detection area can maximise the collected power. However, the huge increase in capacitance and extra noise (background noise and f^2 noise) as a result of the larger photodetection area makes it act as a low pass filter which restricts the data rate of optical receivers [42], [43]. Therefore, a relatively small photodetector coupled with a concentrator to guarantee enough optical power is proposed in [42]. The small photodetector improves the receiver's sensitivity. The decreasing receiver capacitance leads to reduced noise current and improved receiver sensitivity [44].

Concentrators used in IRC and VLC receivers can be categorised into non-imaging concentrators and imaging concentrators [25]. Imaging concentrators keep the spatial

information of light signals from different transmitters, while non-imaging concentrators focus on receiving more signal power without isolating the signals from different transmitters. Non-imaging receivers are commonly used in OWC systems [45]-[47]. There are two typical non-imaging concentrators which are extensively adopted in OWC systems. The first structure is a non-directional hemispherical lens [48]. Its structure is given in Fig. 2-3. The advantages of the non-directional hemispherical lens include ultra-wide FOV and omni-directional receiving, hence, it is ideal for non-line of sight (NLOS) OWC systems and can be adopted in commercial IRC receivers [49]. The second typical non-imaging concentrator structure is the compound parabolic concentrator (CPC). It has better gain compared with hemispherical lenses, however, its FOV is reduced. The concentrator gain of CPC ($FOV < 90°$) approachs the maximum gain of an ideal concentrator [50]. To make the best use of the advantages and avoid the disadvantages, CPC is usually integrated with narrow band pass filter to effectively mitigate the power of the ambient noise and enhance the power of the desired signal. Therefore, CPC is ideal for LOS-link OWC systems.

Compared with non-imaging concentrator, the imaging concentrator retains the spatial information of the incident radiation and focuses an image of the light source to the photon detector. It is usually adopted in imaging receiver and MIMO VLC system which needs specific spatial information of the incident radiation [50]. In [52], [53], a hemispherical imaging concentrator is compared with convex-lens concentrator based on imaging MIMO VLC system. Hemispherical imaging receiver has a larger FOV and better performance in separating the signals from different LEDs as reported in [51].

As mentioned above, the concentrator collects the incident optical signal as well as the background ambient light noise. For a complete receiver, the main function of an optical filter in OWC systems is mitigating the ambient light. The spectral power density of the main source of ambient light is depicted in Fig. 2-4. The primary proportion of ambient light power is concentrated on the relative low band in the spectrum. Therefore, high pass filter and band pass filter are two main optical components adopted in OWC systems [44]. A high pass filter is commonly made of coloured glass and plastic. The optical characteristics of the high pass filter are related

to the material and structure and are independent of the incident angle. A high pass filter is deposited between the concentrator and the photodetector. Commercial IRC systems usually use high pass filters.

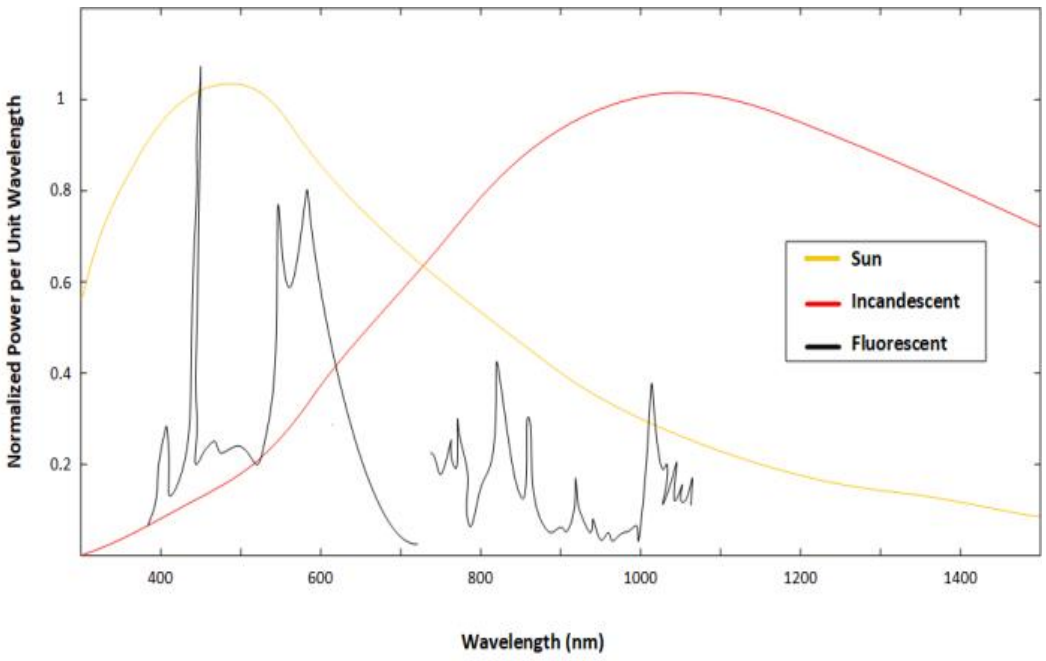

Figure 2- 4 The power spectral density of the main sources of ambient light [1].

Compared with high pass filters, band pass filters have a very narrow bandwidth ($\leq 1nm$) and are usually made of thin dielectric layer [44]. Based on optical interference, the band pass filter can achieve superior rejection of ambient light. Relatively, the main proportion of the spectral power of the transmitter needs to fit the narrow bandwidth of the band pass filter. Compared with LEDs, LDs have higher directivity and narrow spectral bandwidth and hence, adapt to the feature of the bandpass filter. In VLC systems with WDM, different receivers are deployed with suitable bandpass filters to mitigate the influence of co-channel interference [54].

2.4.2 Photodetector and preamplifier

The photodetector is the primary component of the receiver in OWC systems. The main function of the photodetector is to convert the optical signal into electrical current. An adequate photodetector should provide reliability, lightweight, robustness, and durability. PIN photodiodes and APDs are the typical photodiodes adopted in OWC

systems. Metal-Semiconductor-Metal Photodetector (MSM PD), Super Lattice Avalanche Photodiode (SL-APD), Waveguide Photodetector (WGPD) and Resonant Cavity-enhanced Photoelectric Detector (RCE-PD) are also adopted in some OWC systems. However, currently, almost all commercial IRC systems adopt ordinary PIN photodiodes due to the low cost, the simple structure, and the simpler biasing [55].

The PN conjunction of conventional photodiodes is integrated with a depletion area and a neutral area. Since the depletion area of conventional photodiodes is only several micrometres, most portion of the incident radiation is detected at the neutral area. This results in the degradation of photoelectric conversion efficiency, response time and quantum efficiency. In PIN photodiodes, an intrinsic component with low doping is deployed between the P-type and the N-type to increase the width of the depletion area. The wider the depletion area of the PIN photodiode, the more incident radiation they can capture. Also, decreasing the junction capacitance improves the response time of the photodiodes. Responsivity, R, measures the efficiency of photodiodes. The responsivity of PIN photodiodes is defined as follows [44]:

$$R = \frac{I_0}{P_0} = \frac{\eta e}{hf} \quad \left(\frac{A}{W}\right), \tag{2-2}$$

where η is the quantum efficiency of PIN photodiodes which depends on the structure and material of the detector, e represents the elementary charge, h is the Planck Constant and hf represents the energy of the photon. The responsivity of common PIN photodiodes is in the range of 0.5~0.6A/W [28]. Due to the influence of the material of PIN photodiodes on the quantum efficiency and responsivity, the spectrum of Si PIN photodiodes is from 0.5~0.9 um, while the adaptive spectrum of Ge and InGaAs PIN photodiodes is 1.3~1.6 um.

APDs are another photodetector type which is extensively adopted in OWC systems. APDs can be treated as a PIN photodiode operated with a high reverse bias [44]. With high reverse bias, the photon generated carrier in the depletion area acquires enough kinetic energy from the electrical field. Ionised collisions between energetic carrier and lattice produces a new electron-hole pair. This constant chain reaction, which results in

the advent of abundant electron-hole pairs and improves the internal electrical gain of APDs, is called the avalanche multiplication effect. Since the remarkable internal electrical gain of APDs can overcome the thermal noise produced by preamplifiers and improve the SNR, APDs are dominating in photon-sensitive OWC systems when the ambient light is weak [56]. When the ambient light dominates, the random nature of electrical internal gain of APDs increases of the shot noise more than the internal electrical gain [44]. The expression of APDs responsivity is similar to Equation 2-6. In an ideal environment, the responsivity of silicon APDs is 0.75 A/W within the 0.6~0.9 um wavelength band [57].

According to the structure of the OWC receiver, the optical signal is converted into a weak electrical signal by the photodetector. This weak electrical signal is undetectable for the electrical decision circuit. Therefore, a preamplifier is needed as an important component of the optical front end of the OWC receiver. The preamplifiers of OWC receivers are categorised into three different groups, low-impedance preamplifier, high-impedance preamplifier and trans-impedance preamplifier [44]. The low-impedance preamplifier is a simple voltage amplifier. To guarantee receiver bandwidth, the total input resistance is selected to be small. This structure results in the domination of thermal noise at the receiver and a relatively low receiver sensitivity. High-impedance preamplifier provides high sensitivity and low thermal noise while the high totally input resistance of the receiver limits the bandwidth of receiver. Therefore, high impedance preamplifiers are usually coupled with an equaliser which have greater attenuation for low frequency components. This can compensate the low bandwidth of the high impedance preamplifier.

To simplify the structure of the preamplifier and overcome the drawbacks of high-impedance, trans-impedance preamplifier consisting of a low noise high input impedance amplifier with negative feedback is used [29]. The main function of the negative feedback is to reduce the equivalent input resistance which creates a trade-off between the bandwidth and thermal noise. The noise level of the preamplifier can be reduced by using a Field Effect Transistor (FET) as an alternative front-end device instead of a bipolar-junction transistor (BJT) [29]. Conversely, BJT has better power efficiency compared to FET [29].

2.4.3 Wide FOV receiver, angle diversity receiver and imaging receiver

Wide FOV receiver was widely studied in CDS [58]. Since CDS is NLOS communication system, the FOV of CDS receiver is designed to be $180°$ to collect the signals reflected by the walls and ceiling. However, the wide FOV results in high ambient light noise. Moreover, reflected signals arrive at different times due to the difference in the distances between reflecting surfaces and the receiver. Therefore, systems with wide FOV receiver suffer from multipath dispersion and high ambient light noise. In [14] and [59], Al-Ghamdi investigated the FOV of the receiver to find the equilibrium point between signal power collected and mitigating the ambient light noise. The background noise is gradually reduced with decreasing the FOV. When the FOV of the receiver is smaller than $60°$, the optical power of the ambient light dramatically decreases as well as the collected optical power of the signal [59]. Therefore, varying the FOV of conventional receiver cannot solve the problem of time spread and low SNR. Angle diversity receiver is proposed to mitigate the influence of ambient light, improve the SNR, and reduce ISI [59]. Pyramidal Fly-eye Diversity Receiver (PFDR) is a typical angel diversity receiver [60]. The structure of PFDR is shown as in Fig. 2-5.

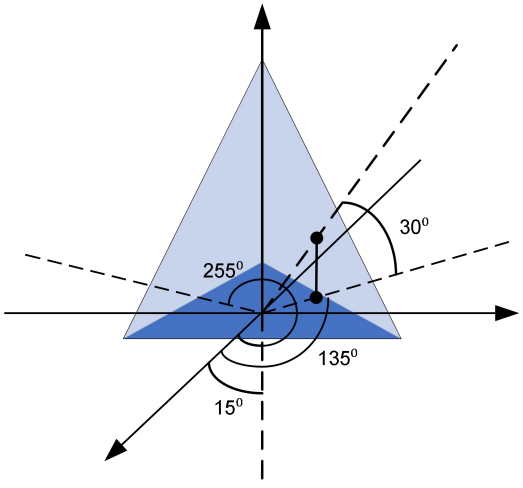

Figure 2- 5 The structure of PFDR.

PRDR contains three different faces and each face has an independent concentrator and photodetector. The azimuth angles of the faces are $15°, 135°\ and\ 255°$, while the

elevation of all faces is 30°. The best performance in terms of SNR and time spread is acquired for a FOV of 120° for each face in [14], [15] for the system configurations and system parameters considered. The signal detected by each face go through a combiner before demodulation. Three different combining algorithms are used which are Select Best Combining (SBC), Maximum Ratio Combining (MRC) and Equal Gain Combining (EGC) [[16], [17]]. EGC which directly combines the signals detected by each face is the simplest combining algorithm. However, the signal from the face with the lowest SNR and highest time spread may degrade the SNR of the combined signal. SBC requires an extra circuit to check the SNR of different faces. The signal of the face with best SNR is selected for the demodulator. Conversely, for MRC, the output signals are combined through an adder circuit, in which each input multiplied by weight that is proportional to its SNR. The weight ω_k is defined as [59]:

$$\omega_k = \frac{I_{rk}}{\sigma_k^2}\,, \tag{2-3}$$

where I_{rk} is the electrical current of the detected signal at face k and σ_k^2 is the total noise power at face k. The SNR is defined as [59], [60]:

$$SNR_{MRC} = \frac{\left(\sum_{k=1}^{K} \omega_k I_{rk}\right)^2}{\sum_{k=1}^{K} \omega_k \sigma_k^2} = \sum_{k=1}^{K} SNR_k \tag{2-4}$$

where K is the total number of faces and SNR_k is the SNR of face k. Comparing the three combining algorithms, the performance of SBC is slightly worse than MRC and is much better than EGC [61]. As SBC is simpler than MRC, SBC is preferred in practical systems [61].

To adopt to the features of the LSMS, an improved angle diversity receiver is proposed in [20]-[26]. The structure of this angle diversity receiver is shown in Fig. 2-6. This angle diversity receiver contains three square pyramid faces. Each face has independent concentrator and photodetector while the azimuth angles of the photodetector are $0°, 180° \; and \; 0°$. The elevation angles of two of the photodetectors are $35°$, while the elevation of third photodetector is $90°$ facing up. The FOV of the three photodetectors

is $70°, 70°\ and\ 40°$. This structure guarantees that one photodetector can view at least five spots on the walls or ceiling in the CDC. In [27], a six-face angle diversity was proposed to further enhance the ability to mitigate ambient noise and time spread using more lenses and photodetectors. The advantages of the narrow FOV and combining algorithm of the angle diversity receiver include mitigating the influence of ambient light, improving the SNR, and reducing ISI. However, each photodetector of angle diversity requires an independent concentrator which increases the complexity of the receiver. The bulk size of the angle diversity receiver cannot adapt to mobile users.

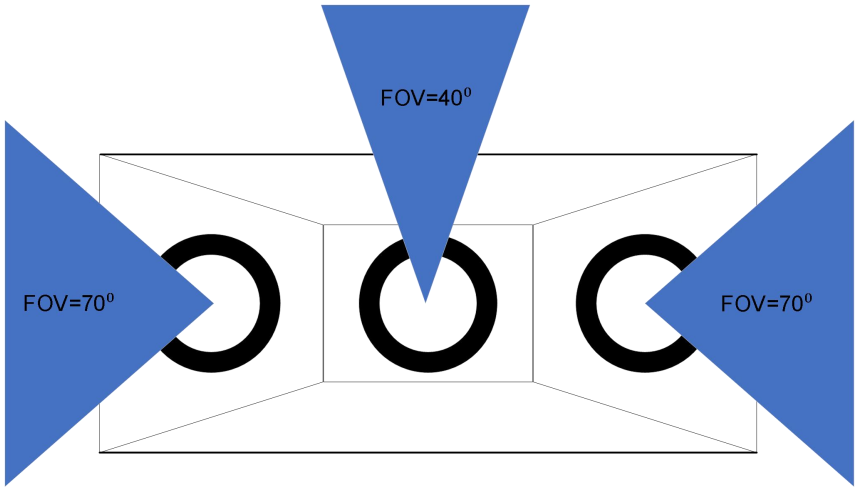

Figure 2- 6 The structure of improved angle diversity receiver.

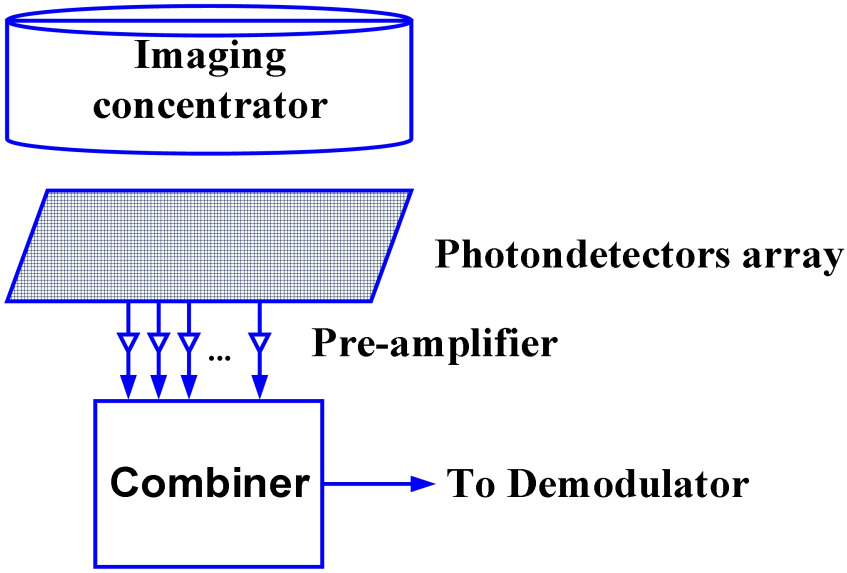

Figure 2- 7 The structure of the imaging receiver [20].

Imaging receiver is a special case of angle diversity receivers. The structure of the imaging receiver is shown in Fig. 2-7 [20]. A common imaging receiver is integrated with an imaging concentrator, a planar array of photodetectors, and a combiner. The planar array is divided into multiple hexagonal or square pixels. Each pixel has an independent photodetector and a preamplifier. Thereby, signals from different directions are collected by different pixels. The detected signals of each pixel are combined at the combiner based on the SBC or MRC algorithm. Compared with the conventional angle diversity receiver, the imaging receiver has two merits. The Imaging receiver adopts only a single imaging concentrator reducing the size and complexity of the receiver. Also, the photodetectors of the imaging receiver are laid on a single plane, which is easier to manufacture with smaller size [62].

If the imaging receiver includes 200 pixels, the detecting area of each photodetector is only $\frac{1}{200}$ of the area of the imaging receiver. The equivalent FOV of each pixel is only 11.3º [20]-[29]. Therefore, the received power of the imaging receiver is an order of magnitude lower than that of the wide FOV receiver. However, the narrow FOV and limited detecting area of the imaging receiver also limits the optical power of the ambient light and the signal from the reflections. In [20]-[29], the results show that imaging receivers have better SNR and time spread performance compared to the wide FOV and angle diversity receivers. In [54], WDM was used with an imaging receiver. An aggregate data rate of 10 Gb/s with $BER = 10^{-6}$ was achieved using OOK [54].

2.5 Modulation Formats of OWC systems

In OWCs, intensity, frequency, phase and polarization modulation are currently considered. Among these, intensity modulation is the most common modulation technique for OWC systems due to its simple transceiver structure. The electrical signal to be transmitted is used to modulate the optical signal from a suitable light source. Direct detection is used with intensity modulation. A photodetector produces a current that is proportional to that of the received instantaneous power. Fig.2-1 shows an IM/DD OW system. Considering the short wavelength of IR or VL, the area of the OWC photodetector is typically larger than the wavelengths which leads to the efficient

spatial property that prevents multipath fading. OW channels can still suffer multipath dispersion due to the different propagation channels of transmitted light. Baseband intensity modulation of OWC systems contains five main classes: (1) Pulse Amplitude Modulation (PAM), (2) Pulse Position Modulation (PPM), (3) Pulse Interval Modulation (PIM), (4) Pulse Width Modulation (PWM) and (5) Subcarrier Modulation (SCM) [22].

2.5.1 PAM

PAM is a basic modulation scheme which is achieved via modulating the intensity of the optical signal. On-Off Keying (OOK), which is based on the rapid switching on-off feature of LDs and LEDs, is a common PAM technique with two levels representing logic 0 and logic 1. There are two types of OOK modulation: Non-Return to Zero (NRZ-OOK) and Return to Zero (RZ-OOK). The waveforms of basic NRZ-OOK and RZ-OOK with a 50% duty cycle are shown in Fig. 2-8. OOK is adopted as a standard in the IEEE 802.15.7 [63]. OOK suffers serious ISI and is subject to multipath dispersion in channels with low bandwidth [44]. The power efficiency and the achieved data rates are relatively lower than other modulation schemes.

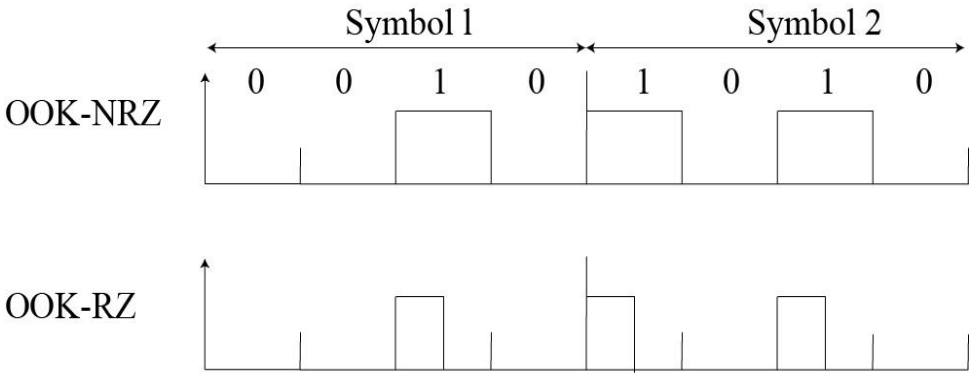

Figure 2- 8 Time waveforms of NRZ-OOK and RZ-OOK.

2.5.2 PPM

PPM is another widely applied modulation scheme that varies the pulse location in the time domain. PPM is an orthogonal modulation technique. PPM can achieve improved average power efficiency at the cost of an increased bandwidth requirement

and greater complexity. PPM is even more sensitive to multipath dispersion compared to OOK. L-level PPM (L-PPM) is a typical PPM technique which can increase the average power efficiency and bandwidth efficiency by increasing the order of L [64], [65]. Instead of 1 bit in a frame, M bits represent the location of the impulse in a frame via L-PPM modulation scheme ($L=2^M$). Information is encoded within the position of the pulse and the position of the pulse corresponds to the decimal value of the M-bit input data. Differential PPM (DPPM) is a major variant of PPM. DPPM varies the duration and sample boundaries to achieve higher bandwidth efficiency with lower average power requirement. DPPM Improves the power efficiency as well as the bandwidth efficiency or the throughput by removing all the empty slots that follow a pulse in a PPM symbol. Fig. 2-9 shows the time domain waveforms of 8-PPM and DPPM. Compared with L-PPM, time synchronisation is not as strict with DPPM decoding which reduces the complexity of the system [24].

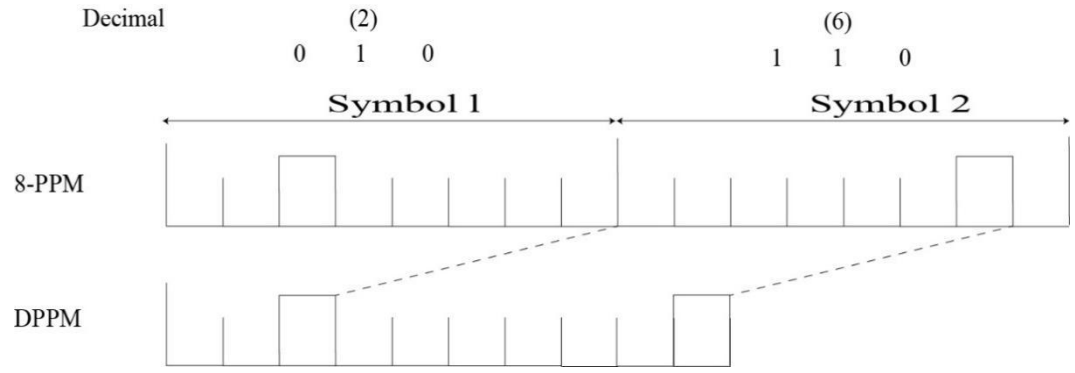

Figure 2- 9 Time waveforms of 8-PPM and DPPM.

2.5.3 PIM, PWM and SCM

In PIM, information is encoded by embedding various vacant time slots between two impulses. PIM is the simplest PPM scheme which deletes the redundant space in PPM, thus improving its bandwidth efficiency. Compared to PPM, PIM has reduced system complexity as a result of reduced symbol synchronisation requirements [42]. In PWM, information is encoded via varying the width of the pulse [25].

In OWC SCM systems, a number of user baseband signals are frequency up- converted prior to intensity modulating the optical carrier as shown in Fig. 2-10. Compared with

single carrier modulation, the main advantages of SCM are the better power efficiency and the multipath dispersion immunity. Conversely, the main drawback of SCM with IM/DD is the poor average optical power efficiency [65]. This is because the SCM electrical signal has both positive and negative values. Therefore, a DC offset must be added to ensure that transmitter (LED or LD) is working in the positive area [66]. Considering that the average optical power of an OWC system is extremely restricted for the skin and eye safety, the balance of the number of subcarriers and the power allocated to each subcarrier is a major challenge of current OWC SCM systems. Orthogonal frequency division multiplexing (OFDM) is applied for SCM modulation to improve the spectrum efficiency [67].

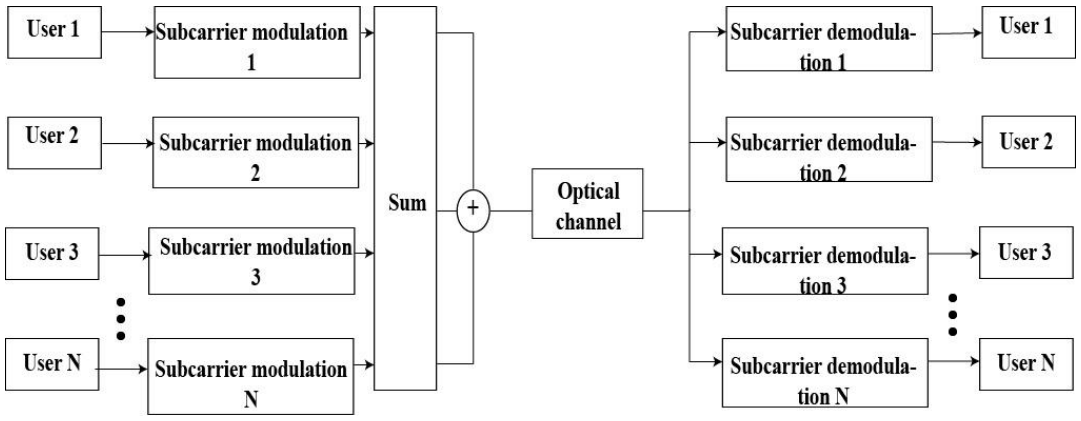

Figure 2- 10 Basic implementation of OWC SCM [63].

2.6 Challenges of OWC systems

OWC systems as a candidate of the next generation wireless communication still face some challenges to be addressed before practically using the systems. In the following we will discuss four challenges. In an indoor environment, the illumination including natural and artificial source introduces white cyclostationary noise in the receiver, which can also degrade the SNR [44]. The multipath dispersion due to the reflections and multiple signal sources results in ISI which limits the achieved data rate. Blockage and shadowing are considered as additional interference sources. In indoor environment, the shadowing and blockage due to the furniture and humans can result in signal outages. Humans impact is more serious as the movements are random and unpredictable. In the following, we further discuss these challenges.

2.6.1 Ambient light

In optical fibre systems, the optical signal is protected from ambient light noise sources. This is not the case with OWC systems where the optical signal is transmitted via free space channel and is exposed to interference from other light sources. OWC receivers collect both the desired optical signal and ambient light (natural and artificial) noise sources [68]. As shown in Fig. 2-1, a photodetector captures some ambient light even with the use of a bandpass filter in front of its active area, where the optical signal will be converted to an electrical signal. The ambient light will generate substantial shot noise and results in the degradation of SNR. Recently, white LEDs and LDs are being adopted as the major illumination sources for indoor environments. Compared with other artificial light source, LEDs and LDs have a narrower spectral power distribution, especially LDs. When LEDs or LDs are used as the illumination system, a bandpass filter can efficiently reduce the influence of ambient light. Considering different material and structures of LED and LD results in different spectral power distribution. Fig. 2-4 shows the power spectral distribution of the sun, fluorescent and incandescent light sources which act as noise sources [17]. Fig. 2-11 shows the spectral sensitivity of a PIN diode [69] and the spectral power distribution of different white LED [70].

With the use of white LED as the main light source of current indoor environments, the power of LED is mainly in the visible spectrum as shown in Fig. 2-11 (b). The light from the sun is a low-risk factor as it can nonetheless lead to a noticeably high shot noise at the receiver's end when the receiver operates close to a window. Sunlight is not subject to quick and random changes, which means that the irradiance it emits can be treated as a steady flow of photons with very slow variations in intensity. In IR systems, a commercial bandpass filter can efficiently reduce the shot noise due to white LEDs. For the sunlight, an IR bandpass film can be used in the receiver to reduce the ambient light noise.

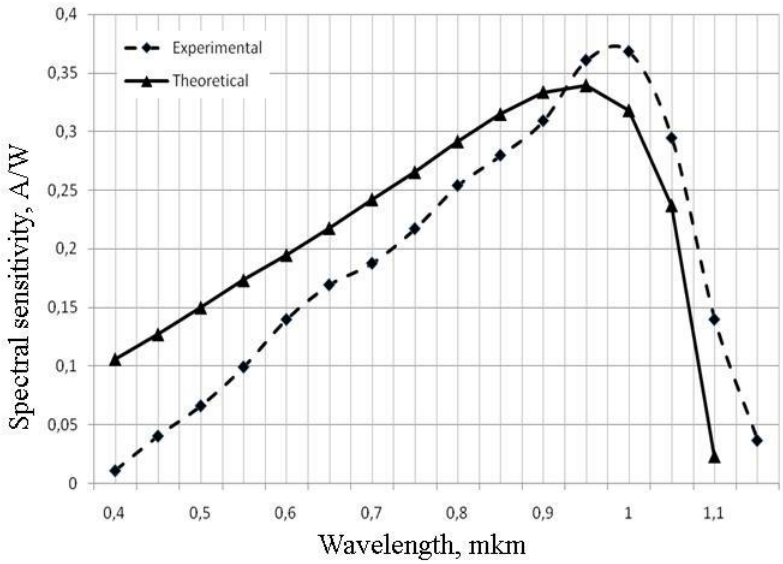

(a) The spectral sensitivity of PIN [69].

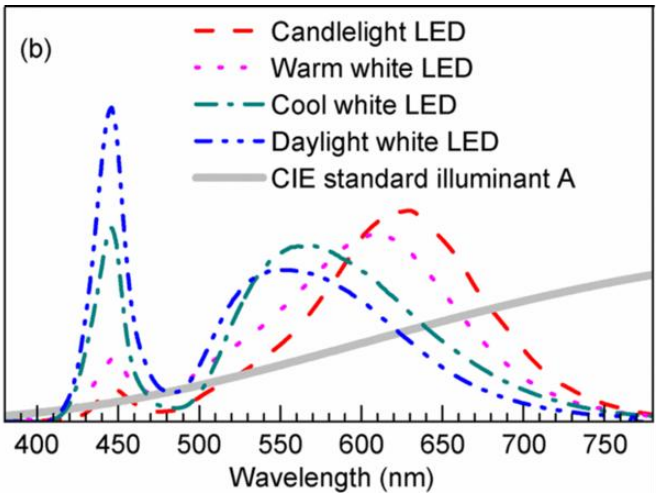

(b) The spectral power distribution of different white LED [70].

Figure 2- 11 The spectral sensitivity and power distribution of PIN and different white LED.

Many studies concentrated on different methods of reducing the effects of background noise [12]-[17], [71]-[75]. Some of these focus on designing a new receiver structure. The core idea of most new receiver structures is to integrating multiple detectors facing different directions. Each detectors possesses a narrow FOV to reduce the received ambient light. Via MRC or SB method, the received signals of different detectors are combined before decoding. The results in [18] show that the new receiver structures can improve the SNR as well as reduce ISI. The angle diversity receiver and the imaging

receiver introduced in Section 2-4 are examples of these receiver structures. However, a main drawback of these structures is the bulk size of the receiver which reduces mobility.

Another way to solve the problem of ambient light is to adopt a narrow light beam transmitter instead of a diffusing transmitter. The higher the optical power detected, the better the SNR at the receiver. However, there are two main challenges with this method. One is that the narrow light beam LOS link can be blocked by furniture and humans. The second challenge is that users randomly move in the room. To overcome this, the transmitter requires real-time positioning information to adjust the beam steering angle to follow the location of the user. Computer Generated Hologram (CGH) and Fresnel phase plated based on SLM were introduced as dynamic beam steering technique in [76], [77]. Both methods control the light beam via changing the phase. In [33], the authors introduced a user location algorithm-based on divide and conquer method. Chapter 6 discusses the use of user locating algorithm and beam steering technique to reducing blockage probability.

2.6.2 ISI

ISI is a big concern when designing an indoor OWC system as it limits the achieved data rate. Two major factors result in ISI. The first one is the multipath dispersion attributed to the reflective properties of the OW channel. In an indoor OW diffuse channel, the transmitted signal travels along multiple paths and can be reflected by walls, ceiling, floor, and furniture in the room. The different arrival times of reflected signals result in time dispersion of the received pulse [78] and cause the ISI. As with the multipath dispersion, when there are multiple signal sources (eg. transmitter and relay nodes) in the room, a user may receive the signals from multiple signal sources. Considering the signal sources are deployed at different locations, the received signals from different signal sources also result in the time dispersion of the received pulse. When more than one signal sources are deployed in the rooms, the ISI attributed to multipath dispersion and multiple transmitters need to be considered. Moreover, the multipath propagation characteristics of the indoor diffuse channels depend on the relative positions of the signal source, the receiver and the reflectors and their optical

properties. These characteristics can be also affected by moving humans and objects. However, the movement changes are slow compared with the transmission rate [44]. Therefore, the channel can be considered stationary for specific transmitter and receiver positions and the received optical power and delay can be considered deterministic. RMS delay spread, and impulse response are the performance indicators to measure the impact of ISI induced by multipath propagation and multiple transmitters [12].

Different techniques have been suggested to reduce ISI. A straightforward idea for addressing ISI is to deploy a single narrow beam transmitter that is directly aimed at the user, where the user is equipped with a narrow FOV receiver. Via the collaboration of a single user coupled with a signal transmitter, the effect of multipath dispersion can be negligible [79]. However, the narrow light beam can be easily blocked and thence, there is a need to calibrate the direction to follow the user. In [76], [77], a phase Fresnel zone plate is mounted on a SLM which is integrated with a LD transmitter. Beam steering angle can be changed via changing the zone centre of the Fresnel zone plate on SLM. In [32], CGH technique was applied on white LDs transmitter, 20% of the average optical power from the transmitter was directed to the location of the user. Considering an OWC system with multiple signal sources, a delay adaptation method is proposed in [80] to balance the signal arrival time from different light sources. For each signal source, a time interval related to the distance between the different signal sources and the receiver is added to the time dispersion of the received signal pulse. Restricting the service area or allocating different spectrum for different light source are also an effective way to reduce the time dispersion [44], [45].

The imaging receiver and angle diversity receiver can also reduce ISI. The narrow FOV of each photodetector restricts the received ambient light power as well as the reflected signal power from walls, ceiling, and floor. The MRC and SB method can also reduce the influence of time dispersion. In [32], CGH and imaging receiver are both used in a VLC system. RMS delay spread of 0.0035 ns and SNR of 22dB were reported when the system operating at 20 Gb/s.

2.6.3 Blockage and shadowing

Reducing the blockage and shadowing influence due to the furniture and moving humans in the room is an important topic for OWC system design. The blockage and shadowing influence due to stationary furniture is predictable and can be reduced by rational transmitter location setup. Conversely, humans are randomly moving in the room with low speed and the real time locations of humans are unpredictable in OWC system. A diffuse transmitter coupled with wide FOV receiver is an effective way to reduce the influence of blockage and reduce the shadowing influence of moving humans. However, this setup faces ambient light due to wide FOV of the receiver and multipath dispersion due to the reflection of walls and ceiling. Multiple signal sources collaboration can be used to solve blockage due to moving humans. The blockage experienced by a rotating user in an environment with fixed obstacles is investigated in [81], [82]. The blockage and shadowing of moving obstacles are simplified and are modelled via a parameter that follows a Bernoulli distribution to investigate the incorporation of multiple Access Points (APs) and its impact on the performance of OWC [83]. In [84], the author introduced a Random Way Point (RWP) model to simulate human movement in the room and modelled the human as a cylinder to evaluate the blockage and shadowing. The results revealed that an OWC system with 8 APs have better performance than the system with 4 APs. RWP models were also used to model humans' motion to study the performance of OWC systems under blockage considering a transmitter with a Lambertian model [85]. Multi APs or transmitters cooperation was considered as the solution of human moving in [81-85]. However, these papers focused on diffuse transmitters. This setup faces large ambient light due to the wide FOV of the receiver and multipath dispersion due to the reflection of optical beams at walls and ceiling. In [86], beam steering is considered and the obstacle is defined as a plane (convex hull). In Chapter 6, with outage probability of a relay assisted OWC system is evaluated to study the influence of blockage and shadowing by humans.

2.7 Summary

In this chapter, we reviewed the characteristics of OWC systems and presented the components and modulation techniques as well as the challenges of OWC systems. We discussed the merits and limitations of different types of OWC transmitters and the structure and materials of different types of OWC receivers. We also reviewed the modulation techniques and challenges including ambient light noise, ISI and human blockage.

Chapter 3: Channel Modelling of Indoor OWC System

3.1 Introduction

To investigate OWC systems in an indoor setting, firstly, the optical wireless link must be modelled considering the channel connecting the transmitter and the receiver. Secondly, interfering factors that impair the performance of the OWC system including background noise sources, receiver noise, multipath propagation, mobility and human blockage must be modelled in an indoor setting to study their effect on the received signal. Finally, a simulation tool based on these two steps is built in MATLAB. In this chapter, the simulation package we developed to simulate the OW channel in an indoor environment is presented. To evaluate the simulation package, we verified simulation results of the literature works on OWC systems including CDS, LSMS with wide FOV receivers and angle diversity receivers [10]-[12]. As a result of multipath propagation, a mathematical formulation and ray tracing algorithm are employed to compute the received optical power from a number of reflection elements. A good match was observed with the results in literature.

The remainder of this chapter is organised as follows: The indoor OWC ray tracing-based channel model is discussed in Section 3.2. The performance indicators including SNR, RMS and outage probability are presented in Section 3.3. The simulation results of previous work in OWC systems are presented in Section 3.4. Finally, a summary is given in Section 3.5.

3.2 Indoor OWC ray tracing-based channel model

With IM/DD and, as shown in Fig. 2-1, the instant received optical signal is converted into electrical current. This process can be described by the following equation [25]:

$$I(t) = R\,x(t) \otimes h(t) + n(t)\,, \tag{3-1}$$

where $I(t)$ is the instantaneous photocurrent of the receiver at a certain location in the room, $x(t)$ is instantaneous optical power of the transmitter, R is photodetector responsibility of the receiver, $\otimes$ represents the convolution operation, $h(t)$ is impulse response of the channel from the transmitter to the receiver, and $n(t)$ is the additive Gaussian noise due to different noise sources (etc. ambient light, thermal noise at receiver). The receiver movement speed is slow compared to the transmission rate in indoor environments. Therefore, the channel can be considered stationary for specific transmitter and receiver positions. The impulse response, $h(t)$, reflects the propagation characteristics of an indoor optical wireless channel depending on the relative positions and radiation pattern of the transmitter, receiver, and reflectors including walls, ceiling, and floor. Due to the reflecting property of optical signals, they travel different propagation distances before reaching the receiver which results in the multipath dispersion. To evaluate the influence of multipath dispersion, the optical property of the reflectors is required. Measurements to study the reflection coefficients for a number of materials normally used in indoor settings were taken by Gfeller and Bapst [87]. They have shown that the reflection coefficients (ratio of reflected power to incident power) ranged from 0.4 to 0.9 and with white plaster walls the reflection coefficients vary between 0.7 and 0.85 based on the surface consistency and angle of incidence. They also observed that the power reflected by either the walls or the ceiling takes a form similar to a Lambertian radiation pattern. The phenomenon in which incident energy, centered at the point of incidence, is uniformly reflected in all directions within the hemisphere is called diffuse reflection, also known as isotropic reflection. A perfect diffusing surface is referred to as a Lambertian surface [25]. The walls, floor and ceiling are divided into many reflecting elements in the literature and in this thesis. These reflecting elements can be seen as small secondary emitters that diffuse the received signal from the transmitter or other reflecting element in multiple paths. The power radiated from a general Lambertian radiation pattern into a solid angle $d\omega$ can be represented as the following [25]:

$$dP = \frac{n+1}{2\pi} P_s \cos^n \theta \, d\omega, \tag{3-2}$$

where P_s is the optical power of the light source, $\frac{n+1}{2\pi}$ ensures that integrating dP occurs over a hemisphere surface, θ is the angle of incidence related to the normal angle of the light source, and n represents the mode number that determines the shape of the radiated beam. The mode number n of a radiated beam is defined as:

$$n = \frac{-\ln(2)}{\ln(\cos(\text{hps}))}, \tag{3-3}$$

where hps is half-power semi-angle of the light source. As n increases, the beam shape of the light source becomes narrower. For $n = 1$, the radiation pattern of the light source is an ideal Lambertian radiation. In this work, the walls, ceiling and floor are considered to be a plaster surface which is modelled as an ideal Lambertian radiation pattern based on the results in [22].

To investigate the influence of reflectors on the channel from transmitter to receiver and based on the simulation model proposed by Barry in [45], a ray tracing model for indoor OWC is developed. The transmitted signals are reflected from all possible room reflecting surfaces, which were divided into a number of equal-sized, square shaped reflection elements. The reflection elements have been treated as small transmitters that diffuse the received signals from their centres in a Lambertian radiation pattern [11]. The third-order reflections and higher order reflections do not produce significant change in the received optical power, and therefore reflections up to the second order only are considered [12]-[14]. The surface element sizes used in this thesis were set to 5cm by 5 cm for the first-order reflections and 20 cm by 20 cm for the second-order reflections, considering the balance between the computation complexity and the simulation accuracy. The optical power at the receiver can be defined as the linear summation of the LOS component, first order reflection components and second order reflection components and can be expressed as [25]:

$$P_r = P_{LOS} + \sum_{i=1}^{N} dP_i^{(1)} + \sum_{i=1}^{M} dP_i^{(2)}, \tag{3-4}$$

where N is the total number of reflection elements in the room for the first order reflection elements, and M is the total number of reflection elements in the room for

second order reflection. As shown in Fig. 3-1, we assume that a Lambertian radiation transmitter is deployed at the centre of the ceiling, while the receiver is located in the communication plane which is 1m above the floor. The LOS (the orange dashed line in Fig. 3-1) can be defined as:

$$P_{LOS} = \frac{n+1}{2\pi R^2} P_s \cos^n \theta \cos \delta dA \, rect(\delta/FOV), \tag{3-5}$$

where n is the radiation mode of transmitter, R is the Euclidian distance between transmitter and receiver, P_s is the average optical power of the transmitter, θ is the angle of incidence relating to the normal angle of the transmitter, δ is the difference between the normal angle of the photodetector and the incident signal, dA is the integration of the photodetector area of the receiver, and $rect(\delta/FOV)$ is a rectangle function which is defined as:

$$rect\left(\frac{\delta}{FOV}\right) = \begin{cases} 1 & \frac{\delta}{FOV} \leq 1 \\ 0 & \frac{\delta}{FOV} > 1 \end{cases}, \tag{3-6}$$

where FOV is the field of view of the receiver. Based on equation (3-6), we can find that a greater FOV receiver can collect more optical power. However, a greater FOV also result in receiving more ambient power and leads to ISI.

The received optical power for a first order reflection, represented by a pink dashed line in Fig. 3-1, can be given as:

$$dP_i^{(1)} = \frac{(n_1+1)(n+1)}{4\pi^2 R_1^2 R^2} \rho_1 P_s \cos^{n_1} \theta \cos \alpha \cos^{n_2} \beta \cos \delta dA \, dA_1 rect(\delta /FOV), \tag{3-7}$$

where n_1 is the radiation mode of a reflection element for the first order, R is Euclidian distance between the reflection element and the transmitter, R_1 is the Euclidian distance between the reflection element and receiver, ρ_1 is the reflection efficiency of the reflecting element for the first order, α is the difference between the normal angle of the reflecting element and the incident signal, β is the difference between the normal angle

of the reflecting element and the emitting direction, and dA_1 is the integration of the photodetector area of the reflection element for the first order.

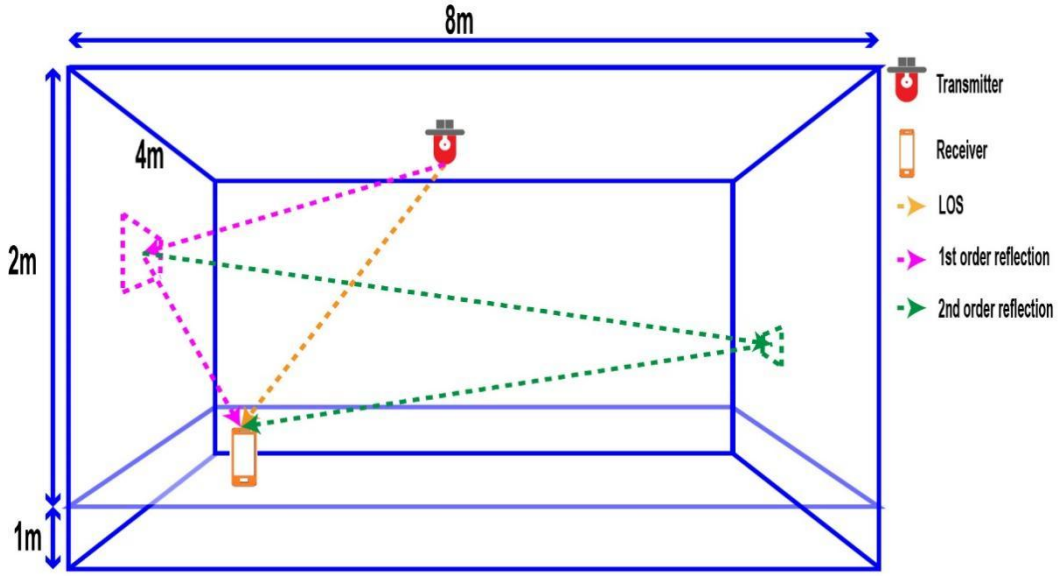

Figure 3- 1 The ray tracing model for indoor environment.

The second order reflection, represented by green dashed line in Fig. 3-1, can be represented as follows:

$$dP_i^{(2)} = \frac{(n+1)(n_1+1)(n_2+1)}{4\pi^2 R_1^2 R_2^2 R^2}\rho_1\rho_2 P_s H$$
$$H = \cos^n\theta \cos\alpha \cos^{n_1}\beta \cos\gamma \cos^{n_2}\varepsilon \cos\delta dA\, dA_1 dA_2 rect\left(\frac{\delta}{FOV}\right), \quad (3\text{-}8)$$

where n_2 is the mode number of the radiation pattern of the reflecting element for the second order, R is Euclidian distance between the reflection element for first order and the transmitter, R_1 is the Euclidian distance between the reflection element for the first order and the reflection element for second order, ρ_2 is reflection efficiency of the reflecting element for second order, γ is the angle between the normal of reflecting element for second order and incident signal, ε is the angle between the normal of reflecting element for second order and emitting direction, and dA_2 is the integration of the photodetector area of the reflection element in second order.

In this thesis, the Gaussian radiation transmitter is considered in Chapter 6. Gaussian wave is a signal waveform described by a Gaussian function. This waveform has Gaussian distribution characteristics with its main features being centered symmetry, maximum amplitude at the center, and gradually decreasing amplitude [41]. The waveform emitted by a laser emitter is approximately Gaussian in shape [40]. When a Gaussian beam is reflected by Lambertian radiation material, it gets transformed into a Lambertian radiation pattern [88]. Therefore, the only difference between Gaussian radiation transmitter and Lambertian radiation transmitter is the LOS component. The LOS component of a Gaussian radiation transmitter is given as [88]:

$$P_{LOS} = \int_{\Delta S} \frac{2P_s}{\pi\omega^2} e^{\frac{-2R^2}{\omega^2}} cos\,\delta\, dR, \tag{3-9}$$

where ω is the distance out from the centre axis of the beam, e is the natural number, R is the transverse distance from the axis and ΔS is the area of receiver.

3.3 The performance indicators of OWC systems

The impulse response, SNR, the RMS delay spread, and the outage probability are commonly used to evaluate the performance of OWC systems. In this section, these performance indicators are defined. In Chapter 6, SINR and achievable rate are investigated to study the multiuser environment.

3.3.1 The impulse response

Practically, the impulse response of an OWC wireless system is continuous. However, in the ray tracing model, walls, floor, and ceiling reflecting surfaces are divided into numerous discrete elements. Therefore, the impulse response gives the received optical power at the receiver within time intervals. A suitable suggestion for the time interval width is the time taken by light to travel between neighbouring elements which is given as [89], [90]:

$$time\ inteval = \frac{\sqrt{dA}}{\mathrm{c}}, \tag{3-10}$$

where dA is the reflection element area and c is the speed of light. With the time interval as a dimensional factor of the impulse response, the rays received within similar time interval are assembled and stored for a particular transmitter-receiver position. In the simulation, the impulse response result displays a histogram of the total optical power of the received rays within each time interval [24]. It should be observed that the reduction of dA results in improved resolution in the impulse response together with an increase in the computation time. Thus, choosing the time interval width is a trade-off between the computation time and the resolution. Meanwhile, according to the adaptation theory, $time\ interval \leq \frac{c}{2\times bandwidth}$.

3.3.2 The RMS delay spread

In indoor environments, the OWC system is affected by multipath dispersion and multiple signal sources. They both cause the received signal to spread in time resulting in ISI. The channel spread can be quantified using the RMS delay spread [91], [92]. RMS delay spread is defined as [11]-[13]:

$$D = \sqrt{\frac{\sum_{i=1}^{\infty} \sum (t_i - \mu)^2 Pr_i^2}{\sum_{i=1}^{\infty} Pr_i^2}} \tag{3-11}$$

where t_i is the delay time (time interval) associated with the received optical power, Pr_i, and μ is the mean delay given by:

$$\mu = \frac{\sum_{i=1}^{\infty} t_i Pr_i^2}{\sum_{i=1}^{\infty} Pr_i^2} \tag{3-12}$$

RMS delay spread represents the degree of power dispersion in the time domain. In this chapter, RMS delay spread is used to quantify the performance of typical CDS and LSMS systems [12-14].

3.3.3 SNR

The OWC system's performance is best evaluated using the SNR, which also provides a measure of the noise and signal spread (eye opening). The probability of error for OOK is expressed as:

$$P_e = \mathrm{Q}(\mathrm{SNR}), \tag{3-13}$$

where the Q function can be approximately defined as：

$$Q(x) = \frac{1}{2} erfc\left(\frac{x}{\sqrt{2}}\right) \approx \frac{1}{\sqrt{2\pi}} \frac{e^{-\left(\frac{x^2}{\sqrt{2}}\right)}}{x}. \tag{3-14}$$

When $SNR = 15.6dB$, x in equation (3-14) approximate to 6. Based on Equation (3-13) and (3-14), $P_e \approx 10^{-9}$ can be achieved. Therefor $SNR \geq 15.6dB$ is required for guaranteeing $P_e \leq 10^{-9}$ for OWC communication. SNR for OOK-based OWC system is defined as:

$$SNR = \left(\frac{R(P_{s1} - P_{s0})}{\sigma_0 + \sigma_1}\right)^2 \tag{3-15}$$

where R is the responsivity of the receiver, P_{s1} and P_{s0} are the power levels associated with logic 1 and logic 0, respectively, σ_0 and σ_1 are the noises associated with the received signal at logic 1 and logic 0, respectively and can be computed as follows [34], and [93]:

$$\sigma_0 = \sqrt{\sigma_{s0}^2 + \sigma_{bn}^2 + \sigma_{pr}^2} \;\; and \; \sigma_1 = \sqrt{\sigma_{s1}^2 + \sigma_{bn}^2 + \sigma_{pr}^2} \tag{3-16}$$

where σ_{s0}^2 and σ_{s1}^2 are the shot noises associated with the received signal at logic 1 and logic 0, respectively and are computed as follows:

$$\sigma_{s1} = \sqrt{2RqP_{s1}BW} \; and \; \sigma_{s0} = \sqrt{2RqP_{s1}BW} \tag{3-17}$$

where BW is the receiver bandwidth and q is the electron charge. According to the experimental results reported in [94], this signal-dependent noise is very small and is often neglected. σ_{pr}^2 represents the user preamplifier noise component related to the bandwidth of the receiver and the noise spectral density of the preamplifier.

σ_{bn}^2 represents the background shot noise at the user's receiver and is given as:

$$\sigma_{bn} = \sqrt{2RqP_bBW} \tag{3-18}$$

where P_b is the receiving ambient light power computed as follows:

$$P_b = \sum_{i=1}^{L}\left(P_i^{LOS} + \sum_{n=1}^{N} dP_{i,n}^{(1)} + \sum_{m=1}^{M} dP_{i,m}^{(2)}\right) \tag{3-19}$$

where L is total number of illumination light sources in the room. The received ambient light power is calculated considering a Lambertian transmitter.

3.3.4 The outage probability

In indoor OWC system, the speed of a moving user is slower than the communication rate. Therefore, the channel between the receiver and transmitter is relatively stationary. However, there are still some interfering factors (e.g., the blockage and shadowing due to humans moving, the air turbulence due to air conditioner and fans), fan blades motion, which can all cause sharp fading of the channel between transmitter and receiver. The outage probability is used to qualify the stabilisation of the channel. Outage probability is defined as the possibility of the communication rate being lower than a threshold which results in service interruption. The outage probability P_{out} is given as:

$$P_{out}(\mathrm{SNR} < \mathrm{SNR}_{th}) = \int_{-\infty}^{\mathrm{SNR}_{th}} f(x) \tag{3-20}$$

where SNR_{th} is the baseline of guaranteeing the normal OWC communication, and $f(x)$ is the probability density function of the SNR.

3.4 The simulation results of typical CDS and LSMS OWC systems

To evaluate the OWC system performance under the impact of multipath propagation, user mobility, human blockage and background noise, the channel impulse response of the OWC system must be evaluated and the background noise has to be determined. In this chapter, the impulse response and background noise evaluations are based on the mathematical formulation presented in Section 3.2 and Section 3.3 and a ray tracing algorithm built in MATLAB.

The room setup of CDS is shown in Fig. 3.2(a), where a transmitter and a user are located on the same plane. The radiation pattern of a CDS transmitter is a typical

Lambertian pattern, and the user can receive the signal from the reflections from the walls and ceiling. Fig. 3.2(b) shows the room setup of LSMS system. The Tran-

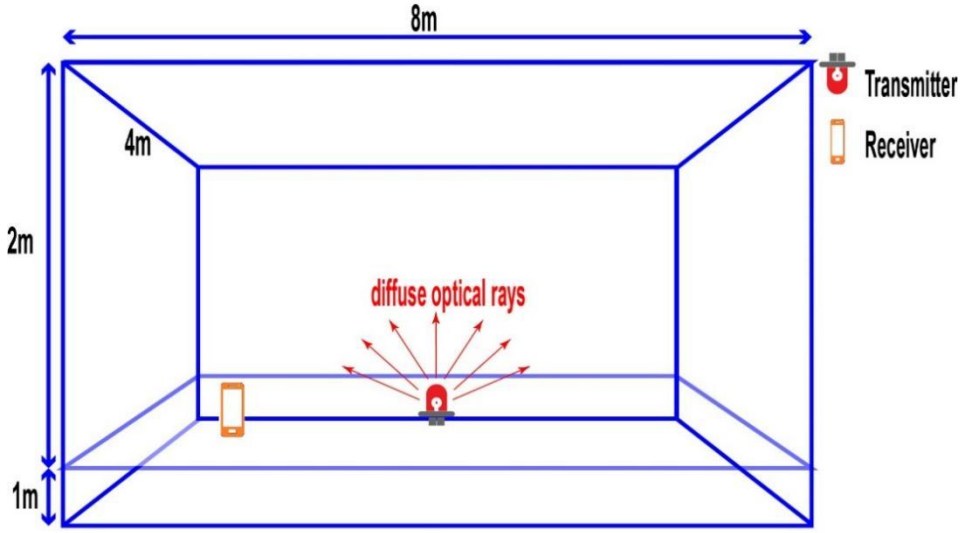

(a)

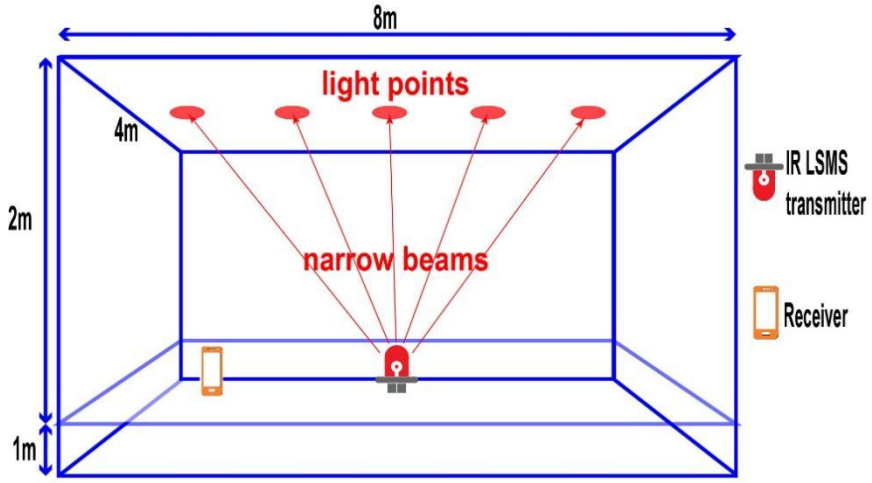

(b)

Figure 3- 2 The room setup of CDS and LSMS system.

-mitter of LSMS produces multiple light spots on the ceiling. These light spots act as secondary transmitters sending signal to the user.

The impulse response results of previous work considering CDS and LSMS verified using our simulator are considered as a baseline to evaluate the performance of our proposed systems. The IR transmitter of CDS and LSMS is deployed on the communication plane facing up. The transmitter of CDS is a diffusing transmitter modelled as an ideal Lambertian transmitter ($n = 1$), while the transmitter of LSMS produces a line of light points which act as a secondary transmitter on the ceiling with holographic optical element or multiple emitters. Two different receivers are considered including wide ($FOV = 180^{\circ}$) receiver and ADR receiver which were discussed in Section 2.4. The ray tracing algorithm mentioned in Section 3.2 is developed in [14]-[19] using the room configuration and parameters given in Table 3-1. The length, width and height of room were set as 8m, 4m, and 3m, respectively. The devices of OWC system are deployed on or above the communication plane which is one meter above the floor as the general height of desk. The OWC signal is blocked below communication plane in this configuration [14]-[16]. In IRC systems (CDS and LSMS), the transmitter and receiver can be situated at the corner of the room (1m,1m,1m) on the communication plane to measure the worst channel condition of IRC system. The transceiver specifications and other parameter of IRC examples are based on [34], [35].

Table 3- 1 The parameters of CDS and LSMS

Transmitter type	IRC (CDS LSMS)
Room setup	
Length, width, height	8m, 4m, 3m
Reflectivity of the walls	0.8
Reflectivity of the ceiling	0.8
Reflectivity of the floor	0.3
AP	
Quantity	1
Location	(2, 4, 1)
Power	1W
Illumination	

Quantity	8		
Location	(1, 1, 3), (1, 3, 3), (1, 5, 3), (1, 7, 3), (3, 1, 3), (3, 3, 3), (3, 5, 3), (3, 7, 3)		
Power	18w		
Radiation mode n	33.1		
Wide FOV Receiver			
Quantity of detector	1		
Elevation	90º		
Azimuth	0º		
FOV	180º		
Area of detector	1 cm^2		
The responsivity	0.5 A/W		
ADR Receiver			
Quantity of detector	3		
FOV	70°	70°	40°
Elevation	35°	90°	180°
Azimuth	35°	0°	0°
Area of detector	1 cm^2		

Fig. 3-3 illustrates the impulse response of CDS, LSMS and LSMS with ADR. The ADR suppressed ISI by reducing the reflection components of the impulse response. The deviations of the simulation impulse response results in Fig. 3-3 and the impulse response in [14] are less than 2 percent.

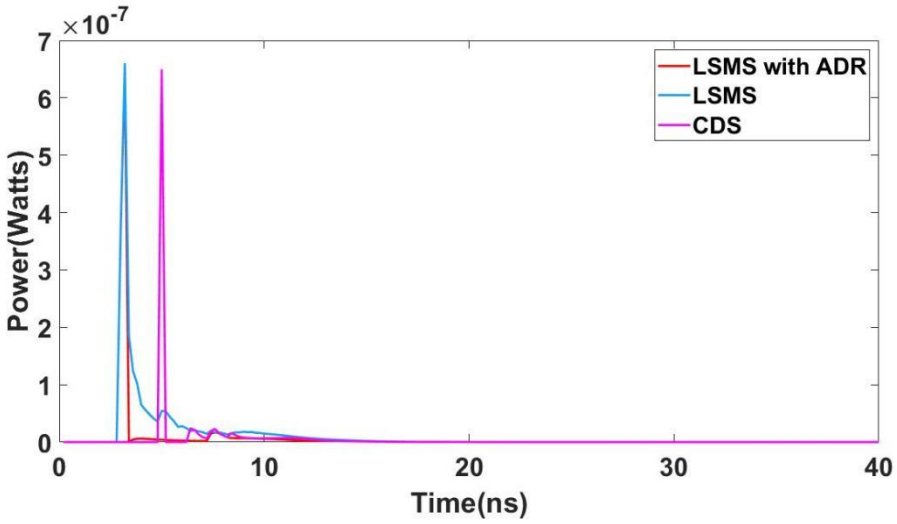

Figure 3-3 Impulse responses of CDS and LSMS systems with wide FOV receiver (FOV=90°) and LSMS systems with ADR (select best algorithm); transmitter is located at room centre, while receiver is located at the room corner(1m,1m,1m)

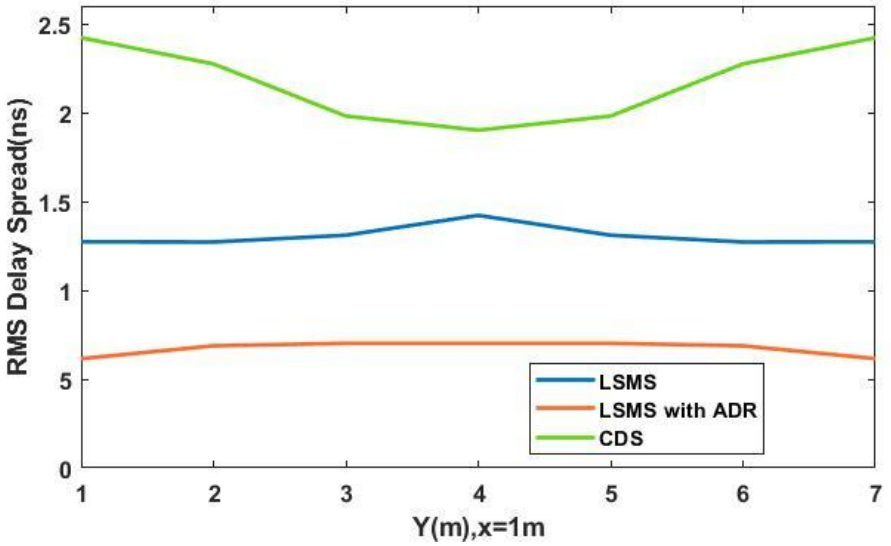

Figure 3-4 Delay spread of CDS, LSMS (wide FOV) and LSMS with ADR; transmitter is located at room centre, while receiver moved along Y axis with X=1M.

Fig. 3-4 illustrates the RMS delay spread performances of the CDS, LSMS and LSMS with ADR. Compared to CDS, LSMS receiver can receive LOS components from the spotlights on the ceiling which reduces the optical power distribution degree in the time

domain. The time spread was decreased from around 2.4 ns to around 1.3 ns. Deploying the ADR in the LSMS system, suppresses the influence of reflection components as a result of the narrow FOV of ADR. Better time performance is obtained when LSMS is coupled with ADR. Compared with the impulse response in [11] and [14], the deviations of the simulation results in Fig. 3-3 and are less than 5 percent.

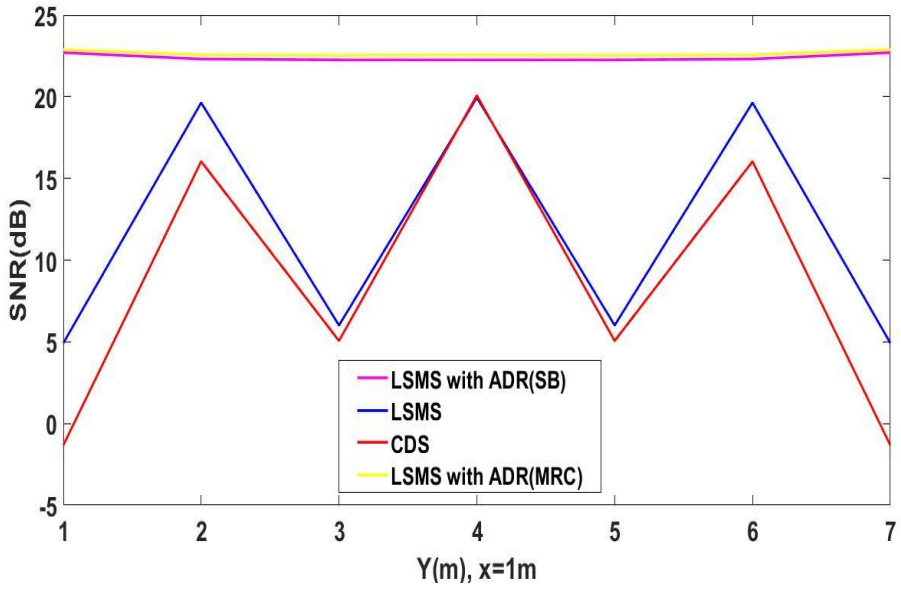

Figure 3-5 SNR of CDS, LSMS (WIDE FOV) and LSMS with ADR (SB and MRC algorithm); transmitter is located at room centre, while receiver moved along Y axis with X=1M

Fig. 3-5 shows the SNR of CDS, LSMS (wide FOV) and LSMS with ADR (SB and MRC algorithm), when the transmitter is located at the room centre, while the receiver is moved along Y axis with x=1m. Two different signals combining method (SB and MRC) for ADR are considered. The simulation SNR results of MRC and SB are similar. The SNR of one face dominates over other faces. Compared to CDS, LSMS receives LOS component from the spotlights on the ceiling which increases the received signal power. The narrow FOV of ADR suppress the influence of background noise causing the increasing of LSMS SNR. Compared with the SNR results in [10], the deviations of the simulation results in Fig. 3-4 are less than 3 percent.

3.5 Summary

In this chapter, we reviewed the channel model of indoor OWC systems and introduced the ray tracing model for simulating the impulse response for OWC channel. A simulator based on ray tracing model is developed in MATLAB. To evaluate the performance of OWC systems, performance indicators including SNR, RMS delay spread, impulse response and outage probability are evaluated using our simulator. A good match was observed, giving confidence in the capability of the author's simulator to evaluate new OWC systems.

Chapter 4: A Delay Adaptation Method for Relay Assisted OWC Systems

4.1 Introduction

Most of the previous work on indoor OWC system has focused mainly on the transceiver design. Improving the channel between the transmitter and the receiver is a challenging task that can enhance the optical power received by users and reduce ISI. Relay-based communication, which are widely used in RFC systems to improve the channel, are also proposed for the use in OWC systems [95]-[99]. The work in [98], addressed the beam blockage by humans sitting or moving in the communication plane between the main light source and the user. The authors suggested the use of an additional desk or floor light to assist communication when the beam from the main light source is blocked. Similarly, the authors in [97] considered nearby mobile phones with two photodetectors and a transmitter LED array as relay nodes to provide relay-assisted service to a user. The above-mentioned work focused on the relay assisted communication in fixed circumstances to overcome blockage and shadowing. The performance of the relay assisted communication with a moving user was not taken into consideration. The relay technique was integrated with OFDM in [98] and [99] to further improve the performance of indoor OWC systems. Both amplify-and-forward and decode-and-forward relaying techniques were investigated in a relay-assisted Direct Current biased Optical (DCO)-OFDM VLC system in [99]. These papers [95]-[98] only considered a relatively stationary situation where only one relay node and one user are located at fixed locations [95]-[98]. The impact of the number, type, and location of the relay node (i.e., terminal) were not adequately investigated. In [95] and [96], the authors introduced a relay-assisted indoor OWC system with multiple relay terminals and assessed the influence of the relay nodes location on a moving user. However, the authors did not optimise the locations of the relay nodes.

Multipath propagation in a relay-assisted OWC system with multiple relay terminals signals, where relayed signals travel different distances and arrive at different times,

results in serious pulse spread and ISI. In this chapter, we propose a delay adaption method to address this problem. The proposed method balances the arrival time of the signals from different relay terminals by adding a pre-calculated delay to different relay terminals. To study the effectiveness of this method, we consider three different relay terminals deployment scenarios.

The relay communication mode and the channel model for three different types of relay terminals are discussed in Section 4.2. The proposed delay adaptation method is introduced in Section 4.3. The simulation results of the proposed delay adaptation method considering three different types of relay terminals are presented in Section 4.4. This chapter is summarised in Section 4.5.

4.2 The Relay Communication Mode and the Channel Modelling for Different types of Relay Terminals

4.2.1 The Relay Communication Mode in CDS Systems

To investigate the performance of a relay assisted IR-based CDS OWC system, we utilise a basic relay communication mode with a simple half duplex time division multiplexing protocol [97], [99]. In this work, the OWC system contains a diffuse AP, typically located on the communication floor and a Wide-Field-of-View (WFOV) receiver for each user. In this relay mode, a time slot is divided into 4 phases. In the first phase, the AP sends a downlink signal to the relay terminals. In the second phase, all relay terminals amplify and send the downlink signal to the user on the communication plane. In the third phase, the user sends the uplink signal to the relay terminals while in the last phase, the relay terminal forwards the amplified uplink signal to the AP. The flow chart of the basic relay communication mode (i.e., relay-assisted downlink and uplink communication in one time slot) is shown in Fig. 4-1.

In the first phase, the photodetection current, $I_r(t)$, at relay terminal r, where $r \in \mathrm{R}$, and R is the set of all relay terminals, is defined as the following:

$$I_r(t) = R_r X(t) \otimes h_{sr}(t) + N_r(t), \tag{4-1}$$

where $X(t)$ is the optical power emitted from the AP in W, R_r is the responsivity of the relay terminal r in A/W, $h_{sr}(t)$ is the impulse response for the channel between the AP and relay terminal r, and $N_r(t)$ is the additive white Gaussian noise at relay terminal r.

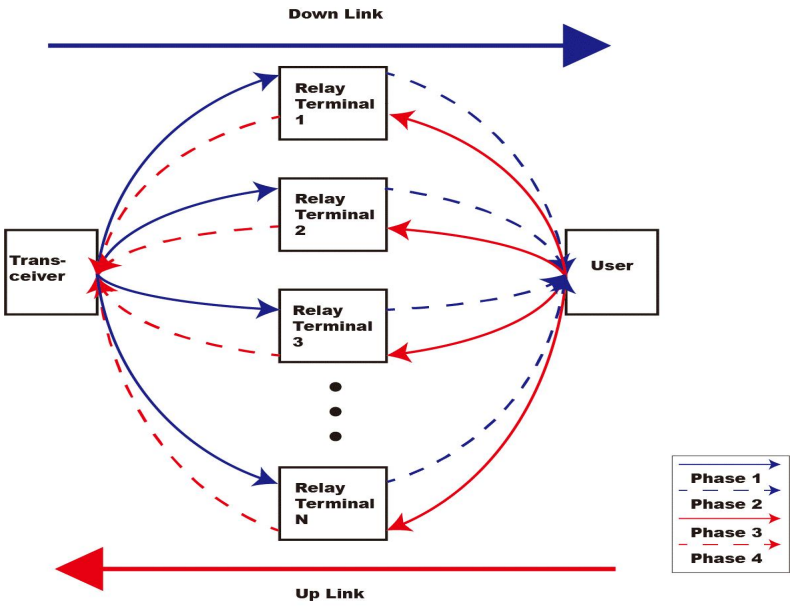

Figure 4- 1 The Flow Chart of Basic Relay Communication in One Time Slot.

In the second phase, the downlink photodetection current $I_u(t)$ at a user is defined as follows:

$$I_u(t) = R_u \sum_{r \in R} (X_r(t) \otimes h_{ru}(t)) + N_u(t) \tag{4-2}$$

where $X_r(t)$ is the instantaneous optical power from relay terminal r in W, R_u is the responsivity of the user in A/W, $h_{ru}(t)$ is the impulse response for the channel between the relay terminal r and the user, and $N_u(t)$ is the additive white Gaussian noise at the user's transceiver. In this work, we adopt IM/DD OOK. In OOK modulation, logic 1 and 0 are sent by switching the light source on or off, respectively during the bit period. In the second phase, the SNR of a user (SNR_u) is given as [12] and [95]:

$$SNR_u = \left(\frac{R_u \sum_{r \in R} (P_{s1,r} - P_{s0,r})}{\sigma_{u0} + \sigma_{u1}} \right)^2, \tag{4-3}$$

where $P_{s1,\mathrm{r}}$ and $P_{s0,\mathrm{r}}$ are the power levels associated with logic 1 and logic 0, respectively, $\sigma_{\mathrm{u}0}$ and $\sigma_{\mathrm{u}1}$ are the noise associated with the received signal at logic 0 and logic 1 respectively, and can be computed as the following [97], and [25]:

$$\sigma_{u0} = \sqrt{\sigma_{s0,u}^2 + \sigma_{bn,u}^2 + \sigma_{pr,u}^2 + \sum_{r\in R} \sigma_{r,u}^2} \tag{4-4}$$

$$\sigma_{u1} = \sqrt{\sigma_{s1,u}^2 + \sigma_{bn,u}^2 + \sigma_{pr,u}^2 + \sum_{r\in R} \sigma_{r,u}^2} \tag{4-5}$$

where $\sigma_{s0,u}^2$ and $\sigma_{s1,u}^2$ are the shot noises associated with logic 0 and logic 1, respectively for user u. According to the experimental results reported in [103], this signal-dependent noise is very small and is often neglected. $\sigma_{bn,u}^2$ represents the background shot noise at the user's receiver, $\sigma_{pr,u}^2$ represents the user preamplifier noise component at user u, and $\sum_{r\in R} \sigma_{r,u}^2$ is the sum of the noise components from all relay terminals at user u. For the uplink (i.e., phase 3 and 4 of the relay communication mode), the functions of AP and user are exchanged and hence, the SNR for uplink is derived in a similar way to the downlink SNR. The SNR of the uplink at the terminal, SNR_t, is given as

$$SNR_t = \left(\frac{R_t \sum_{r\in R} (P_{s1,r} - P_{s0,r})}{\sigma_{t0} + \sigma_{t1}} \right)^2 \tag{4-6}$$

where σ_{t0} and σ_{t1} are equivalent to $\sigma_{\mathrm{u}0}$ and $\sigma_{\mathrm{u}1}$ in Equation (4-4) and (4-5), respectively. In the next section, we will focus on the discussion of the downlink for three different types of relay terminals.

4.2.2 Relay Terminal Types:

Relay terminals can be generally classified into two groups which are amplify-and-forward relay terminals and decode-and-forward relay terminals [97]. For the amplify-and-forward type, the relay terminal only amplifies the received signal with an electrical or optical (e.g., Semiconductor Optical Amplifier (SOA)) amplifier and directly

forwards it to the user. Therefore, amplify-and-forward relay terminals have a relatively simple structure, however, it will amplify the signal and noise simultaneously. On the contrary, a decode-and-forward relay terminal can be seen as a fully functional transceiver. It will decode the received signal and re-encode it before modulating. To investigate the influence of the relay terminals type, we consider optoelectronic (O-E-O) amplify-and-forward, SOA amplify-and-forward, and decode-and-forward relay terminals. The structure of these relay terminals, the impulse response, and the SNR calculations are detailed in the next paragraphs.

4.2.2.1 O-E-O amplify-and-forward relay terminal

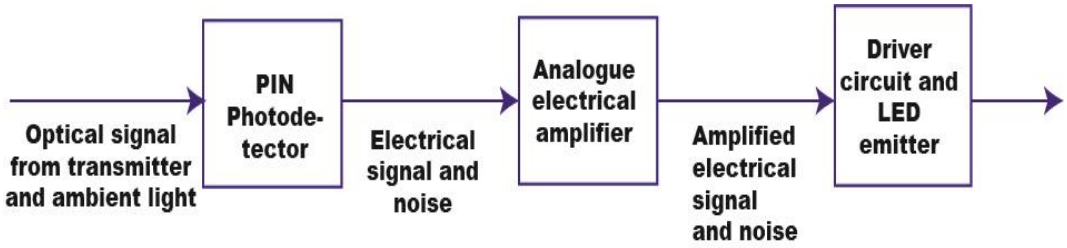

Figure 4- 2 O-E-O Amplify-And-Forward Relay Terminal.

The structure of an O-E-O amplify-and-forward relay terminal is shown in Fig. 4-2. The optical signal from the AP is transformed into an electrical signal via a PIN photodetector. Then, the electrical signal is amplified by an electrical amplifier before using it to modulate an IR Laser or LED [10] and [11]. We assume that the parameters of the O-E-O amplify-and-forward relay terminal are constant within the noise equivalent bandwidth [104]. With O-E-O amplify-and-forward relay terminals, the photodetection current, $I_u(t)$, generated by the received downlink optical signal at the user from the relay terminals in the second phase is defined as follows:

$$I_u(t) = R_u \sum_{r \in R} \left(\frac{hf}{q} \eta_g G_A I_r(t) \otimes h_{ru}(t)\right) + N_u(t), \tag{4-7}$$

Where f is the central frequency, h is Planck's constant, q is the elementary charge, η_g is the external quantum efficiency of the relay terminal, and G_A is the amplifier gain of

the relay terminal. The SNR of the user (SNR_u) is given by Equation (4-3) where the values of σ_{u0} and σ_{u1} are given by Equation (4-4) and (4-5). For an O-E-O amplify-and-forward relay terminal the Gaussian noise, σ_r^2 is given as [104]:

$$\sigma_r^2 = 2qR_u\left(\frac{hf}{q}\sqrt{N_r B_r}H_{ru}(0)\right)B_u, \tag{4-8}$$

where B_u and B_r are the bandwidth of the user and the relay terminal, respectively, N_r is the noise spectral density at the output of relay terminal r, and $H_{ru}(0)$ is the channel gain from relay terminal r to the user. $H_{ru}(0)$ can be given as:

$$H_{ru}(0) = \int_{-\infty}^{\infty} h_{ru}(t)dt. \tag{4-9}$$

N_r of relay terminal r can be given as:

$$N_r = N_{bn_r} + N_{sig_r} + N_{AMP} + N_{LED}, \tag{4-10}$$

where $N_{bn_r} = 2q\,\eta_g^2 G_A^2\, R_r P_{bn_r}$, corresponds to the ambient light noise at relay terminal r, $N_{sig_r} = 2q\,\eta_g^2 G_A^2 R_r P_{signal_r}$, is the shot noise related to the received signal at relay terminal r, $N_{AMP} = \eta_g^2 G_A^2 j_c^2$, is the shot noise due to the electrical amplifier and $N_{LED} = 2q\theta < i_{out} >$, is the shot noise corresponding to the LED emitter of the O-E-O relay terminal [104]. R_r is the responsivity of relay terminal r, θ is relative to the shot noise level and the external quantum efficiency η_g of the relay terminal, j_c is the equivalent input noise current in $(A/\sqrt{Hz})$ of the amplifier, P_{bn_r} is the received ambient light power by relay terminal r and P_{signal_r} is the received signal power by relay terminal r. Therefore, Equation (4-10) can be rewritten as the following [104]:

$$N_r = 2q\eta_g^2 G_A^2 R_r P_{bn_r} + \eta_g^2 2qG_A^2 R_r P_{signal\ r} + \eta_g^2 G_A^2 j_c^2 + 2q\theta < i_{out} > \tag{4-11}$$

As $G_A \gg 1$ based on the result of [104], the term ($2q\theta < i_{out} >$) can be neglected. Therefore Equation (4-11) can be approximated as:

$$N_r \approx 2q\eta_g^2 G_A^2 R_r\left(P_{bn_r} + P_{signal_r}\right) + \eta_g^2 G_A^2 j_c^2 \tag{4-12}$$

4.2.2.2 SOA amplify-and-forward relay terminal

The structure of the SOA amplify-and-forward relay terminal is given in Fig. 4-3 [105]-[107]. At each SOA relay terminal, the incident light is focused and coupled into the optical fibre by a converging lens [105]. An SOA is then used to amplify the received optical field, and the amplified optical signal is forwarded to the user via a transmitting lens. Optical fibres are used to connect SOA with two lenses in order to meet the input and output interface requirements of the existing SOA. To discuss the SOA amplify-and-forward relay terminal in the same conditions, the influence of optical wireless transceiver lens and optical fibre of SOA relay terminal on the signal is neglected in the simulation. We assume that the SOA amplify-and-forward relay terminal is always operating in the unsaturated region to ensure that the amplifier operates in the linear amplification region [26].

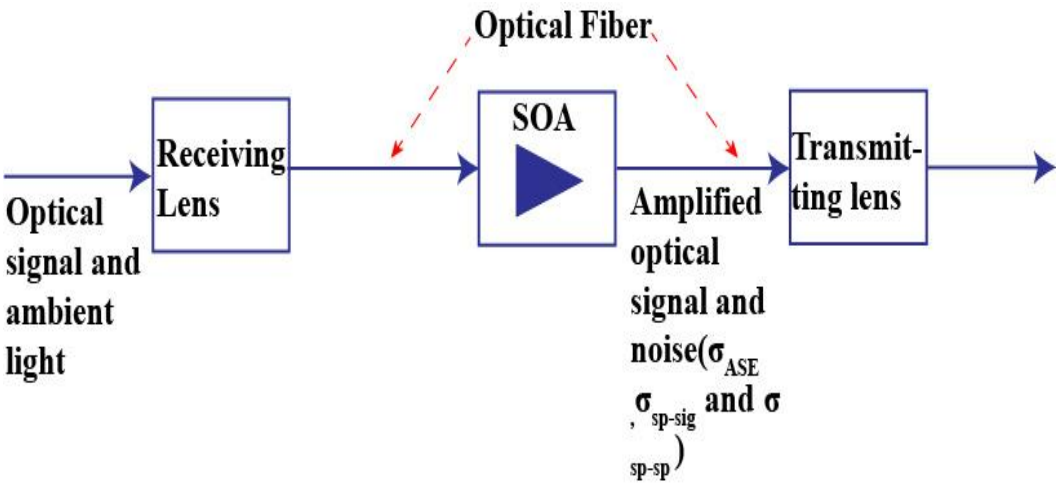

Figure 4- 3 SOA Amplify-And-Forward Relay Terminal.

SOA amplify-and-forward relay terminals, directly amplify the optical signal, $X(t)$, and hence, there is no responsivity, R_r, related to the conversion from optical signal to electrical signal. Thus, in the first phase, the received optical signal $P_r(t)$ at the SOA amplify-and-forward relay terminal r, can be given as:

$$P_r(t) = X(t) \otimes h_{sr}(t) + N_r(t) \tag{4-13}$$

In the second phase, the downlink photodetection current $I_u(t)$ at the user is defined as:

$$I_u(t) = R_u \sum_{r\in R} (G_s P_r(t) \otimes h_{ru}(t)) + N_u(t), \tag{4-14}$$

where R_u is the responsivity of the user's receiver, G_s is the amplifier gain of SOA relay terminal, $h_{ru}(t)$ is the impulse response from relay terminal r to the user, and $N_u(t)$ is the additive white Gaussian noise at the user's receiver. With SOA amplify-and-forward relay terminals, the SNR of a user can be given as Equation (4-3) while the noise components are defined as [26], [106]:

$$\begin{aligned} \sigma_{u0} &= \sqrt{\sigma_{s0,u}^2 + \sigma_{bn,u}^2 + \sigma_{pr,u}^2 + \sum_{r\in R} \sigma_{r,u}^2} \\ &= \sqrt{\sigma_{th,u}^2 + \sigma_{shot,u}^2 + \sigma_{sig-sp,u}^2 + \sigma_{sp-sp,u}^2} \\ and\ \ \sigma_{u1} &= \sqrt{\sigma_{s1,u}^2 + \sigma_{bn,u}^2 + \sigma_{pr,u}^2 + \sum_{r\in R} \sigma_{r,u}^2} \\ &= \sqrt{\sigma_{th,u}^2 + \sigma_{shot,u}^2 + \sigma_{sp-sp,u}^2 + \sigma_{sig-sp,u}^2} \end{aligned} \tag{4-15}$$

The noise components are described by the following noise variances that describe the thermal, shot, signal-spontaneous beat noise and spontaneous-spontaneous beat noise contributions as [107]:

$$\begin{aligned} \sigma_{th,u}^2 &= j_c^2 B_e, \\ \sigma_{shot,u}^2 &= 2qR_u B_e (P_{amb} + \textstyle\sum_r^R (P_{signal} + P_{ASE})), \\ \sigma_{sig-sp,u}^2 &= \frac{4R_u^2 \sum_{r\in R} P_{signal_r} \sum_{r\in R} (P_{ASE} H_{ru}(0))\, B_e}{B_o}, \\ \sigma_{sp-sp,u}^2 &= \frac{R_u^2 \left(\sum_{r\in R} P_{ASE} H_{ru}(0)\right)^2 (2B_o - B_e) B_e}{B_o^2} \end{aligned} \tag{4-16}$$

where B_e and B_o are electrical and optical bandwidth, respectively, j_c is an equivalent input noise current ($A/\sqrt{Hz}$) of the user's preamplifier, P_{amb} is the background light

power at the user, and P_{ASE} is the amplified spontaneous emission (ASE) power of relay terminal r which can be given as:

$$P_{ASE} = N_{sp}(G_s - 1)hfB_o, P_{ASE} = N_{sp}(G_s - 1)hfB_o, \quad (4\text{-}17)$$

where N_{sp} is the population inversion factor (amplifier excess noise factor) of the SOA relay terminal.

In addition to the noise due to the preamplifier (i.e., $j_c^2 B_e$), the SOA amplify-and-forward relay terminal experiences ambient light (i.e., $2qR_u B_e P_{amb}$) at the user's transceiver and the shot noises associated with receiving the signal (i.e., $2qR_u B_e P_{signal_r}$). Therefore, σ_r^2 can be given as:

$$\sigma_r^2 = 2qR_u B_e P_{ASE} + \frac{4R_u^2 P_{signal_r}(P_{ASE}H_{ru}(0))B_e}{B_o} + \frac{R_u^2(P_{ASE}H_{ru}(0))^2(2B_o - B_e)B_e}{B_o^2} \quad (4\text{-}18)$$

4.2.2.3 Decode-and-Forward (DF) relay terminal

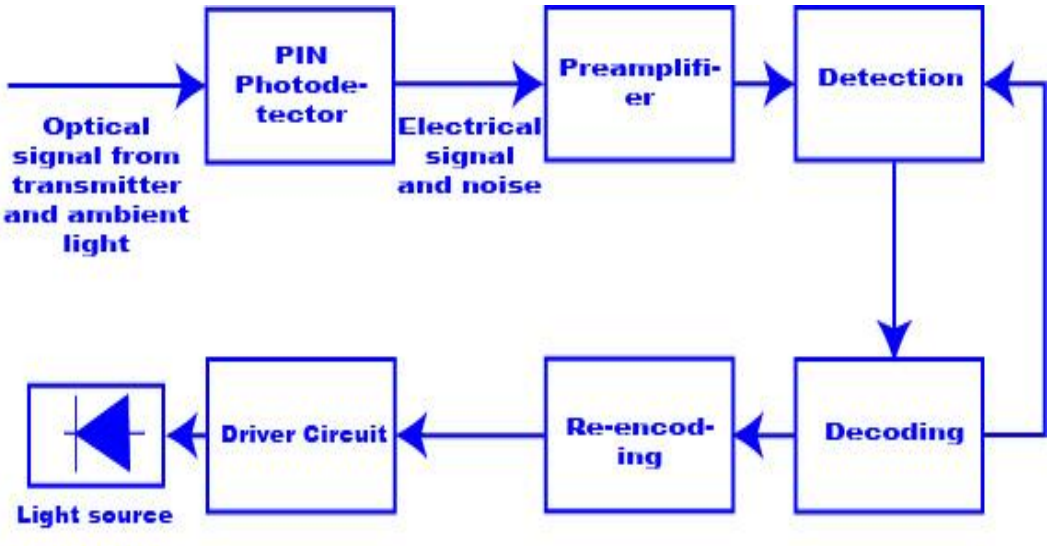

Figure 4- 4 Decode-And-Forward relay terminal.

The general structure of a DF relay terminal is given in Fig. 4-4. When Decode-and-Forward (DF) relay terminals are deployed, in the first phase, the photodetection current at relay terminal r is the same as in Equation (4-1). In first phase, the SNR of a DF relay terminal (SNR_r) is given as:

$$SNR_r = \left(\frac{R_r(P_{s1_r} - P_{s0_r})}{\sigma_{r1_r} + \sigma_{r0_r}}\right)^2 \tag{4-19}$$

where σ_{r0_r} and σ_{r1_r} are the noises associated with the received signal from the AP. When ignoring the part of the noise related to the signal, these noises can be computed as the following:

$$\sigma_{r1_r} = \sqrt{\sigma_{bn_r}^2 + \sigma_{pr_r}^2} \text{ and } \sigma_{r0_r} = \sqrt{\sigma_{bn_r}^2 + \sigma_{pr_r}^2} \tag{4-20}$$

where $\sigma_{bn_r}^2$ represents the background shot noise at the DF relay terminal receiver and $\sigma_{pr_r}^2$ represents the DF relay terminal preamplifier noise component. In the second phase, the photodetection current at the user is the same as in Equation (4-2). The SNR of the user (SNR_u) is updated as Equation (4-3), while the noise components are defined as:

$$\sigma_{u0} = \sqrt{\sigma_{bn}^2 + \sigma_{pr}^2} \text{ and } \sigma_{u1} = \sqrt{\sigma_{bn}^2 + \sigma_{pr}^2} \tag{4-21}$$

Note that, the sum of the noise components from all DF relay terminals is neglected as in the decode and re-encode process, the signal is reshaped to eliminate the influence of the noise and the multi path reflections. However, compared with amplify-and-forward relay terminals, a system with DF relay terminal faces the problem of error propagation due to decoding the signal at the relay terminals and again at the user's receiver. To avoid error propagation occurring, the bit error rate at any DF relay terminal should be lower than a minimum standard value ($P_e \leq 10^{-9}$) to guarantee acceptable communication performance [96].

To ensure that the total optical power received from all relay terminals is within eye safety power limitation, we normalise the average optical power of each relay terminal r (P_r) so that the summation of all normalised P_r values (i.e., $P_r^{'}$) is equivalent to the

average optical power of the AP (i.e., P_t). This excludes the influence of the differences in the optical power gain of the systems. To investigate the performance of different types of relay terminals we use the following Equation:

$$\sum_{r\in R} P_r^{'} = P_t \tag{4-22}$$

P_t is given as:

$$P_t = \lim_{T\to\infty} \frac{1}{2T} \int_{-T}^{T} X(t)\, dt. \tag{4-23}$$

When an OEO amplify-and-forward relay terminal is used, the average optical power of relay terminal r ($P_{r_{OEO}}$) is given as:

$$P_{r_{OEO}} = \lim_{T\to\infty} \frac{1}{2T} \int_{-T}^{T} \frac{hf}{q} \eta_g G_A I_r(t)\, dt \tag{4-24}$$

In order to equate total average optical power of all relay terminals to transmitter, the amplifier gain G_A of relay terminal r is defined as:

$$G_A = \frac{(\lim_{T\to\infty} \frac{1}{2T} \int_{-T}^{T} X(t)\, dt)}{(\sum_{r\in R} \lim_{T\to\infty} \frac{1}{2T} \int_{-T}^{T} \frac{hf}{q} \eta_g I_r(t)\, dt)} \tag{4-25}$$

When SOA amplify-and-forward relay terminal is used, the average optical power of relay terminal r ($P_{r_{SOA}}$) is given as:

$$P_{r_{SOA}} = \lim_{T\to\infty} \frac{1}{2T} \int_{-T}^{T} G_s P_{soa}(t)\, dt \tag{4-26}$$

The amplifier gain G_s of relay terminals r is given as:

$$G_s = \frac{(\lim_{T\to\infty} \frac{1}{2T} \int_{-T}^{T} X(t)\, dt)}{(\sum_{r\in R} \lim_{T\to\infty} \frac{1}{2T} \int_{-T}^{T} P_{soa}(t)\, dt)} \tag{4-27}$$

When DF relay terminal is used as the relay terminal r, the average optical power of relay terminal r, ($P_{r_{DF}}$) is given as:

$$P_{r_{DF}} = \frac{\lim_{T\to\infty} \frac{1}{2T} \int_{-T}^{T} X(t)\, dt}{N} = \lim_{T\to\infty} \frac{1}{2T} \int_{-T}^{T} X_r(t)\, dt \tag{4-28}$$

where N is the number of DF relay terminals deployed in the system.

4.2.3 The delay adaptation method in relay-assisted communication

We invoke the delay adaptation method to overcome the drawbacks of having different signals arrival time in the IR-based OWC systems with relay terminals. This method was first proposed in [12] where the authors decreased the time spread by adding differential delay to different beams.

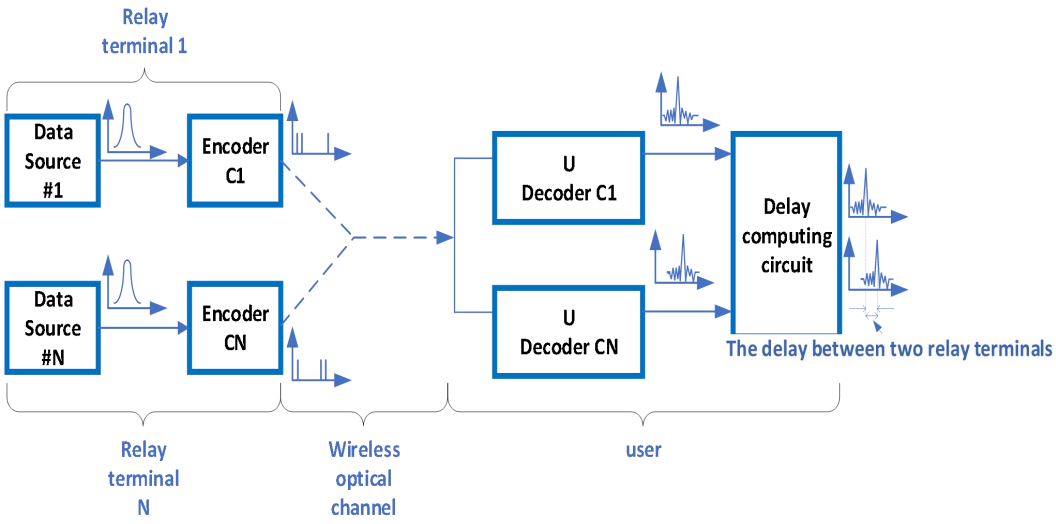

Figure 4-5 Description of the Delay Adaption Method Based on Optical Orthogonal Code Technique.

The method to achieve delay adaption is based on the optical orthogonal code technique in [80]. The relay terminals and the user synchronise at the start of a frame before the formal communication begins. Then, each relay terminal simultaneously sends a special impulse encoded with a unique optical orthogonal code sequence. The user can identify the signals from different relay terminals with relevant decoders due to

the auto and cross-correlation properties of the optical orthogonal code. Then, all decoded signals will be sent to a comparing circuit to compute the propagation delay between each pair of relay terminals. After the user computes the time delay of all relay terminals, a feedback message containing information about differential delay values is sent to each relay terminal via the uplink channel. The description of the delay adaptation method based on optical orthogonal code technique is shown in Fig. 4-5.

4.2.4 The impulse response and delay spread results for system with O-E-O amplify-and-forward relay terminal with and without delay adaptation method

To evaluate the advantages of the proposed method, a simulation was performed considering an empty room with dimensions of 8 m × 4 m × 3 m (length × width × height). The room setup is the same as the one described in Chapter 3. The transmitter is located at the centre of the ceiling while the user is in the communication plane which is 1m above the floor. The room set-up is showed in Fig. 4-6.

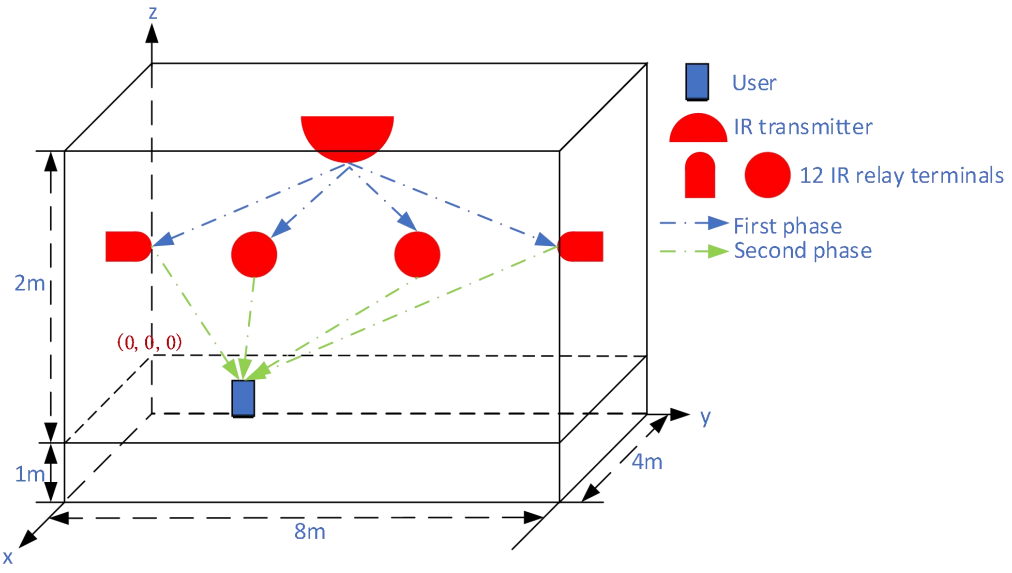

Figure 4- 6 The Room Set-Up of Simulation.

We consider three different scenarios of relay terminal deployments in which the O-E-O amplify-and-forward relay terminals are separately deployed 0.5 m, 1 m and 1.5 m under the ceiling around the walls. Each scenario contains 12 relay terminals. The distance between them is 1 m. Additional simulation parameters are given in Table 4-1.

Table 4- 1 Simulation Parameters

Parameter	Configuration	
IR Transmitter		
Quantity	1	
Location	(2, 4, 3)	
The average optical power	1W	
half-power semi-angle	60º	
Relay terminal locations		
Quantity	12	
Locations	The relay terminals of three scenarios are separately deployed 0.5m, 1m and 1.5m under the ceiling around the wall. Each scenario contains 12 relay terminals.	
Users		
Quantity	1	
Elevation	90º	
Azimuth	0º	
FOV	90º	
Resolution		
Time bin duration	0.1ns	
Bounces	1	2
Surface elements	32000	2000
Wavelength	850 nm	

In this simulation, only downlink is considered and the influence of the relay terminal type on the intensity and waveform of the received signal is ignored for simplification. The received signal of a user can be defined as followed:

$$I_r(t) = \sum_{r \in R} R(X(t) \otimes h_{tr}(t) \otimes h_{ru}(t)) \tag{4-29}$$

where R is the responsivity of the receiver, $X(t)$ is the instantaneous optical power at the transmitter, $h_{sr}(t)$ represents the channel impulse response for the channel between

the transmitter and the relay terminal, $h_{ru}(t)$ represents the impulse response for the channel between the transmitter and the relay terminal, and $\otimes$ represents convolution. The RMS delay spread, which is a good measure of the signal pulse spread is considered as the main performance indicator. Fig. 4-7(a) shows the RMS delay spread of the conventional relay system and the relay system with the delay adaptation method when the relay terminals are deployed at 0.5m, 1m, and 1.5m below the ceiling and the user moves along the Y axis with x=1m. Fig. 4-7(b) shows the RMS delay spread results with x=2m. The results show that the RMS delay spread of the IR relay system with the delay adaptation method are lower than the conventional IR relay system in different scenarios.

Fig. 4-8(a) shows the impulse response of conventional relay system and the relay system with the delay adaptation method when relay terminals are deployed at 0.5m and the user is at the room corner (1,1,1). Fig. 4-8(b) shows the impulse response of the conventional relay system and the relay system with the delay adaptation method when relay terminals are deployed at 1 m below the ceiling and the user is at the room corner (1,1,1). Fig. 4-8 (c) shows the impulse responses of the conventional relay system and the relay system with the delay adaptation method when the relay terminals are deployed at 1.5m and the user is at the room corner (1,1,1). The pulse spread of the IR relay system is effectively reduced by the delay adaption method for the different deployment.

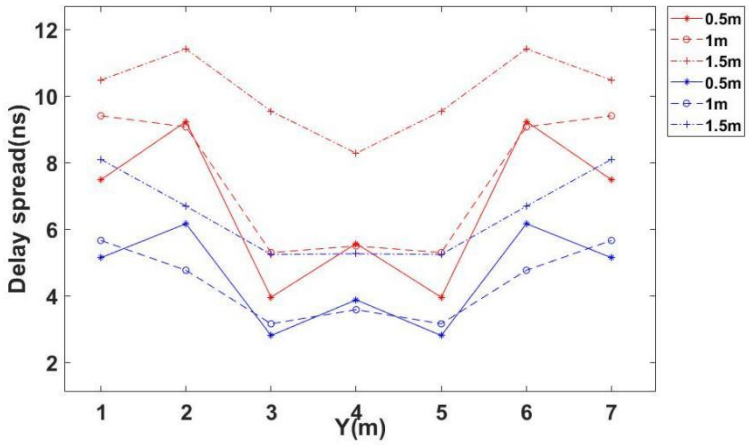

(a)

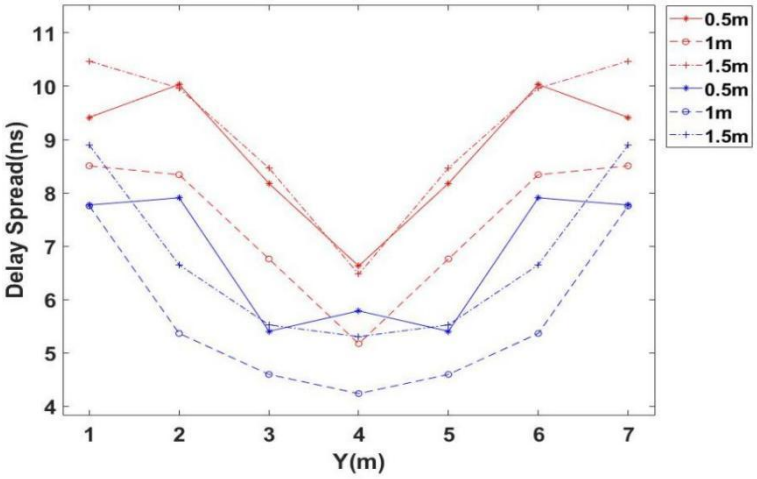

(b)

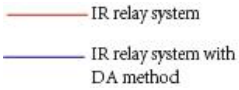

Figure 4- 7 The root-mean-square delay spread results for (a) x=1m (b) x=2m.

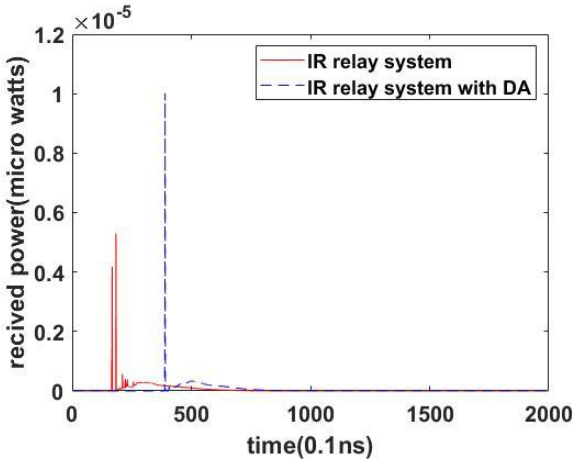

(a)

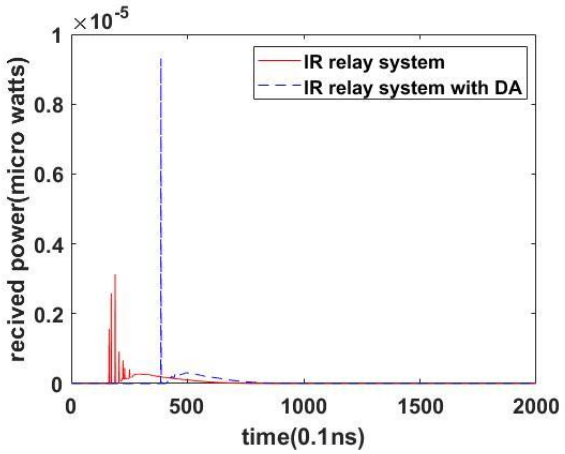

(b)

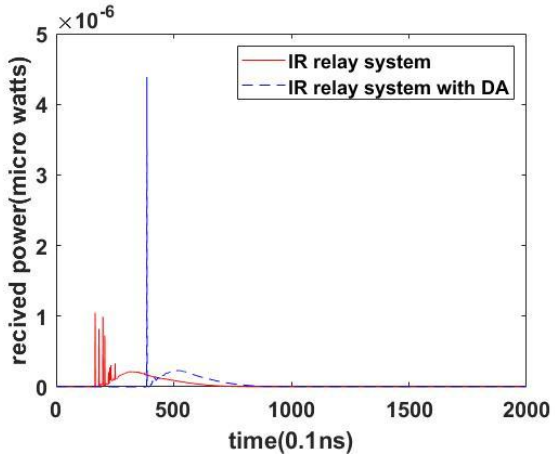

(c)

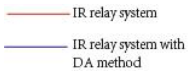

Figure 4- 8 The Impulse Response Results in the Conventional IR Relay System and the IR Relay System With the Delay Adaption (D) Method (A) relay terminals are deployed at 0.5 m below the ceiling, (B) relay terminals are deployed at 0.5 m below the ceiling, And (C) relay terminals are deployed at 0.5 m below the ceiling.

4.3 The SNR simulation results of three different types of relay terminals based on the delay adaptation method

4.3.1 The simulation setup

To evaluate the SNR performance of the delay adaptation method in an indoor IR-based OWC system, we consider the same empty room in Section 4.2.3 with the dimensions of 8 m × 4 m × 3 m (length × width × height). The configuration of the room is the same as the room setup in Chapter 3.

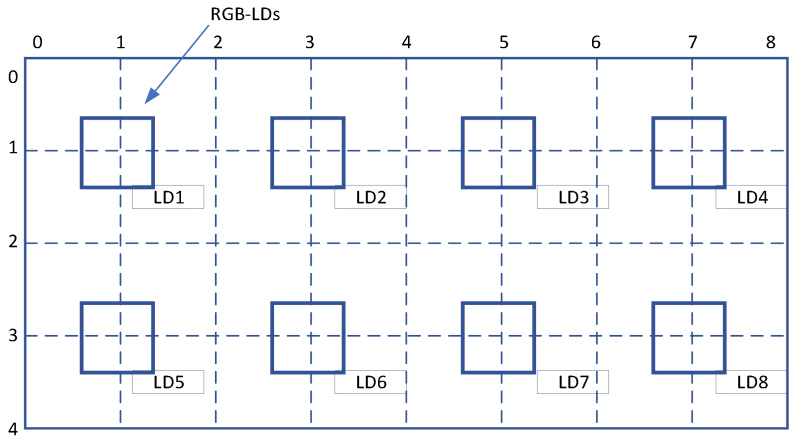

Figure 4- 9 The Locations of RGB-LDs on the Ceiling.

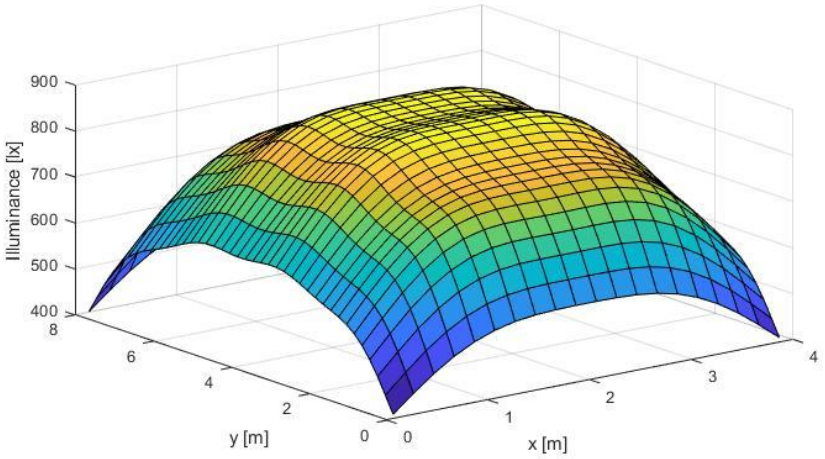

Figure 4- 10 The Distribution of Horizontal Illumination on the Communication Floor.

In the considered room, eight RGB-LDs are mounted on the ceiling [108], [109]. The locations of the eight RGB-LDs are given in Fig. 4-9 [110], [111] while the distribution of illumination on the communication floor is shown in Fig. 4-10. The parameters in Table 4-2 are considered. Fig. 4-10 shows that the illumination in the room achieves the EU standard for comfortable office lighting (i.e., 300 lux to 1500 lux) [112], [113]. The RGB-LDs impact the SNR performance of the IR-based OWC system with relay terminals because the power detected by the photodetector of the receiver from the visible light frequency band is counted as background shot noise as in Equation (4-4).

To fully evaluate the function of the relay terminal, we consider two different scenarios:

1) In the first scenario, the AP is mounted at the centre of the ceiling (i.e., at location (2m, 4m, 3m) while the user can be in one of 21 positions on the communication plane. In this scenario, there is a direct link between the AP and the user.

2) In the second scenario, the AP is located at the centre of the communication plane (i.e., at location (2m, 4m, 1m) as in [10] and [12] while the user is also located as in the first scenario.

In the following, we consider three different relay terminals deployment schemes in which the relay terminals are separately deployed at 0.5m, 1m and 1.5 m below the ceiling. For the two scenarios to investigate the influence of the location, number and type of relay terminal on the communication, each scheme contains 6 or 12 relay terminals where the distance between terminals is 4m and 2m, respectively.

The delay adaptation method proposed in the last section is applied to all deployment schemes. The external quantum efficiency η_g of the OEO-relay terminal is given as 0.95 [114]-[116]. The N_{sp} of SOA-relay terminal in this simulation is set as in [107]. The amplifier used in this study is the positive-intrinsic negative-bipolar junction transistor (PIN-BJT) design proposed in [116] and [117]. This preamplifier has a noise current density of 2.7 $pA/\sqrt{Hz}$. The SNR of the uplink and downlink are evaluated with different user locations on the communication plane. Additional simulation parameters are given in Table 4-2.

Table 4- 2 Simulation Parameters for Three Different Kinds of Relay Terminals

Parameter	Configuration	
IR AP		
Quantity	1	
external quantum efficiency	0.95	
Location	(2, 4, 3) or (2, 4, 1)	
The average optical power	1W	
half-power semi-angle	60º	
Relay terminal locations		
Quantity	6 or 12	
Locations	The relay terminals of the three scenarios are deployed 0.5m and 1.5m under the ceiling around the walls.	
Photodetector		
FOV	90º	
area	1 cm^2	
The responsivity of IR communication	0.5 A/W	
The responsivity of illumination	0.4 A/W	
Users		
Quantity	1	
Elevation	90º	
Azimuth	0º	
FOV	90º	
Resolution		
Time bin duration	0.1 ns	
Bounces	1	2
Surface elements	32000	2000
Wavelength	850 nm	

4.3.2 SNR simulation results

Fig. 4-11 and 4-12 show the SNR of the downlink when the user moves on the communication plane along the Y-axis in the first scenario (i.e., the AP is in the centre of the ceiling) while x equals 1m and 2m, respectively. These two X-axis locations are considered to examine the SNR when the user is at different distances from the wall. The first value locates the user closer to the wall while the second value locates the user closer to the centre of the room. We can see that using relay terminals generally results in worse performance compared to the system without relay terminals (i.e., the black curve results in Fig. 4-11 and 4-12) especially when the user is closer to the centre of the room (i.e., Y-axis coordinates between 2m and 6m). Considering the type of relay terminals, the systems with SOA and O-E-O amplify-and-forward relay terminals were found to experience more distortion compared to DF relay terminals (i.e., the results in the purple and red curves) due to the lack of the reshape function. Meanwhile, the results of the system with SOA amplified-and-forward relay terminals are slightly better than the results of the system with O-E-O amplified-and-forward relay terminals, as the impact of ambient light on SOA is comparatively limited compared to OEO amplifiers. This is primarily because the spectrum bandwidth of SOA amplifiers is typically narrower than that of OEO amplifiers. For the location of relay terminal, comparing the curves in the same colour, the system with relay terminals deployed at 1.5m below the ceiling have better performance compared with the system with relay terminal deployed at 0.5m below the ceiling when the user moves on the $x = 2m$ axis as in Fig. 4-12.

For the $x = 2m$ case, although the delay adaptation method improves the delay spread by 30%, some different impacts due to distance differences are experienced. The distances between relay terminals and the user are similar due to the axial symmetry which reduces the difference of the signal arrival times from different relay terminals. The relay terminals deployed at 1.5m below the ceiling are closer to the communication plane which causes the user to receive more power from the relay terminal via the direct link. However, when the user moves on the $x = 2m$ axis, the axial symmetry does not exist. The distortion due to the different signal arrival time dominates and influences the

SNR of the user resulting in the fluctuations in Fig. 4-11. Considering the number of relay terminal, the SNR attenuation is more visible for the system with 6 relays terminals when the user moves to the middle of Y axis than the attenuation in the system with 12 relay terminals given that the same type of relay terminal. When 12 relay terminals are deployed, the distance between them is reduced and therefore some of them are deployed closer to the midpoint of Y-axis and hence the SNR is improved.

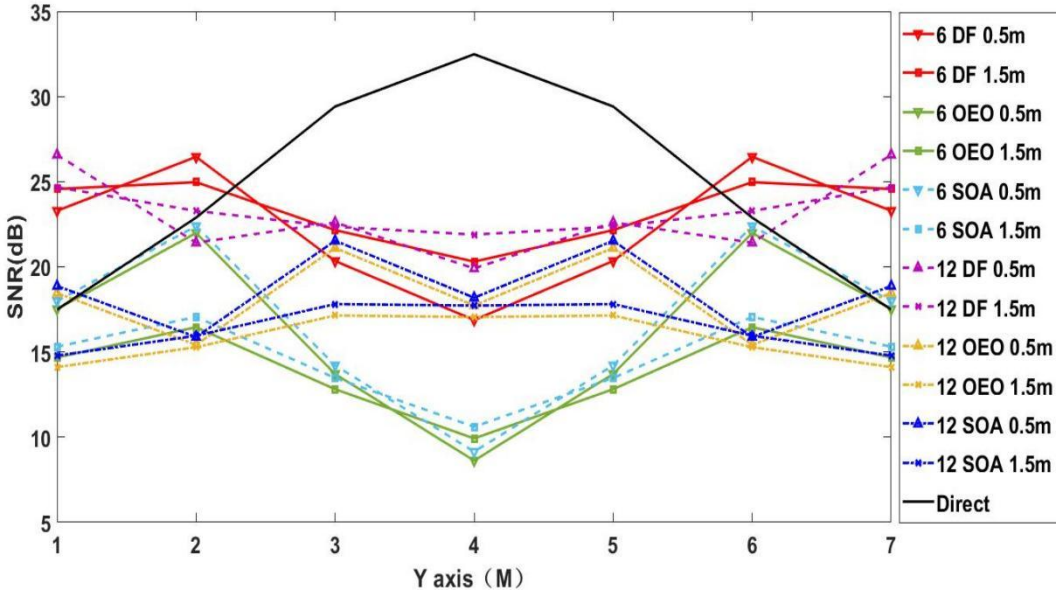

Figure 4-11 The SNR of Downlink when the User Moves Along the Y-Axis， on the *X=1m* Axis, in the First Scenario.

Fig. 4-13 and Fig. 4-14 show the SNR of the downlink when the user moves on the communication plane along the Y-axis in the second scenario (i.e., the AP is in the centre of the communication plane) with x equals 1m and 2m. The system without relay terminals has slightly better performance when the Y-axis coordinate is between 3m and 5m (i.e., around the centre of the room) compared with the system with relay terminals.

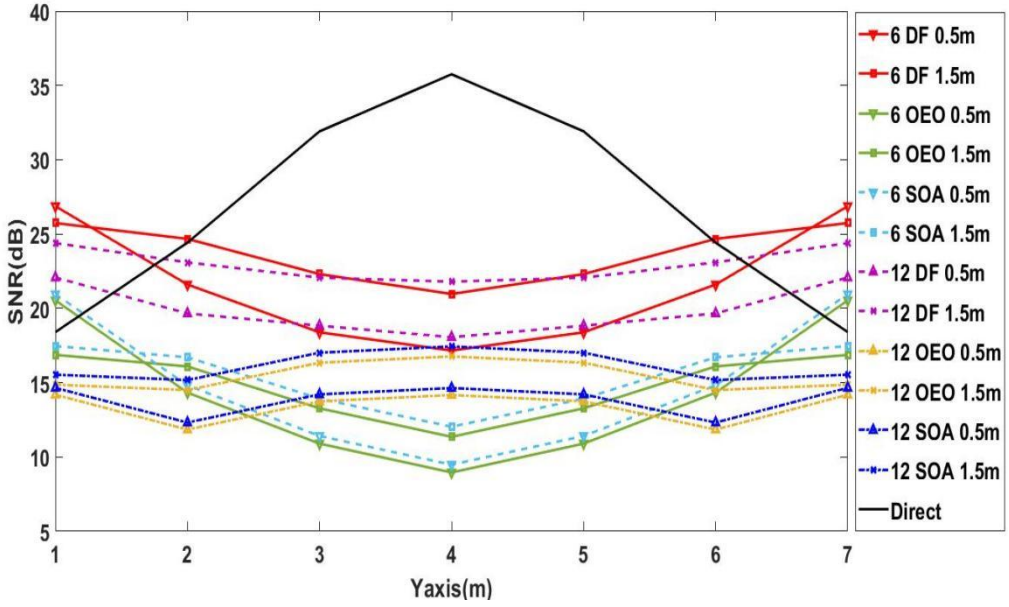

Figure 4- 12 The SNR of Downlink when the User Moves Along the Y-Axis, on the *X=2m* Axis, in the First Scenario.

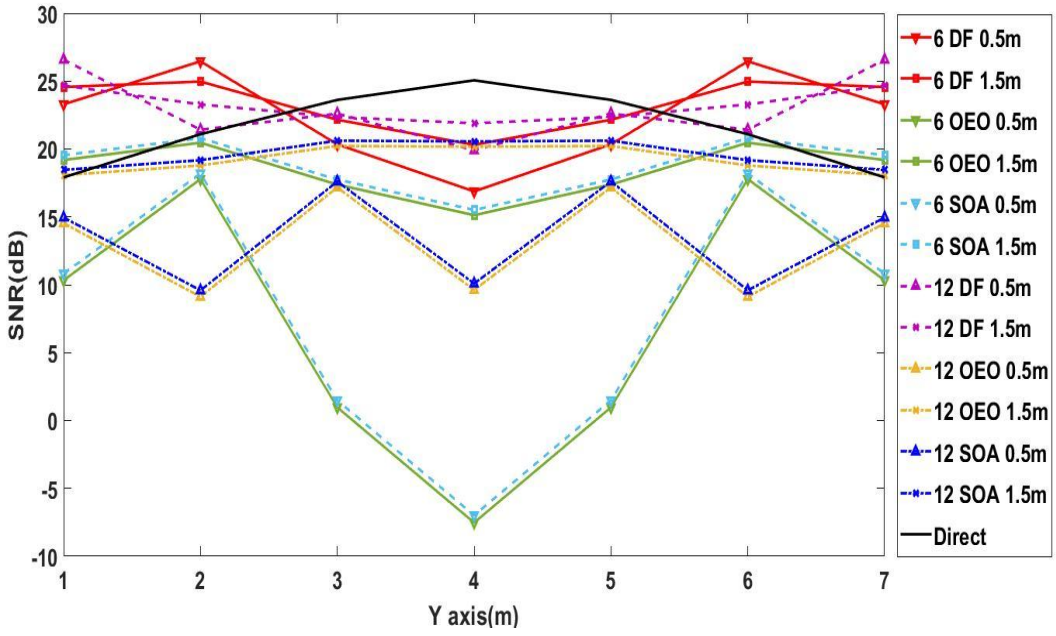

Figure 4- 13 The SNR of Downlink when the User Moves Along the Y Axis on the *X=1m* Axis, in the Second Scenario.

Considering the type of the relay terminal, the SNR of the system with DF relay terminal is higher than the system with OEO or SOA relay terminal when the quantity and location of the relay terminals are the same. Considering the location of the relay terminals, when other conditions are the same, the system with relay terminals deployed at 1.5 m below the ceiling has better performance compared with the system with relay terminal deployed at 0.5 m below the ceiling when the user moves on the $x = 1m$ axis or the $x = 2m$ axis.

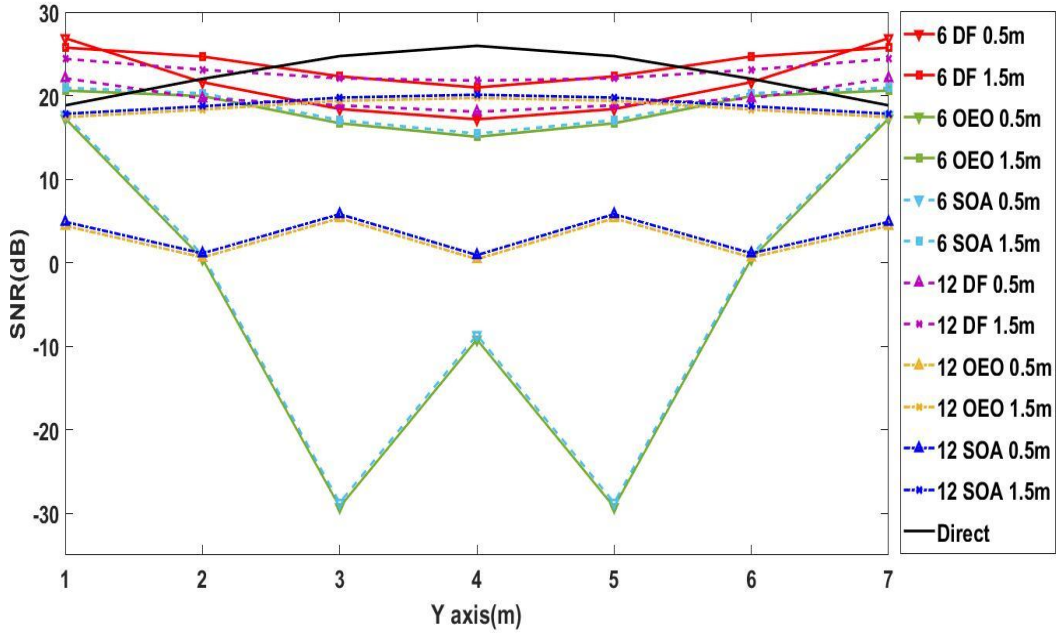

Figure 4- 14 The SNR of Downlink when the User Moves Along the Y Axis on the *X=2m* Axis, in the Second Scenario.

It is different from first scenario in that the AP and the receiver are in the same plane in the second scenario. The relay terminals deployed at 1.5 m below the ceiling get closer to both transmitter and user. Therefore, the relay terminal can receive more power from transmitter via direct links and the user can also receive more power from the relay terminals. The enhanced power at the relay terminal and the user improves the SNR at the user. Considering the number of relay terminals, except for the DF relay terminal, the curve of the system with 6 relay terminal experience more fluctuation than the curve of the system with 12 relay terminals when other conditions are the same.

Fig. 4-15 and 4-16 show the SNR of the uplink when the user moves on the communication plane in the first scenario. Similar to the downlink results in Fig. 4-11 and 4-12 for the first scenario, the system without relay terminals generally has better SNR results. The user location has no major influence on the performance of the system with DF relay terminals because the location of the AP is fixed, and the system can correct the distortion and attenuation of the first phase that are associated with the relay location.

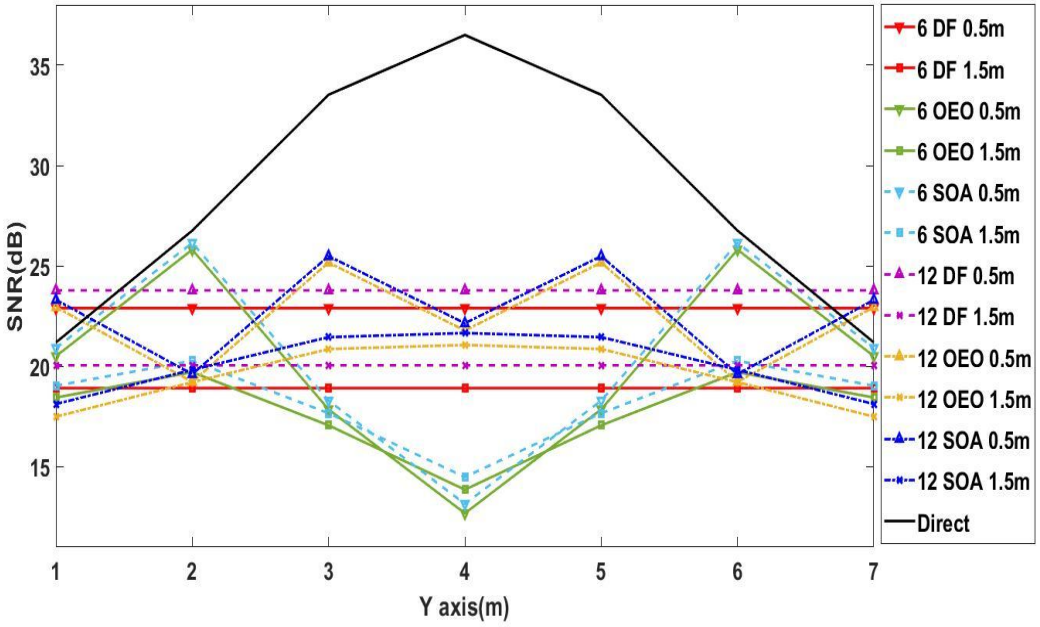

Figure 4-15 The SNR of Uplink when the User Moves Along the Y Axis on the *X=1m* Axis, in the First Scenario.

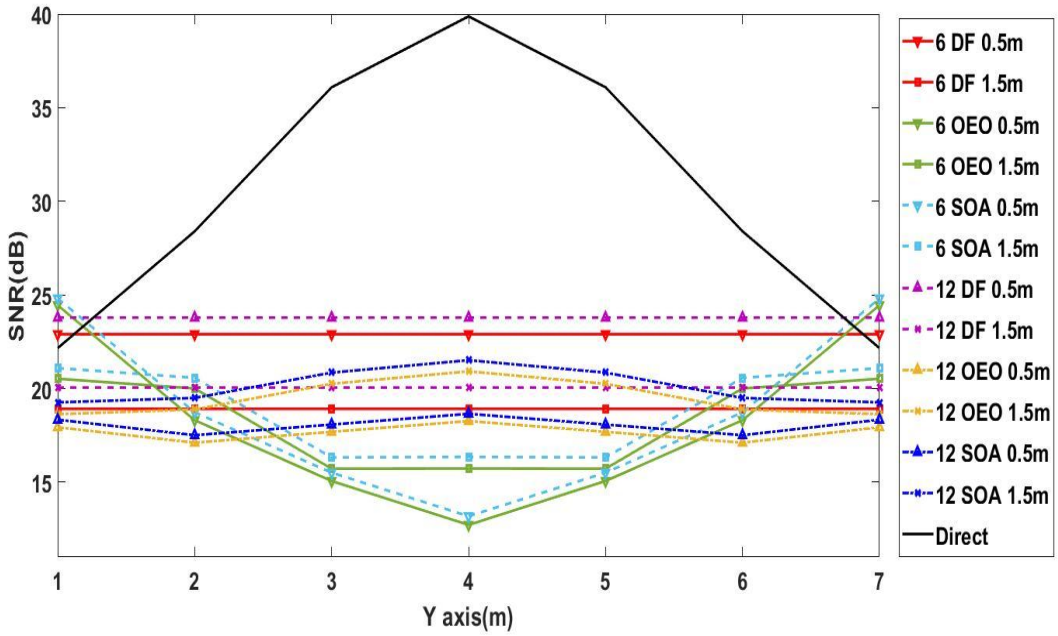

Figure 4-16 The SNR of Uplink when the User Moves Along the Y Axis on the *X=2m* Axis, in the First Scenario.

Fig. 4-17 and 4-18 show the SNR of the uplink when the user moves on the communication plane along the Y-axis in the second scenario. Compared with the curves of the downlink in Fig. 4-11, 4-12, 4-13 and 4-14 the curves of downlink and uplink of the system with SOA or OEO relay terminals possess similar fluctuations (values are different). These fluctuations are a result of the influence of the arrival time and signal distortion due to the location and number of relay terminals. We can see that the system with DF relay terminals has an advantage at the corner of the room compared to the system without relay terminals. Compared with the first scenario, the best SNR result of the system with DF relay terminals at 1.5m below the ceiling gets closer to the result of the system without relay terminal, when user is moving along the $x = 1\ and\ 2m$.

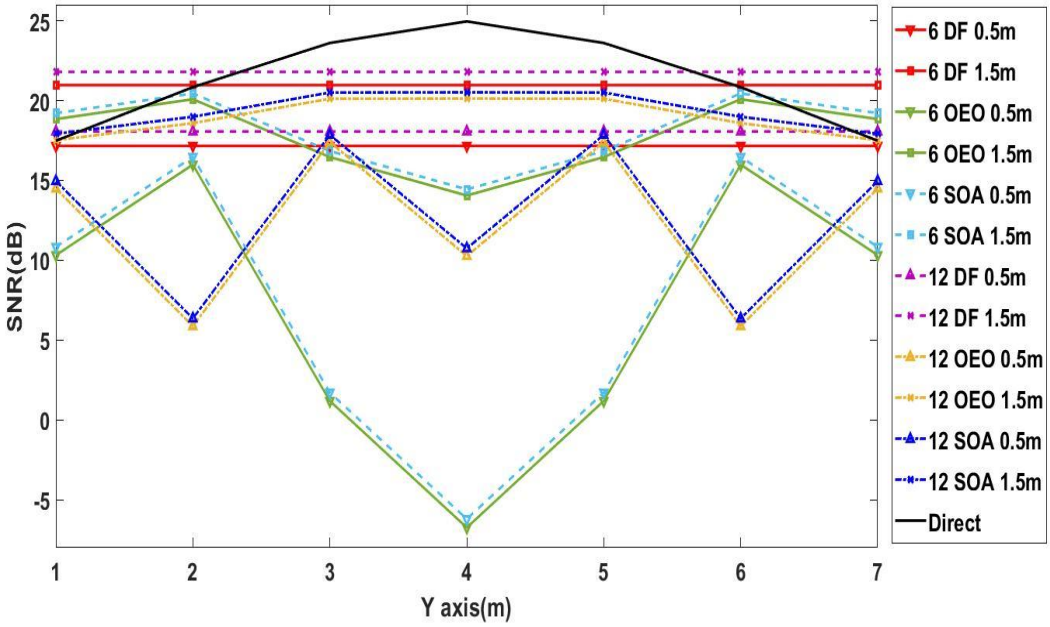

Figure 4- 17 The SNR of Uplink When the User Moves Along the Y Axis on the *X=1m* Axis, in the Second Scenario.

Based on the second scenario results, better SNR values are achieved when the relay terminals are placed closer to the AP and the user. However, when the user and the AP are in different planes as in the first scenario, the influence of the relay terminals height is not clear as in the second scenario. In the uplink, the access point's location remains constant, allowing for the attenuation and distortion in the third phase to be corrected using the reshape, re-timing, and amplification function of the DF relay terminal. Additionally, the attenuation and distortion caused by the location and quantity of relay terminals in the fourth phase are fixed, making it relatively easy to determine an optimal allocation scheme for the relay terminals. However, in the downlink, the optimal deployment scheme for relay terminals must consider the impact of both the quantity and location of relay terminals on different user locations in the second phase. This requires balancing the influence of relay terminals on various user locations. The optimal allocation scheme for relay terminals in the downlink and uplink, taking into account different user locations, is discussed in detail as a multiple constraints and large optimization problem in next chapter.

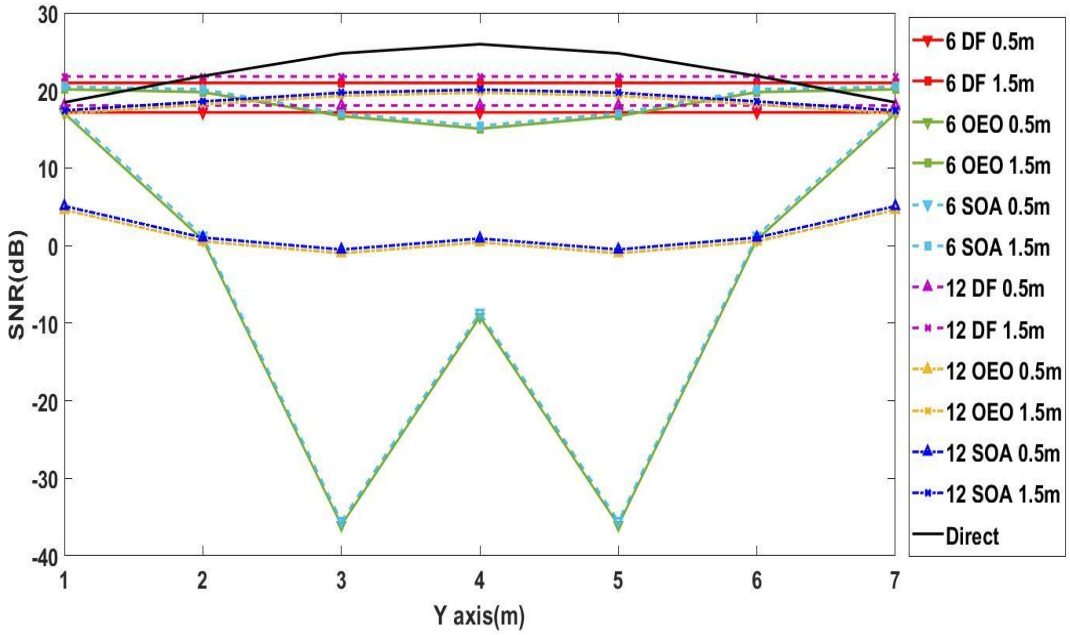

Figure 4- 18 The SNR of Uplink when the User Moves Along the Y Axis on the *X=2m* Axis, in the Second Scenario.

4.4 Summary

In this chapter, a four-phase relay assisted OWC system based on the CDS is proposed. We considered three different types of relay terminals including the O-E-O amplify and forward, the SOA amplify and forward, and the DF relay terminal. The noise calculations and channel models of the three types are presented. To reduce the ISI due to multiple relay terminals, a delay adaption method is applied. The results show that the RMS delay spread of relay terminals with the delay adaptation method is 30% less than the relay terminals without the delay adaptation method. Considering the delay adaptation method, the SNR performance of the different types of relay terminals is evaluated in different scenarios. The results show that the DF relay terminal has better SNR performance in different scenarios compared with the other two types of relay terminals. Hence, general rules about optimal relay terminal deployments cannot be provided. In the following chapter, we develop a MILP model to optimise the relay deployment (i.e., the locations and type of relay terminals) in OWC systems. This

model can be used to determine the best relay deployments under several AP and receiver location scenarios.

Chapter 5: Optimising the locations and type of different relay terminals in relay assisted OWC system

5.1 Introduction

In the previous chapter, a relay assisted OWC system based on a CDS system was introduced. Different relay terminal deployment schemes were evaluated in different IR AP location scenarios. The influence of the number and location of relay terminals on the SNR performance of the OWC system was investigated. In this chapter, we propose an Optimised Relay Terminal Allocation (ORTA) method in Section 5.2 to optimise the type and location of activated relay terminals with the objective of maximising the sum of the uplink and downlink SNR under different user locations in the communication plane. In Section 5.2, the details of the ORTA method (i.e., the MILP model and its sets, parameters, variables, objective function, and constraints) are introduced. The optimisation results comparing a relay assisted OWC system optimised using ORTA to the relay terminal deployment schemes in Chapter 4 are presented in Section 5.3. This chapter is concluded in Section 5.4.

5.2 ORTA

We develop a MILP model to determine the optimum relay terminal deployment for an indoor environment. This model selects the optimal location and relay type when considering a certain number of active relay terminals with the objective of maximising the sum of uplink and downlink SNR values at different user locations in the communication plane for the user. We optimise the location and type of relay terminals considering different number of active relay terminals. We considered 81 candidate locations for deploying three types of relay terminals. The distance between them is 1m. There are 21 test points for the user location on the communication plane. The locations of the user test points, and the candidate user locations are shown in Fig. 5-1.

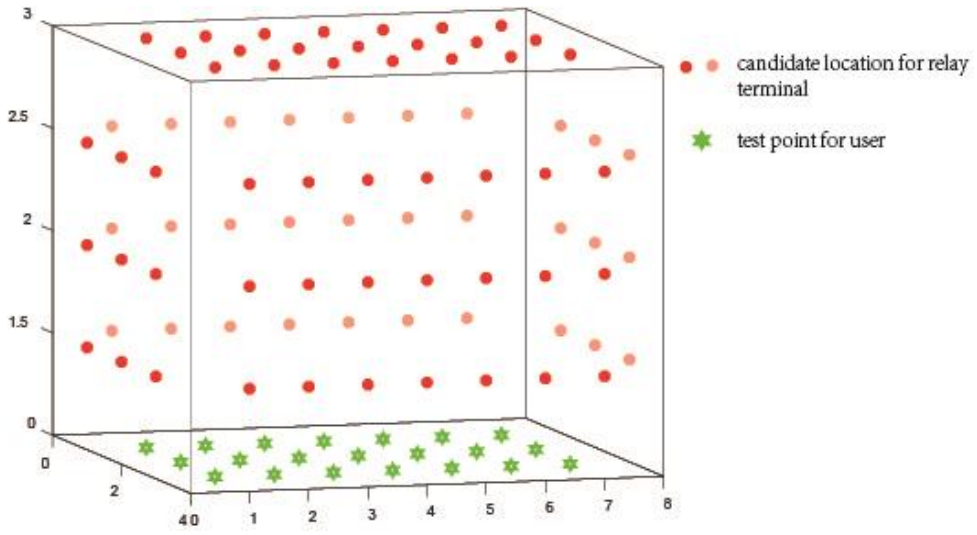

Figure 5- 1 The candidate locations for relay terminals on the walls and ceiling and test points for the user on the communication floor in the room.

The sets, parameters and variables of ORTA MILP model are provided below, followed by the objective and the constraints.

Table 5- 1 Sets of ORTA:

T	Set of different types of relay terminals including O-E-O amplify-and-forward, SOA amplify-and-forward and DF relay terminal.
U	Set of user locations in the room.
N	Set of candidate locations for the relay terminals in the room.
K	Set of indices of break points of piecewise-linearisation.

Table 5- 2 Parameters of ORTA

t	Relay terminal type index, $t \in T$.
u	User location index, $u \in U$.
n	Relay terminal location index, $n \in N$.
δ_u^{AMP}	The preamplifier noise for the user at location $u, u \in U$.
δ_u^{AL}	The ambient light shot noise for the user at location u, $u \in U$.

	This is precalculated using the ray tracing channel model, discussed in Chapter 3, with LOS, first and second reflections.
ξ^{AMP}	The preamplifier noise of the AP.
ξ^{AL}	The ambient light shot noise at the AP. This is precalculated using the ray tracing channel model, discussed in Chapter 3, with LOS, first and second reflections.
I_{tnu}	The received signal current produced by the user at location $u, u \in U,$ related to the downlink signal from candidate relay candidate location $n, n \in N,$ deploying a relay terminal of type $t, t \in T$. I_{tnu} is the multiplication of the responsivity of the user receiver and the received optical power which is precalculated based on the ray tracing algorithm.
R_{tnu}	The noise power of the user at location $u, u \in U,$ related to the downlink signal from candidate relay candidate location $n, n \in N,$ deploying a relay terminal of type $t, t \in T$. This value is precalculated based on the ray tracing algorithm.
P_{nu}	The received signal current produced by the user at location $u, u \in U,$ related to the uplink signal from candidate relay candidate location $n, n \in N,$ deploying a relay terminal of type $t, t \in T$. P_{tnu} is the multiplication of the responsivity of the user receiver and the received optical power which is precalculated based on the ray tracing algorithm.
E_{tnu}	The noise power of the user at location $u, u \in U,$ related to the uplink signal from candidate relay candidate location $n, n \in N,$ deploying a relay terminal of type $t, t \in T$. This value is precalculated based on the ray tracing algorithm.
M	The number of relay terminals.
β	Large enough number.
Q	The SNR threshold to guarantee a bit error rate $P_e \leq 10^{-9}$, $Q = 36.31 \equiv 15.6\ dB$
a_k	The break points of the non-linear function to be linearised,

	$k \in K$.
L	The total number of the pieces used in the piecewise-linearisation. (i.e., $k = 1,2,3, ..., L$)
X_{nu}	The SNR of downlink at relay candidate location $n, n \in N$, considering DF relay terminals.
Y_{nu}	The SNR of uplink at candidate relay location $n, n \in N$, considering DF relay terminals.

Table 5- 3 Variables of ORTA:

S_{tn}	A binary variable that is equal to 1 if the downlink and uplink of the communication go through relay terminal of type $t, t \in T$ at candidate location $n, n \in N$ and is equal to zero otherwise.
O	The sum of uplink and downlink SNR of the system for all user locations.
γ_u	The SNR of downlink at user location $u, u \in U$.
θ_u	The SNR of uplink at the receiver at the AP from a user at location u, $u \in U$.
Φ_{tnu}	A non-negative linearisation variable where $\Phi_n = S_{tn}\gamma_u$. This value reflects the SNR of downlink at user location $u, u \in U$ if relay terminal of type $t, t \in T$ deployed at candidate location $n, n \in N$ is selected for the communication.
τ_{tnu}	A non-negative linearisation variable where $\Phi_{tnu} = S_{tn}\gamma_u$. This value reflects the SNR of uplink at user location $u, u \in U$ if relay terminal of type $t, t \in T$ deployed at candidate location $n, n \in N$ is selected for the communication.
t_{ku}	A variable related to the break point $k, k \in K$ of the quadratic term of downlink for a user at location $u, u \in U$.
v_{ku}	A variable related to the break point $k, k \in K$ of the quadratic term of uplink for a user at location $u, u \in U$.
y_{ku}	A binary variable related to the adjacent break points selected to represent the value of the linearised function of downlink for a

	user at location k ∈ K, $u, u \in U$.
z_{ku}	A binary variable related to the adjacent break points selected to represent the value of the linearised function of uplink for a user at location $k \in K, u, u \in U$.

The objective of ORTA is to maximise O which is equals to the sum of uplink and downlink SNR of the system for all user locations given as:

$$Maximize\ O = \left(\sum_{u \in U} \gamma_u + \sum_{u \in U} \theta_u\right) \tag{5-1}$$

The SNR calculations of uplink and downlink are as follows:

Based on Equation (4-3), the downlink SNR for the user at location u (γ_u) is defined as:

$$\gamma_u = \left(\frac{R_u \sum_r^R (P_{s1} - P_{s0})}{\sigma_{u0} + \sigma_{u1}}\right)^2, \ \forall u \in U \tag{5-2}$$

We use the ray tracing algorithm to pre-calculate the signal current $I_{tnu} = R(P_{s1} - P_{s0})$ and hence Equation (5-2) can be rewritten as:

$$\gamma_u = \frac{\left(\sum_{t \in T} \sum_{n \in N} I_{tnu} S_{tn} \frac{1}{M}\right)^2}{\delta_u^{AMP} + \delta_n^{AL} + \sum_{t \in T} \sum_{n \in N} R_{tnu} S_{tn}}, \ \forall u \in U \tag{5-3}$$

where the numerator represents the sum of received optical power from different relay terminals. In the denominator, $\delta_u^{AMP} = \sigma_{pr}^2$ is the preamplifier noise of the user, $\delta_u^{AL} = \sigma_{bn}^2$ is the shot noise due to ambient light, $\frac{1}{M}$ is used to restrict the total optical power of all active relay terminals to 1 W, and $\sigma_r^2 = R_{tnu}$ is the shot noise for the downlink going through relay terminal of type t at candidate location n. For the OEO and SOA relay terminal types, the value of R_{tnu} is precalculated based on Equations (4-7) and (4-17). Considering that the DF relay terminal can retime and reshape the signal, the R_{tnu} of DF relay terminal is set to zero. Equation (5-3) can be rewritten as:

$$\delta_u^{AMP}\gamma_u + \delta_u^{AL}\gamma_u + \sum_{t\in T}\sum_{n\in N} R_{tnu}S_{tn}\gamma_u = (\sum_{t\in T}\sum_{n\in N} I_{tnu}\, S_{tn}\frac{1}{M})^2, \forall u \in U \qquad (5\text{-}4)$$

The third term in the left side of Equation (5-4) is a nonlinear quadric term containing a multiplication of a continuous variable by a binary variable. To linearise Equation (5-4), an alternative non-negative linearisation variable, $\Phi_{tnu} = S_{tn}\gamma_u$ is used. The inequalities that define the linearisation are as follows [117]:

$$\begin{gathered} \Phi_{tnu} \le \beta S_{tn} \\ \Phi_{tnu} \le \gamma_u \\ \Phi_{tnu} \ge \beta S_{tn} + \gamma_u - \beta \\ \forall t \in T, \forall n \in N, \forall u \in U, \end{gathered} \qquad (5\text{-}5)$$

where β is a large enough number. Therefore, Equation (5-4) can be rewritten as:

$$\delta_u^{AMP}\gamma_u + \delta_u^{AL}\gamma_u + \sum_{t\in T}\sum_{n\in N} R_{tnu}\Phi_{tnu} = (\sum_{t\in T}\sum_{n\in N} I_{tnu}\, S_{tn}\frac{1}{M})^2,\ \forall u \in U \qquad (5\text{-}6)$$

The quadratic term in the right-hand side Equation (5-6) can dramatically increase the computing complexity so we linearise the quadratic term using the piecewise-linearisation method in [118], and [119] used to linearise $f(x)$. In our work, $\sum_{t\in T}\sum_{n\in N} I_{tnu}\, S_{tn}\frac{1}{M}$ represent x and $(\sum_{t\in T}\sum_{n\in N} I_{tnu}\, S_{tn}\frac{1}{M})^2$ represents $f(x) = x^2$. We break the root axis of the quadratic term (i.e., $(\sum_{t\in T}\sum_{n\in N} I_{tnu}\, S_{tn}\frac{1}{M})^2$) into L pieces. We use $a_k (k \in K)$ to denote the break points of the quadratic term where $a_1 < a_1 < a_2 \cdots < a_L$. To linearise the quadratic term we use the following Equations [118], and [119]:

$$\left(\sum_{t\in T}\sum_{n\in N} I_{tnu}\, S_{tn}\frac{1}{M}\right)^2 \approx \sum_{k\in K} (a_k)^2\, t_{ku}, \qquad (5\text{-}7)$$

$$\sum_{t\in T}\sum_{n\in N} I_{tnu}\, S_{tn}\frac{1}{M} = \sum_{k\in K} a_k t_{ku}\,,$$

$$\sum_{k\in K} t_{ku} = 1\ \forall u \in U.$$

Only two adjacent t_{ku} values should be nonzero [118], [119]. To ensure this, t_{ku} is restricted by the following equations:

$$t_{ku} \leq \begin{cases} \leq y_{ku} & for\ k = 1 \\ y_{k-1,u} + y_{ku} & for\ k = 2,3,\cdots L-1\,, \\ \leq y_{k-1u} & for\ k = L, \end{cases}$$

$$\sum\nolimits_{k=1}^{L-1} y_{ku} = 1 \qquad (5\text{-}8)$$

$$\forall u \in U\ k \in K$$

Based on Equations (5-7) and (5-8), we can rewrite Equation (5-3) into a linearised equation as follows:

$$\delta_u^{AMP}\gamma_u + \sum_{t\in T}\sum_{n\in N} R_{tnu}\Phi_{tnu} + \delta_u^{AL}\gamma_u = \sum_{k\in K}(a_k)^2\, t_{ku} \qquad (5\text{-}9)$$

$$\forall u \in U$$

Based on Equation (4-5), the SNR of uplink when the user is at location u is given as:

$$\theta_u = \frac{(\sum_{t\in T}\sum_{n\in N} S_{tn}P_{tnu}\frac{1}{M})^2}{\xi^{AMP} + \xi^{AL} + \sum_{t\in T}\sum_{n\in N} E_{tnu}S_{tn}}\,,\ \forall u \in U \qquad (5\text{-}10)$$

where the numerator of the right term of Equation (5-10) represents the power of the sum of received optical current from different relay terminals. Equation (5-10) can be rewritten as:

$$\delta_s^{AMP}\theta_u + \delta_s^{AL}\theta_u + \sum_{t\in T}\sum_{n\in N} E_{tnu}\tau_{tnu} = (\sum_{t\in T}\sum_{n\in N} P_{tnu}S_{tn}\frac{1}{M})^2,\ \forall u \in U, \qquad (5\text{-}11)$$

where the non-negative linearisation variable τ_{tnu} is used to replace $S_{tn}\theta_u$. The relationship between them is as the follows [117]:

$$\begin{gathered}\tau_{tnu} \le \beta S_{tn} \\ \tau_{tnu} \le \theta_u \\ \tau_{tnu} \ge \beta S_{tn} + \theta_u - \beta \\ \forall n \in N, \forall u \in U, \forall t \in T\end{gathered} \qquad (5\text{-}12)$$

As the downlink, the quadratic term of uplink is linearised by the following equations:

$$\begin{gathered}(\sum_{t\in T}\sum_{n\in N} P_{nu}S_{tn}\frac{1}{M})^2 \approx \sum_{k\in K}(a_k)^2\, v_{ku} \\ \sum_{t\in T}\sum_{n\in N} P_{tnu}S_{tn}\frac{1}{M} = \sum_{k\in K} a_k v_{ku} \\ \sum_{k\in K} v_{ku} = 1\ \forall u \in U\end{gathered} \qquad (5\text{-}13)$$

As t_{ku}, v_{ku} is restricted by the following equations:

$$\begin{gathered}v_{ku}\begin{cases}\le z_{ku}\ for\ k = 1 \\ \le z_{k-1,u} + z_{bu}\ for\ k = 2,3,\cdots L-1, \\ \le z_{k-1u} for\ k = L\end{cases} \\ \sum_{k=1}^{L-1} z_{ku} = 1 \\ k \in K\end{gathered} \qquad (5\text{-}14)$$

We can rewrite Equation (5-11) as follows:

$$\delta_s^{AMP}\theta_u + \sum_{t\in T}\sum_{n\in N} E_{tnu}\tau_{tnu} + \delta_s^{AL}\theta_u = \sum_{k\in K}(a_k)^2\, v_{ku} \qquad \forall u \in U \tag{5-15}$$

To prevent error propagation and to guarantee QoS as explained in Chapter 4, the SNR of at user locations and the DF relay terminals should at least meet the threshold $Q = 15.6\ dB$ for $P_e \leq 10^{-9}$. The SNR for the user at location u should satisfy the following constraints:

$$\gamma_u \geq Q \quad , \quad \theta_u \geq Q\,, \qquad \forall u \in U \tag{5-16}$$

For DF relay terminals, the SNR of downlink and uplink at the relay terminals is precalculated by the ray tracing algorithm. If it is less than Q, then these locations will not be considered, thus for DF:

$$\begin{aligned} &if\ X_{nu} < Q\ ,\ I_{tnu} = 0 \ \ \forall n \in N, \forall u \in U, t = DF, \\ &if\ Y_{nu} < Q,\ P_{tnu} = 0 \ \ \forall n \in N, \forall u \in U, t = DF. \end{aligned} \tag{5-17}$$

To investigate the influence of the number of active relay terminals on the SNR of the system, S_{tn} is restricted as the following:

$$\sum_{n\in N}\sum_{t\in T} S_{tn} = M \tag{5-18}$$

Since only one kind of relay terminals can be deployed at a candidate location, S_{tn} is restricted by the following Equation:

$$\sum_{t\in T} S_{tn} \leq 1,\ \forall n \in N \tag{5-19}$$

5.3 The optimisation results of ORTA

To investigate the performance of ORTA, we considered three different scenarios of the AP location as illustrated in Fig 5-2.

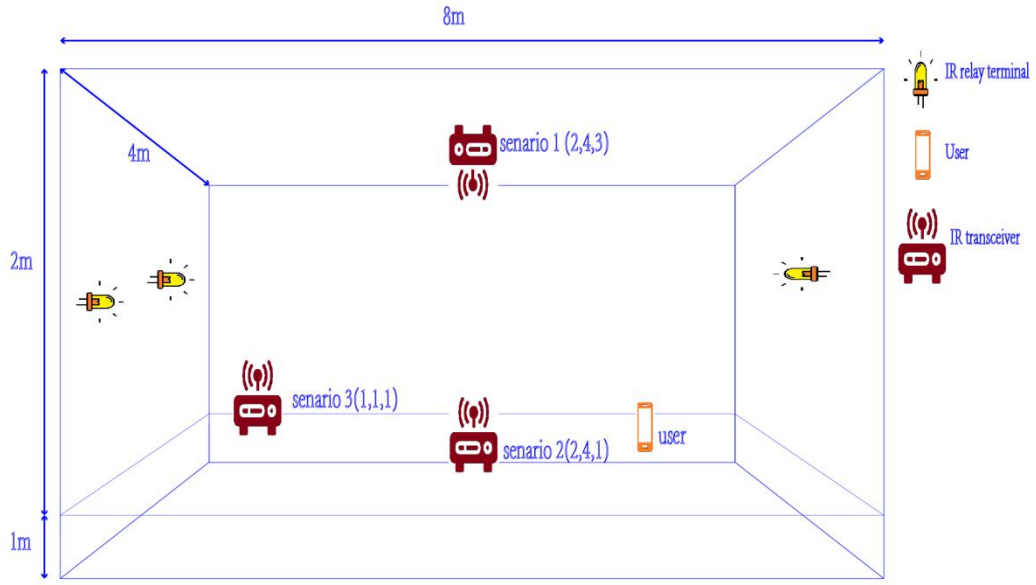

Figure 5- 2 Room set-up for ORTA optimisation.

5.3.1 Scenario 1

In scenario 1, the AP is mounted at the centre of the ceiling. The sum rate of the downlink and uplink SNR for all user locations for ORTA (the objective of ORTA) under scenario 1 for up to $M = 12$ relay terminals are given in Fig. 5-3. The best overall results are achievable by deploying 2 relay terminals, i.e., $M = 2$. As can be seen in Fig. 5-3 for $M = 3$, the objective of ORTA decreased due to the asymmetrical locations of relay terminals. The distances between relay terminals and test points are uniform due to locating relay terminals at the middle of the walls. We use the SNR sum of the system with no relay terminals deployed given in Chapter 4 as a reference.

The downlink and uplink SNR of the 21 user locations with ORTA for $M = 2$, $M = 4$, $M = 6$ and no relay terminals are shown in Fig. 5-4. As shown in Fig. 5-4, for the systems with relay terminals, the fluctuation of the uplink plus downlink SNR at different test points are smoother than the system without relay terminals. This is due to the signals received from optimally selected relay terminals. Also, the results in Fig 5-4(b) show that through deploying relay terminals, the SNR of uplink at the test points at the corner of the room is improved. Since the signal from the AP can directly arrive at the user's receiver without reflections, the SNR results of the system without relay

terminals are better than the systems with relay terminals for user locations toward the centre of the room.

Fig. 5-5 gives the optimal locations and types of the relay terminals for $M = 2, 4\ and\ 6$ in scenario 1. The red points represent the optimal location of relay terminals in the room. All the relay terminals are optimally selected to be DF relay terminals. Note that the optimisation of the relay terminal type with the ORTA objective will always result in selecting the DF terminal as it gives the best SNR. This result verifies the results in Chapter 4 where the DF relay terminal has better SNR compared with OEO and SOA relay terminal in different scenarios. Considering cost or power consumption in objective functions can result in the selection of other types of relay terminals. The relay terminals are optimally deployed symmetrically on two opposite walls. Relay terminals form a line at the middle of two opposite walls.

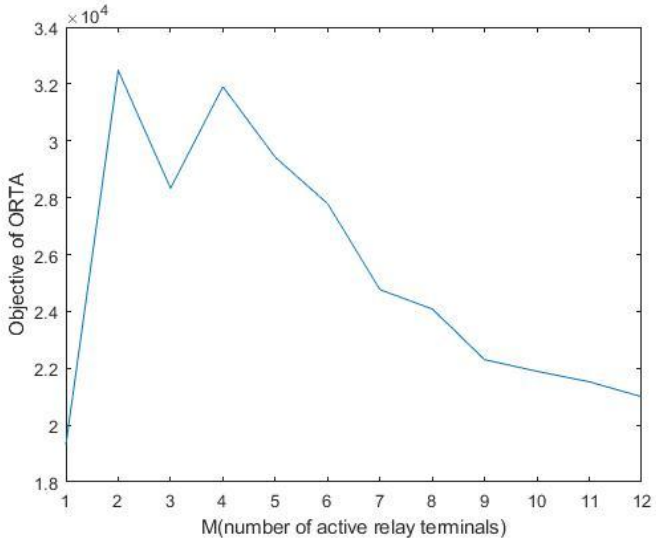

Figure 5-3 The sum of uplink and downlink snr for all user locations (objective of ORTA) for scenario 1.

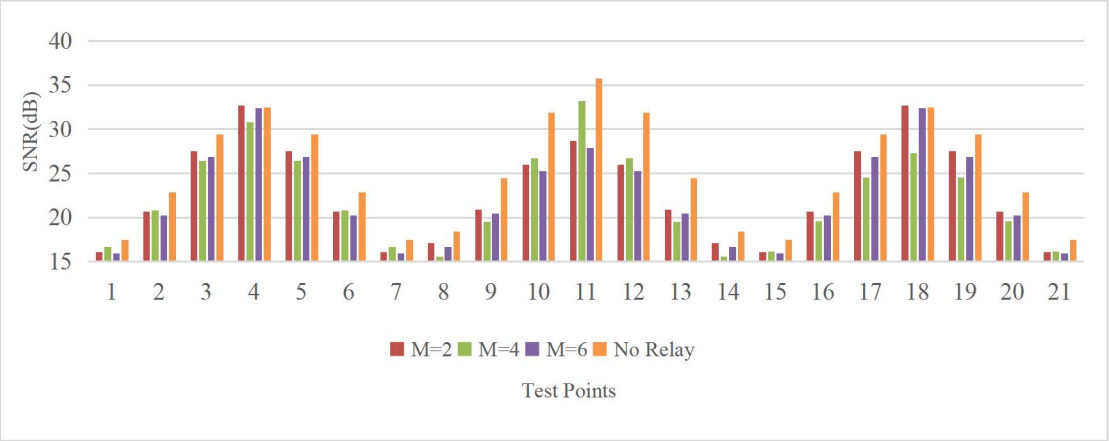

(a) Downlink

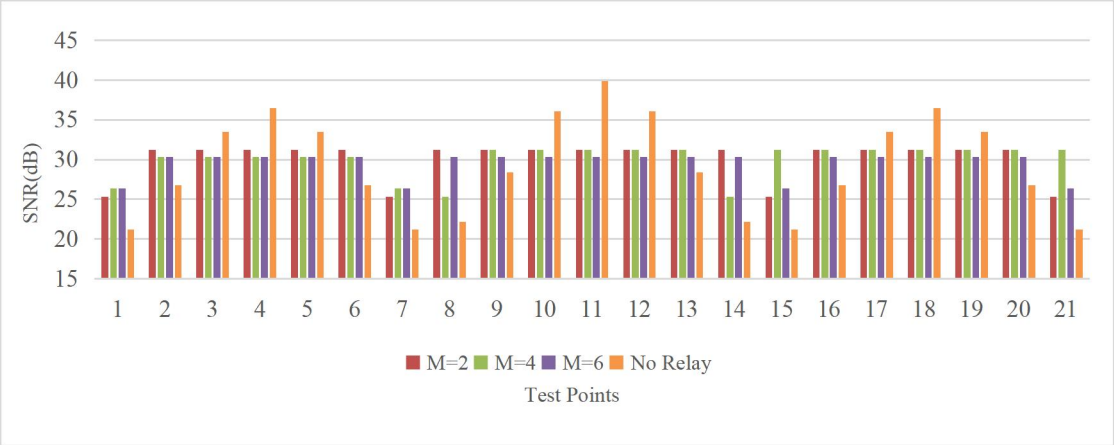

(b) Uplink

Figure 5-4 SNR of downlink and uplink of each test points with different numbers of relay terminals in scenario 1.

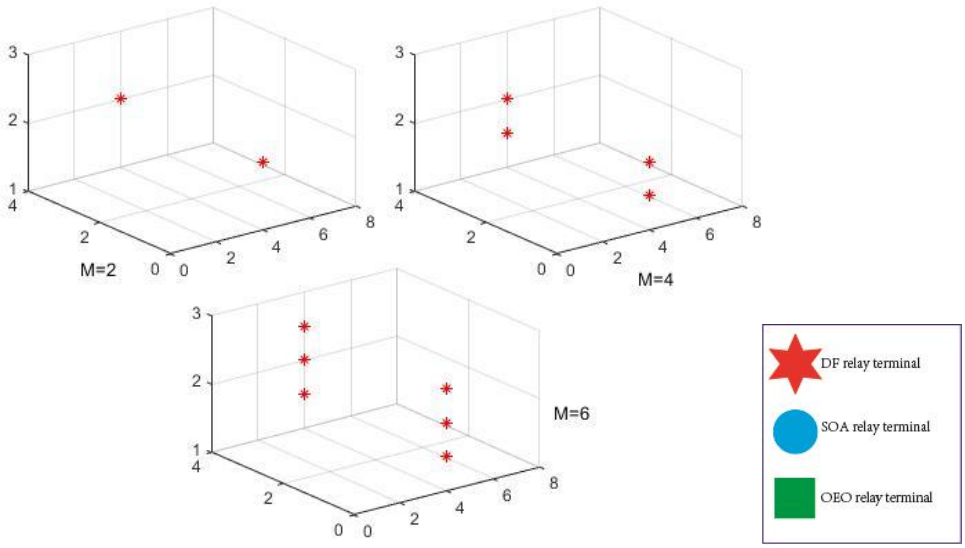

Figure 5- 5 The locations and types of relay terminals in scenario 1.

Fig. 5-6 shows the variation in the uplink and downlink SNR for the different user locations. The red line represents the mean value of the SNR considering the 21 user locations, the blue rectangle represents 25th percentile and the 75th percentile values (i.e., the lower side and the upper side, respectively), the black vertical dashes show the upper and lower value, and the plus sign represents outlier SNR values.

We also compare the results of ORTA under scenario 1 with the 3 deployment schemes discussed in Chapter 4 as shown in Fig. 5-7 and 5-8. We compare the situation where 6 relay terminals are deployed in the room with ORTA to two cases of fixed relay terminal deployment case where the 6 relay terminals are deployed on the walls 0.5m and 1.5m below the ceiling. The distance between the relay terminals is 4m. The downlink performance of ORTA is on average better by 0.4% and 9% than fixed deployment at 0.5m and 1.5m below the ceiling, respectively. The sum of downlink SNR results of ORTA is greater than the previous two schemes. As shown in Fig. 5-7 (a), test points 4 and 18 contribute a major part of the sum of downlink SNR. An extra constraint can be used to limit the upper bound of SNR at any test points to balance the SNR among the different test points. On the contrary, the uplink performance of ORTA is better by 54%, and 70% than fixed deployment at 0.5m and 1.5m below the ceiling, respectively, as can be seen in Fig. 5-7 (b) and Fig. 5-8. We choose the sum of uplink

and downlink with similar importance, however the results show that ORTA focuses on maximising the uplink SNR to maximise total SNR instead of balancing the value of uplink and downlink.

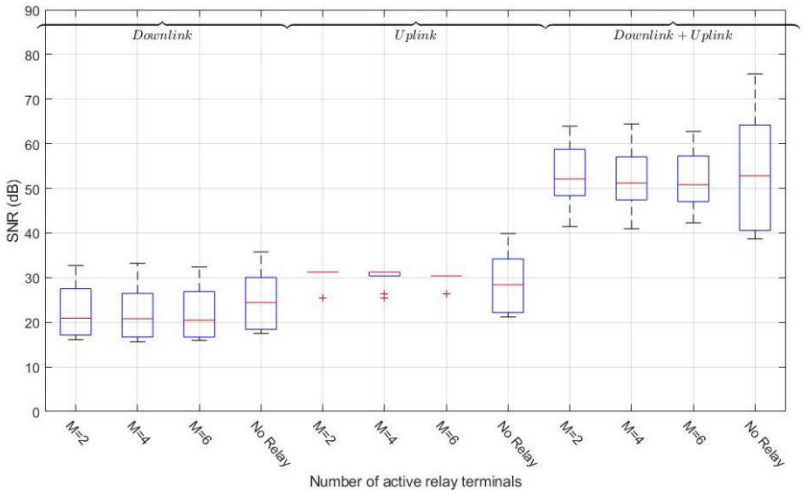

Figure 5- 6 SNR of downlink and uplink of each test points with different numbers of relay terminals in scenario 1.

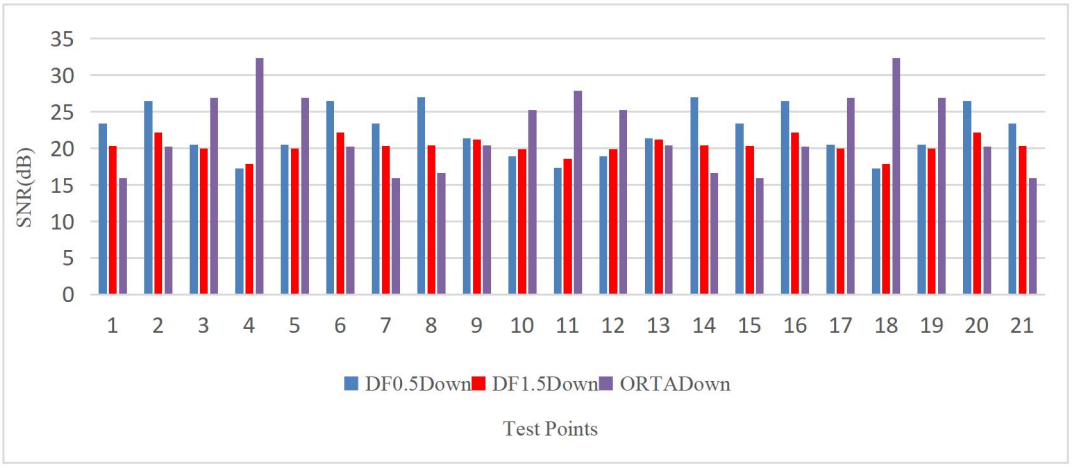

(a) Downlink

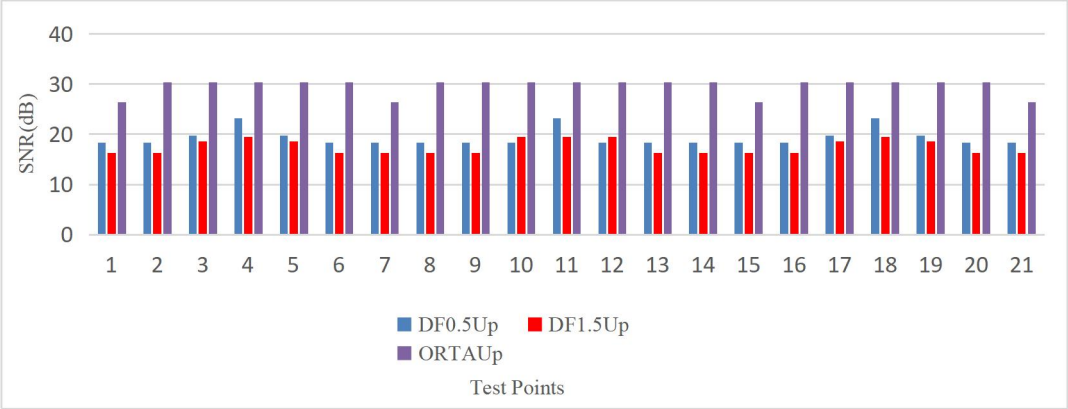

(b) Uplink

Figure 5- 7 SNR of downlink and uplink of ORTA compared to previous schemes.

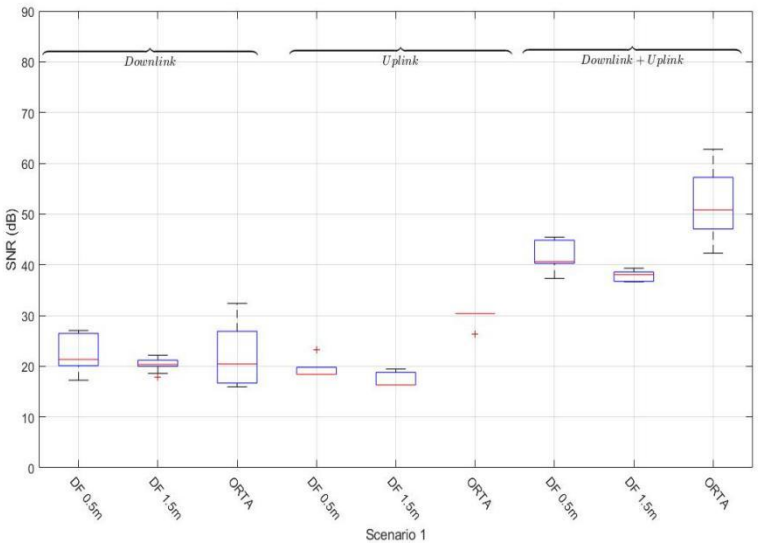

Figure 5- 8 The summary result of downlink and uplink of ORTA compared to previous schemes in scenario 1 with 6 relays.

5.3.2 Scenario 2

In scenario 2, the AP is in the centre of the communication floor. The results for the sum SNR of uplink and downlink considering the 21 user locations are shown in Fig. 5-9 versus up to $M = 12$ relay terminals. The maximum value of the sum of downlink and uplink SNR (i.e., ORTA objective is achieved when one relay terminal is deployed.

Let us focus on the cases when $M = 1,2,4$, and 6 as shown in Fig. 5-10 and Fig. 5-11. For $M = 4\ and\ 6$, the SNR of downlink transmission for test points at the edge of the room is higher compared to the case of $M = 1$. However, the sum of SNR when $M = 1$ is higher compared to the other values of M.

Fig. 5-12 shows the optimal locations and types of relay terminals for $M = 1, 2, 4$ and 6. The DF relay terminal is selected as it has better performance compared to SOA and OEO relay terminals. Note that, for $M = 1$, the relay terminal at the centre of ceiling is selected and for $M > 1$ the relay terminal at the centre of ceiling and other candidate relay terminals around it on the ceiling are selected to enhance the SNR of the system. When the number of relay terminals exceeds 6, the SNR of uplink and downlink decreases significantly regardless of the user location. This shows that the low channel gain of the user degrades the SNR in relay-based wireless communication systems.

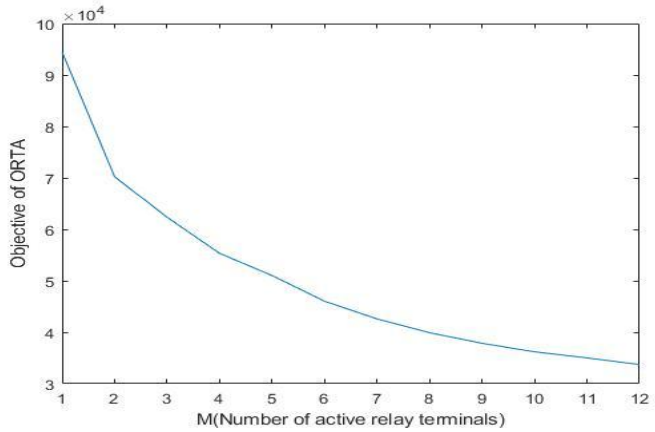

Figure 5- 9 The objective of ORTA for all user locations considered in scenario 2.

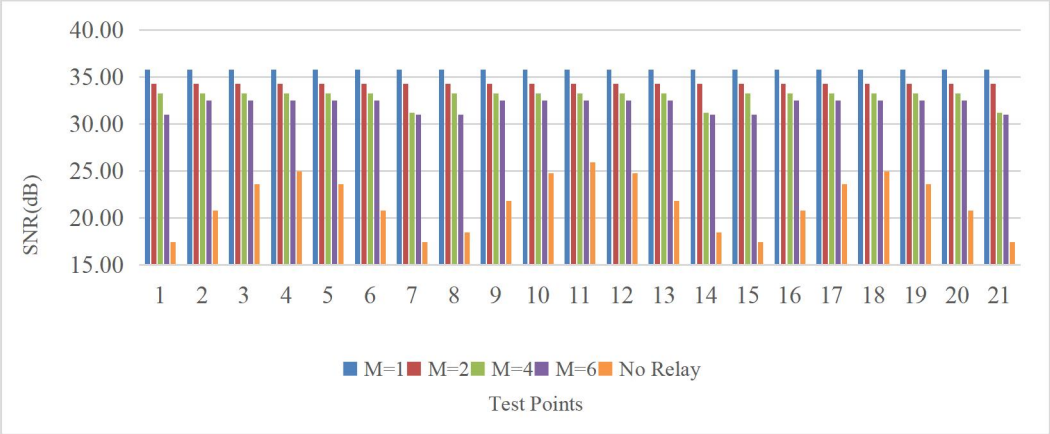

(a) Downlink

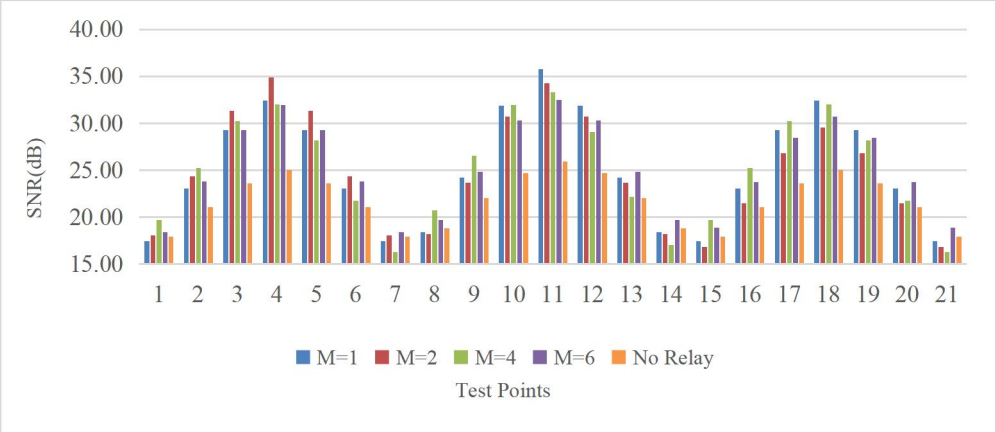

(b) Uplink

Figure 5-10 SNR of downlink and uplink of each test point with different numbers of relay terminals in scenario 2.

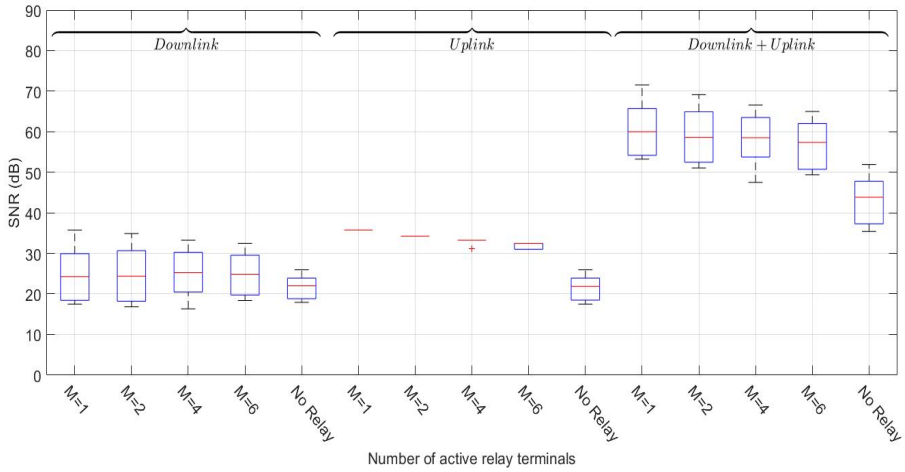

Figure 5- 11 The summary results of downlink and uplink of each test point with different numbers of relay terminals in scenario 2.

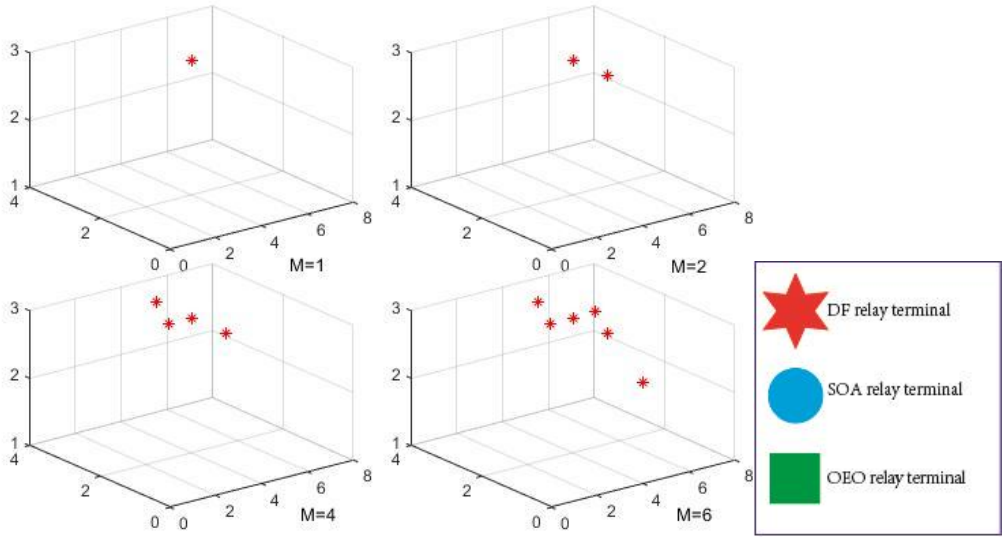

Figure 5- 12 The locations and types of relay terminals in scenario 2.

In Figs. 5-13 and 5-14, the performance of ORTA with 6 relay terminals is compared with the two fixed deployment schemes where the DF relay terminals are mounted 0.5 m below the ceiling and 1.5 m below the ceiling. The results show that the downlink SNR of ORTA is 19% and 9% better than the fixed deployment at 0.5m and 1.5m below the ceiling, respectively while the uplink SNR of ORTA is 127% and 86% better than the fixed deployment at 0.5m and 1.5m below the ceiling, respectively.

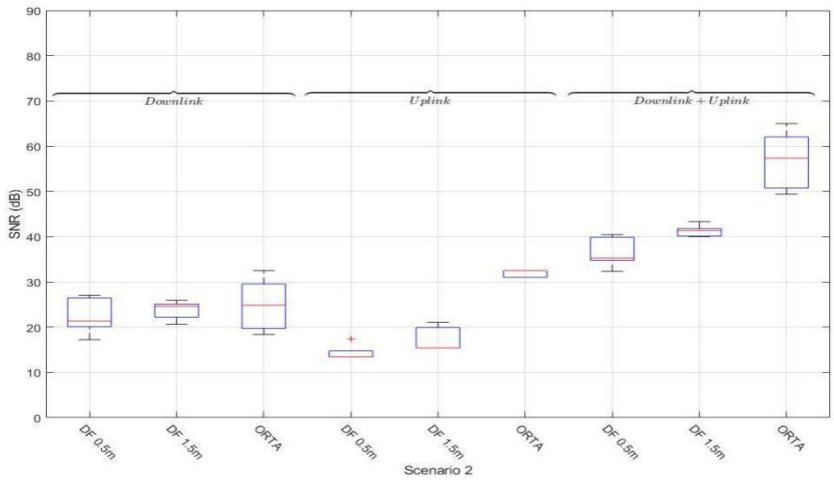

Figure 5- 13 The summary results of downlink and uplink of ORTA compared to previous schemes in scenario 2 with 6 relays.

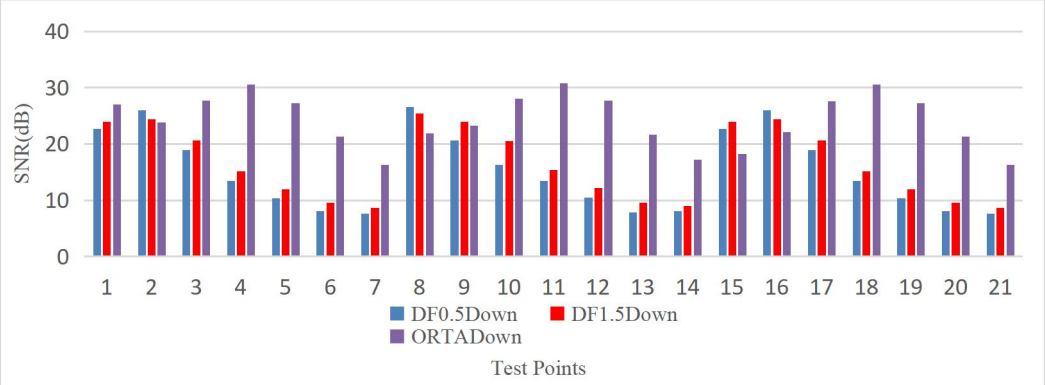

(a) Downlink

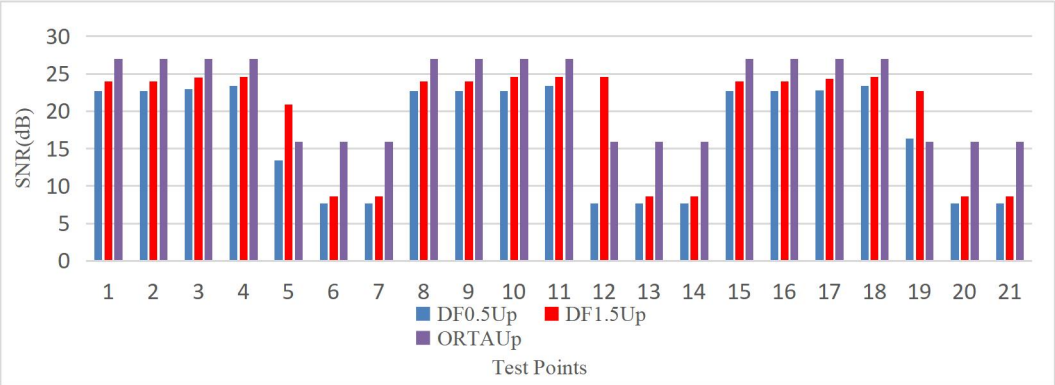

(b) Uplink

Figure 5- 14 SNR of downlink and uplink of ORTA compared to previous schemes in scenario 2 with 6 relays.

5.3.3 Scenario 3

For an extreme situation, the optical AP in this scenario is located at the corner of the communication plane, specifically at (1 m, 1 m, 1 m). The ORTA objective (sum of downlink and uplink SNR) are presented in Fig. 5-15 versus the number of relay terminals. The optimal number of relay terminals in this scenario is 4. Note that, the number of relay terminals is limited to 7 due to the constraint in Equation (5-17), i.e., the condition of only accepting SNR values that are equal to or higher than 15.6dB. Furthermore, the downlink and uplink SNR values for all test points with 1, 2, 4 and 6 terminals are shown in Fig. 5-16 and Fig. 5-17. Deploying the optical AP at the corner of the room without relay terminals results in low SNR. Note that, the sum SNR of downlink and uplink increases once the relay terminals are deployed according to the optimal locations given in Fig. 5-18.

To conclude, the optimum number of relay terminals depends on the location of the optical AP and the best results in the three scenarios are obtained when a fewer number of relay terminals are used as this results in signals that can be constructively combined giving relatively high received power.

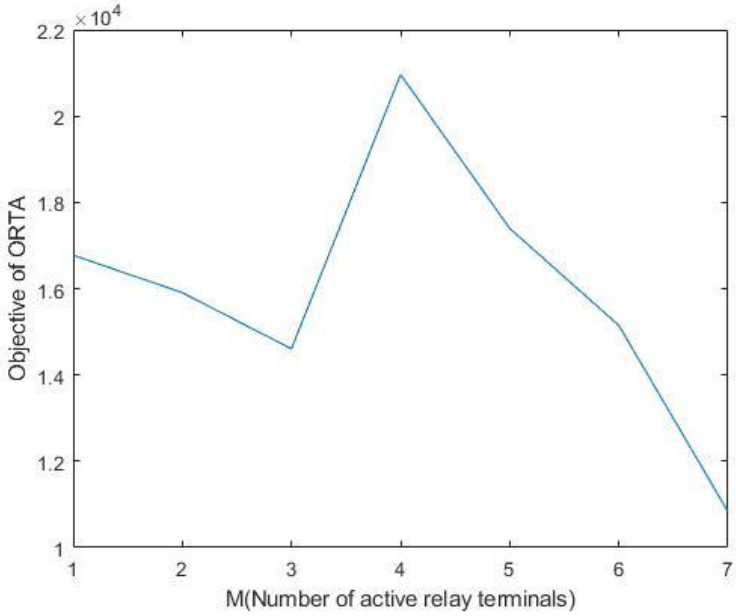

Figure 5- 15 The objective of ORTA which is the sum of SNR for all user locations involved uplink and downlink in scenario 3.

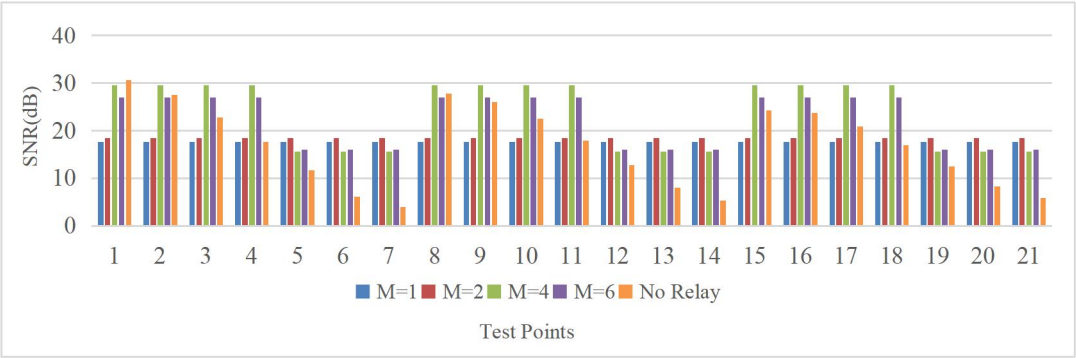

(a) Downlink

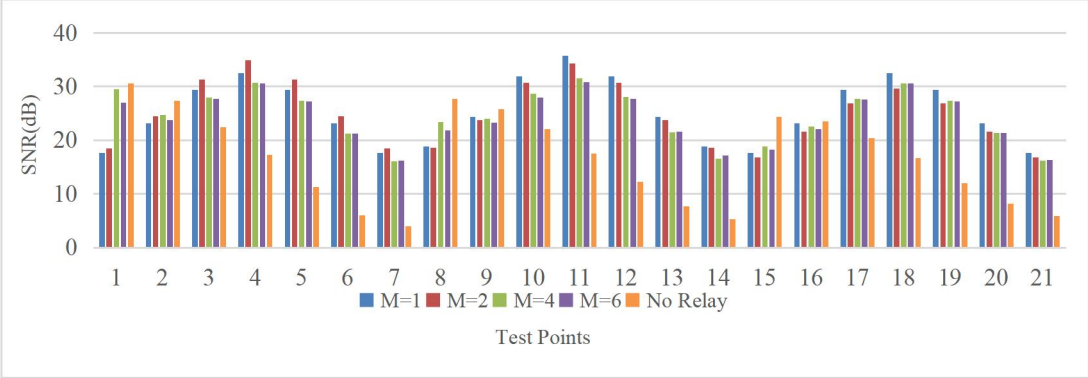

(b) Uplink

Figure 5-16 SNR of downlink and uplink of each test points with different numbers of relay terminals in scenario 3.

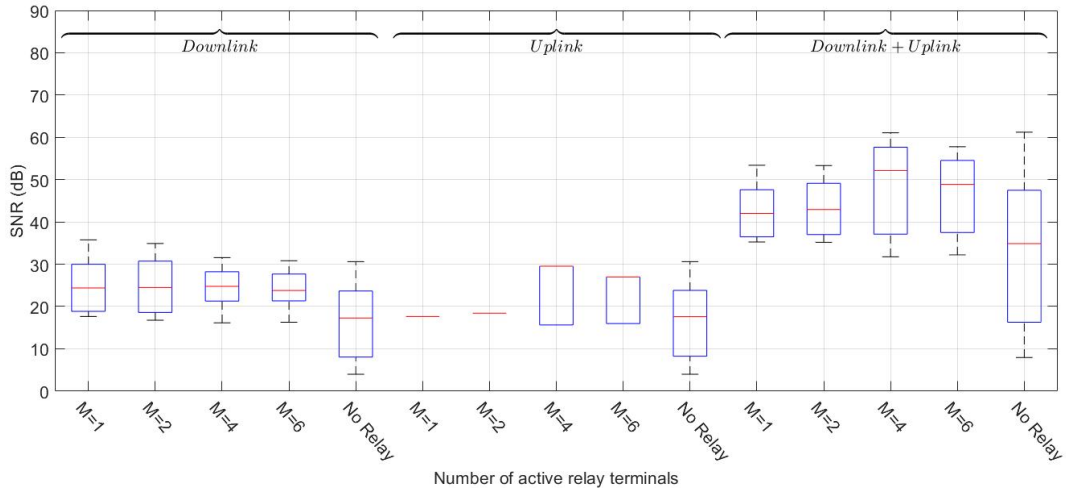

Figure 5- 17 The summary results of downlink and uplink of each test points with different numbers of relay terminals in scenario 3.

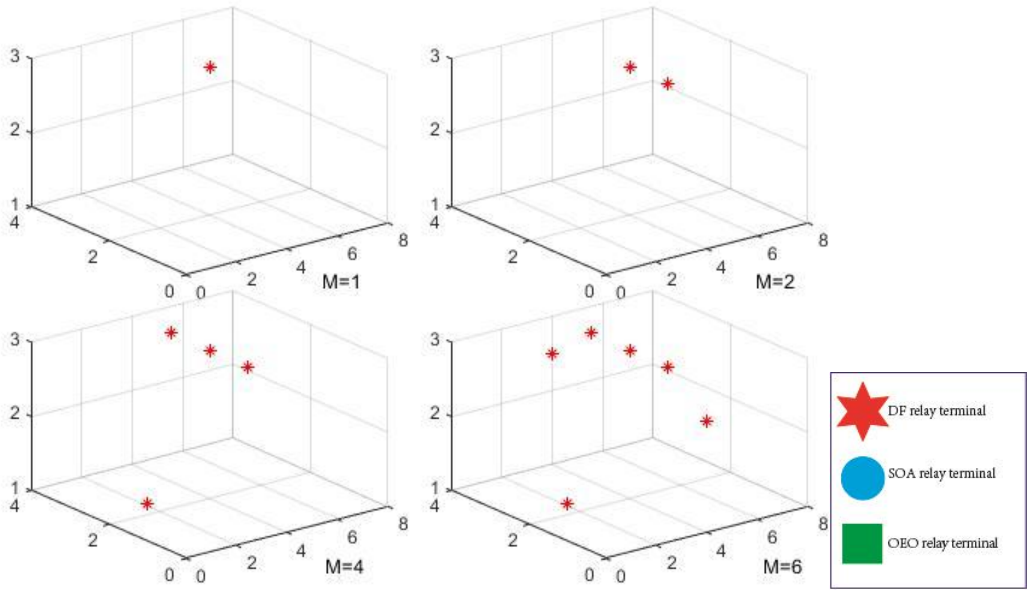

Figure 5- 18 The optimal locations and types of relay terminals in scenario 3.

5.3.4 ORTA with different numbers of uplink relays and downlink relays

In the previous optimisation, we considered that the uplink and downlink go through the same set of relay terminals. To further investigate the system, we considered a scenario where uplink and downlink transmissions are sent through different sets of relay terminals. The binary variable S_{tn} $(n \in N\ t, t \in T)$ is replaced by two new binary

variables X_{tn} and Z_{tn} ($n \in N\ t, t \in T$). X_{tn} is a binary variable that is equal to 1 if the downlink transmission goes through a relay terminal at candidate location $n, n \in N,$ of type $t,\ t\ \in T.$ Z_{tn} is a binary variable that is equal to 1 if the uplink transmission goes through a relay terminal at candidate location $n, n \in N,$ of type $t, t\ \in T.$ In this context, Equation (5-18) is replaced by:

$$\sum_{n \in N} X_{tn} = Q\ ,\ \sum_{n \in N} Z_{tn} = H, \tag{5-20}$$

where Q and H are the number of active relay terminals for downlink and uplink, respectively. Constraints (5-3) and (5-10) which relate to the SNRs of downlink and uplink, are replaced by:

$$\gamma_u = \frac{\left(\sum_{t \in T} \sum_{n \in N} I_{tnu} X_{tn} \frac{1}{M}\right)^2}{\delta_u^{AMP} + \delta_n^{AL} + \sum_{t \in T} \sum_{n \in N} R_{tnu} X_{tn}}, \forall u \in U \tag{5-21}$$

$$\theta_u = \frac{(\sum_{t \in T} \sum_{n \in N} P_{tnu} Z_{tn} \frac{1}{M})^2}{\xi^{AMP} + \xi^{AL} + \sum_{t \in T} \sum_{n \in N} E_{tnu} Z_{tn}}, \forall u \in U \tag{5-22}$$

respectively, the processes of piece-wise-linearisation of Equations (5-21) and (5-22) is the same as the method described for the linearisation of Equations (5-8) -(5-15) and thus, the details of the linearisation of Equations (5-21) and (5-22) are not given here. We evaluate the objective of ORTA while varying the values of Q and H. The sum SNR is shown in Fig. 5-19, where H is the number of active relay terminals for uplink, and Q is the number of active relay terminals for downlink. For 1 downlink relay terminal and 3 uplink relay terminals are active, the sum SNR of uplink and downlink reached the maximum value. In Fig. 5-20 (a), (b), and (c), the results show that the sum SNR of downlink and uplink when the uplink and downlink are allowed to be relayed through different number of relay terminals are better by 3% and 5% compared to the case where the downlink and uplink go through the same number of relay terminals. The sum SNR is obtained with $H = 1$, Q=3.

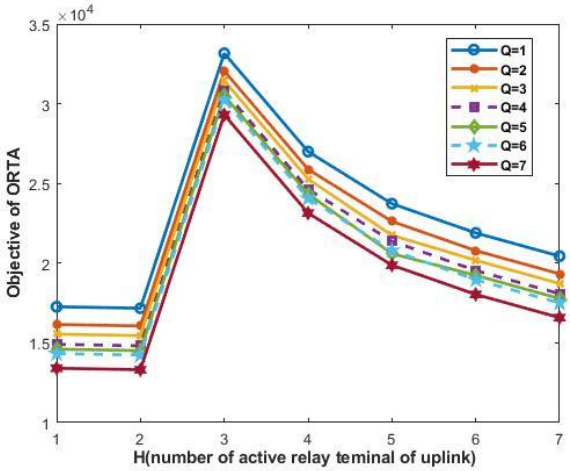

Figure 5-19 The objective of ORTA in scenario 3 that uplink and downlink go through different group of relay terminals.

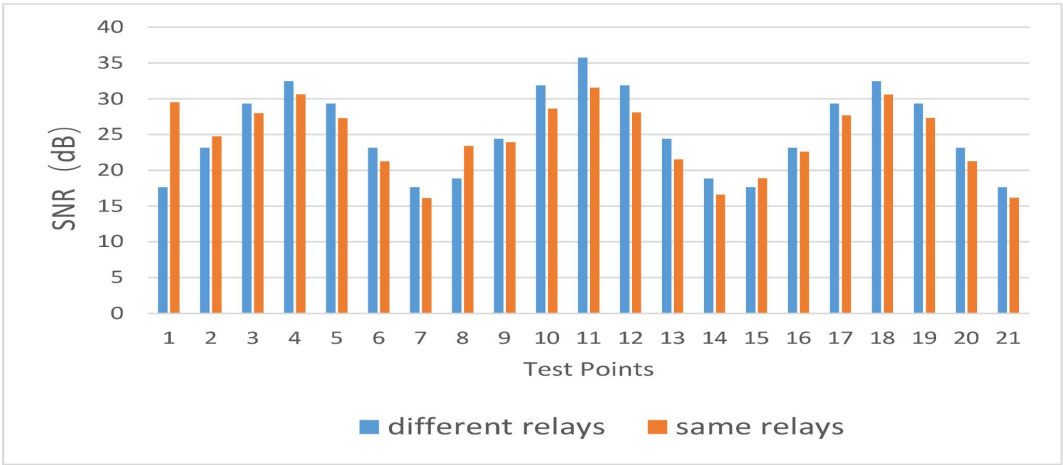

(a) Downlink

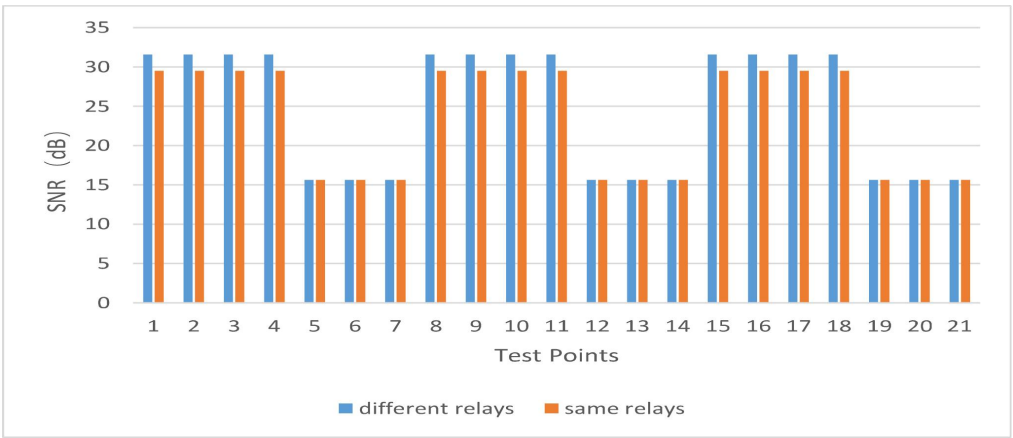

(b) Uplink

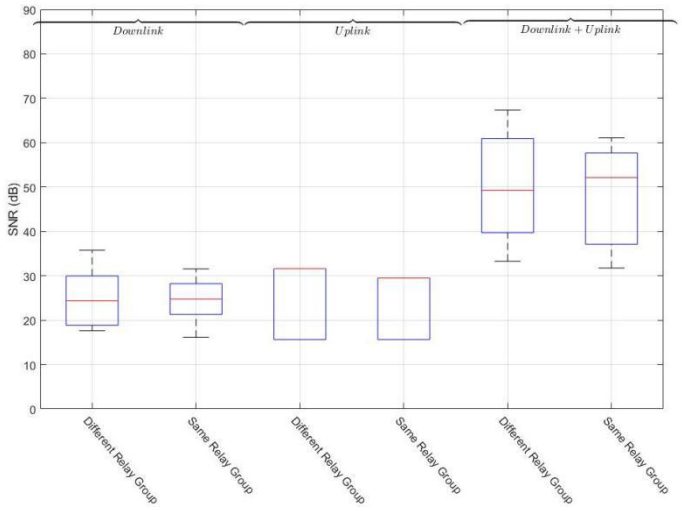

(c) Summary of results

Figure 5- 20 SNR of the system where uplink and downlink go through different relay terminals versus uplink and downlink go through same relay terminals in scenario 3 when the total number of relay terminals is equal to 4.

The optimal locations of the relay terminals are shown in Fig. 5-21. The relay terminal for downlink is deployed at the centre of the ceiling while the relay terminals for uplink are distributed on two walls and the ceiling to ensure coverage in the corner of the room.

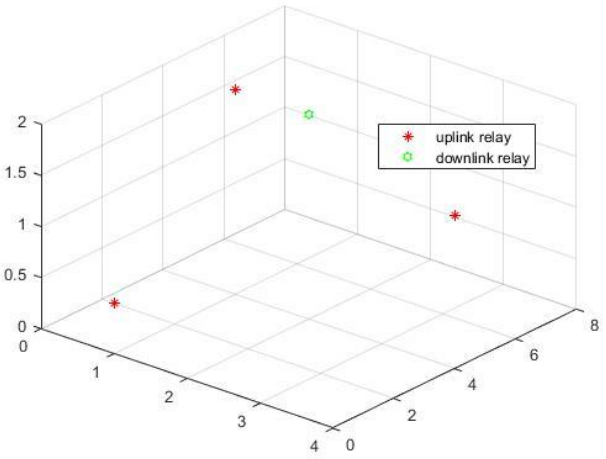

Figure 5- 21 The locations of relay terminals for uplink and downlink (All are DF relay terminals).

5.4 Summary

In this chapter, ORTA is introduced to optimise the location and type of relay terminals (i.e., the deployment scheme) considering different numbers of relay terminals. The sum SNR of uplink and downlink for ORTA are evaluated considering different locations of the optical AP and compared with the fixed deployments of relay terminal in Chapter 4.

For the first scenario the optical AP is located at the centre of the ceiling. The best performance of ORTA is obtained with 2 relay terminals resulting in 19% and 9% improvement in downlink SNR and 127% and 86% improvement in uplink SNR compared to fixed deployments of relay terminals at 0.5m and 1.5m below the ceiling, respectively.

For the second scenario where the optical AP is in the middle of the communication floor at the same level as the user, the results show that the best sum SNR uplink of ORTA using DF relay terminal is 54%, and 70% better than the fixed deployment of relay terminals at 0.5m, and 1.5m below the ceiling, respectively.

For the third scenario where the optical AP is placed on the communication floor at the corner of the room, the best performance of ORTA is achieved when 4 relay terminals are active. By adjusting the variables and constraints of ORTA to deploy different number of relay terminals for downlink and uplink, the results show that the sum SNR is 3% and 5% for downlink and uplink, respectively better compared to the case where the downlink and uplink go through same relay terminals.

Chapter 6: Multiuser Beam Steering OWC system based on NOMA

6.1 Introduction

To enhance the achievable throughput in multiuser downlink of OWC systems, several multiple access schemes were proposed, including Carrier Sense Multiple Access (CSMA) [120], Orthogonal Frequency Division Multiple Access (OFDMA), Code Division Multiple Access (CDMA), Time Division Multiple Access (TDMA) [121], and Non-Orthogonal Multiple Access (NOMA). Among these, NOMA and its spectral efficiency and user fairness have attracted extensive research [122].

NOMA was proposed in [123] as a spectrum-efficient multiple access scheme for downlink in VLC systems. The signals of different users in NOMA systems are superimposed in the power domain with different power levels. The power levels are associated with users according to their channel conditions. Based on this, a user can share frequency and time resources leading to increased spectral efficiency. NOMA allocates higher power levels to users with worse channel conditions than those with good channel conditions to balance the influence of the channels on different users. As a result, the user with the highest allocated power can directly decode its signal while treating the signals of other users as noise. The rest of users in the system perform Successive Interference Cancellation (SIC) for the multi-signal separation for lower decoding orders prior to decoding its signal while treating the signal of high decoding orders as noise. Therefore, accurate channel state information (CSI) and successive SIC are two important processes for NOMA deployment [122].

In [123], assuming precise CSI, a Gain Ratio Power Allocation (GRPA) scheme was proposed which dynamically adjusts the power allocation factor related to CSI between different users. Compared with NOMA with fixed power allocation factor, the achievable rate and BER results show that NOMA has better performance when the GRPA scheme is deployed. However, precise CSI is hard to acquire. A noisy CSI

model is introduced in [124] while an outdated CSI model is reported in [122]. Outdated CSI errors may result from the variations in the channel realisations due to the mobility of users and/or shadowing effects that occur after the latest channel estimate update. These two imperfect CSI channel models, i.e., noisy CSI and outdated CSI models, are extensively investigated as they are considered to be closer to the actual channel state. Motived by this, different techniques are proposed to improve the imperfect CSI as well as the SIC. In [125], random linear network coding is applied to enhance the success probability of NOMA-based transmission while the two Constellation Coding variants were adopted in [126], [127] to cancel the influence of imperfect SIC. The results show that the extra coding scheme reduced the bit error rate (BER) of NOMA-based OWC system while increasing the complexity of the transceiver. In [128], the power allocation of different users is converted into a Convex Semidefinite Program (SDP) with the objective to minimise the BER of all users. Similarly, the authors in [129] proposed a user pairing and power allocation scheme based on letter leveraging Fractional Transmit Power Allocation (FTPA) and Improved Power-Law Strategy (IPLS) methodologies. The studies in [130] and [131] focused on constructing a dynamic power allocation scheme. However, the power allocation algorithms in [130], [131] are highly complex. In [132], [133] a Convolutional Neural Network (CNN) based signal demodulator that mitigates both linear and nonlinear distortions in NOMA-OWC was proposed.

For NOMA-based OWC systems, currently most of the research focuses on the diffuse transmitters which are modelled as typical Lambertian diffuse beam [124-131]. While diffuse transmitters can provide effective ubiquitous connectivity in an indoor environment, they suffer, as explained in Chapter 2, from inter-symbol interference due to signal reflected by the walls, ceiling, floor, and other furniture in the room and low SNR due to the free space propagation loss and signal spread. Beam steering was proposed in recent studies to solve the drawbacks of OWC as explained in Chapter 2. The transmitter of beam steering OWC provides a narrow beam steering that follows the mobile user. The narrow beam size reduces free space propagation loss and the ISI due to the reflection from walls and ceiling. LDs, which possesses high modulation bandwidth, can be efficiently integrated in beam steering OWC systems as the light source. The authors in [34] used beam steering to achieve a data rate of up to 25 Gbps.

The beam steering technique of OWC can be generally divided into two groups. The first group is the mechanical beam steering (i.e., piezoelectric actuators-controlled lens), and the second group is non-mechanical beam steering (i.e., SLM and Micro Electromechanical Systems (MEMS) controlled mirrors). Compared with mechanical beam steering, non-mechanical beam steering consumes less power, have faster reaction speed, possess a smaller size, and does not suffer from mechanical wear and failure [134]. Non-mechanical beam steering is the mainstream solution for the beam steering OWC at present [134]-[137].

Beam steering technology for OWC transmitter based on SLM mounted with a phase Fresnel zone plate is widely discussed in [77], [134]. Compared with a diffuse transmitter, beam steering transmitter suffers less from inter-symbol interference due to narrow light beam which provides high SNR [132]. Meanwhile, via mounting multiple phase Fresnel zone plates on SLM [88], [120], the optical signal that passes through SLM can be divided into multiple narrow light beams to different targets. Based on multiple targets beam steering technology, a NOMA-based OWC with beam steering transmitter for downlink is proposed in this work for the first time to the best of our knowledge. Beam steering is thus investigated in this chapter as an alternative to the use of relays and potentially as a complementary technology.

In this chapter, we introduce beam steering in a NOMA-based OWC system and investigate the influence of the number of users and a static power allocation scheme on the performance of the system. Our results show that with a power allocation factor equals of 0.4 and 6 users, a BER of 1.7×10^{-4} and average bit rate of 3.6×10^{11} b/s can be achieved. The narrow divergence angle of the AP light beam in beam steering OWC systems causes blockage by humans resulting in communication outage. In this chapter we also introduce a relay cooperative OWC system to reduce outage probability in beam steering NOMA based OWC systems.

The rest of this chapter is organised as follows: Section 6.2 describes the beam steering configuration and NOMA based OWC system. Section 6.3 describes the room setup and presents the simulation results and related discussion. In Section 6.4, the relay

cooperative OWC system is introduced to reduce the shadowing and blockage due to humans moving in the room. Finally, this chapter is concluded in Section 6.5.

6.2 Beam steering configuration for a NOMA based OWC system

6.2.1 Beam steering setup for all APs

In this work, the beam steering configuration consists of a SLM rendered with a digital Fresnel Zone Plate (FZP) pattern and an Angle Magnifier (AM) which is a telescope configuration as shown in Fig. 6-1. A uniform, near-flat-field irradiance is produced by the light source to cross the SLM and the beam profile remains Gaussian over the full steering range of SLM with FZP [134].

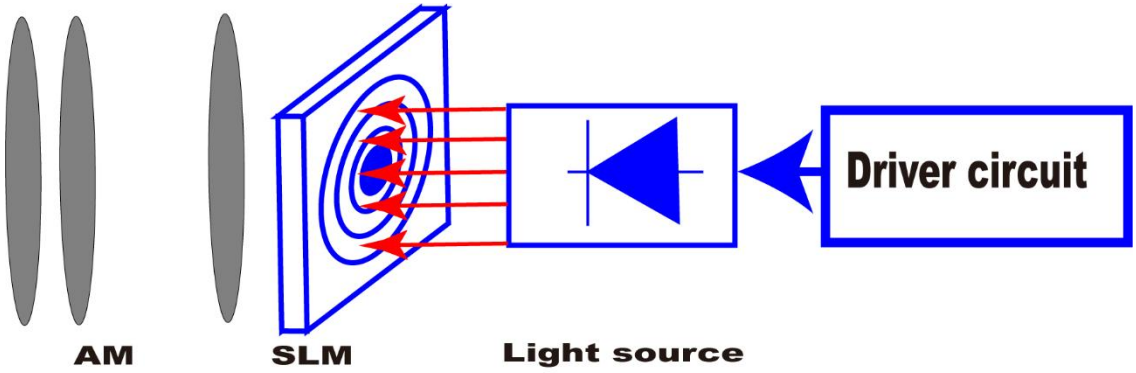

Figure 6- 1 The beam steering configuration of the transmitters (i.e., the APs).

Let $(x_0,\ y_o)$ represents the coordinates of FZP zone centre on SLM. The phase pattern of FZP is derived from a spherical wavefront whose field is given by [134]:

$$E(x,y) = \exp\left(-i\pi\frac{(x-x_0)^2+(y-y_0)^2}{\lambda f}\right) \tag{6-1}$$

where λ is the wavelength of the incident light, and f is the focal length of FZP. The phase calculated from the field is modulo 2π normalised to an 8-bit grey-scale level as shown in Fig. 6-2 where different grey level represents different phase pattern.

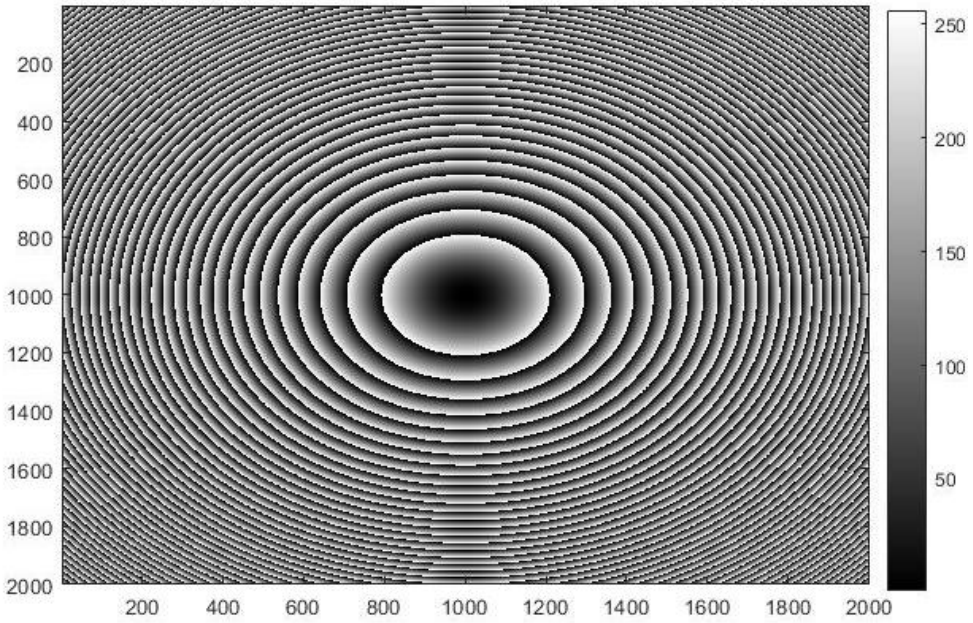

Figure 6- 2 FZP pattern with phase range from 0 to 2π (8 bit).

The maximum steering angle (θ_m) of the SLM with FZP is limited by the pixel size and the incident light wavelength. It is approximated by the first null in the Fraunhoffer diffraction pattern for a square aperture which is given as [134]:

$$\theta_m = sin^{-1}\left(\frac{\lambda}{\rho}\right), \tag{6-2}$$

where ρ is the pixel pitch of the SLM. In this work, we consider an SLM with $\rho = 8\mu m$ and infrared incident light with $\lambda = 850nm$. θ_m in this case is limited to $\sim 6^{\circ}$. The usable steering range is restricted because the intensity diffracted from a rectangular aperture falls off (in one dimension) with increasing angle according to [134], [139]:

$$I = I_0 sinc\left(\frac{\rho \sin(\phi)}{\lambda}\right)^2, \tag{6-3}$$

where I is the light power of zeroth order in far field, I_0 is the light power on the incident axis of the light source and ϕ is the beam steering angle. For a SLM with $\rho = 8\mu m$, infrared incident light with $\lambda = 850nm$, and light power I_0 of the incident light is normalised to 1, the light power I with increasing beam steering angle is shown in Fig. 6-3. The half power point is at $\sim 3^{\circ}$.

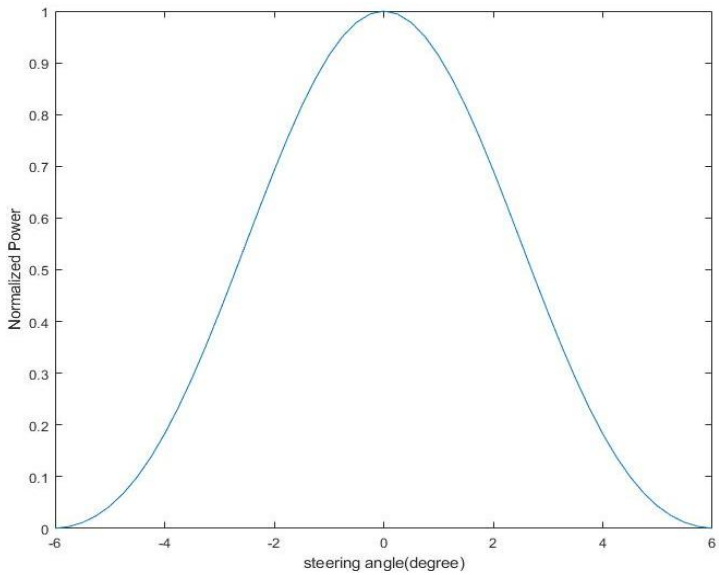

Figure 6- 3 The light power of SLM with varying the steering angle.

The limited beam steering range and power efficiency makes using only the SLM with FZP not adequate to achieve the actual requirement in a real environment. An extra AM is required as shown in Fig. 6-1 and Fig. 6-4 [134], [138]. AM is an afocal system which is constructed from three lenses. The magnification factor γ is defined as $\gamma = f_1/f_2$, where f_1 and f_2 are the focal lengths of lens 1 and 2, respectively. Let θ_{SLM} represents the steering angle of the incident light beam from the SLM, the steering angle θ_{AM} is defined as [138]:

$$\theta_{AM} = \gamma\theta_{SLM}, \tag{6-4}$$

Let γ=10, the maximum steering angle of SLM via an AM is $\theta_m^{'} = \gamma\theta_m \approx 60^{\circ}$. However, the non-negligible thicknesses and limited field of view (FOV) of the actual lens provides a quasi-linear angle magnification and an actual maximum steering angle lower than $\theta_m^{'}$ [138]. For the sake of simplicity, these two factors are ignored in the simulations in this chapter (the FOV of AM is set as 60°). The power of light beam via SLM and AM is impacted by the penetration factor of AM and SLM as well as the phase scale level of SLM. Therefore, Equation (6-3) is re-defined as [138], [140]:

$$I = I_0 sinc\left(\frac{\rho \sin(\phi)}{\lambda}\right)^2 sinc\left(\frac{1}{L}\right)^2 \rho_{SLM}\rho_{AM}, \tag{6-5}$$

where L is the phase scale level which is defined as 256 (8 bit) of SLM, ρ_{SLM} is the penetration factor of SLM and ρ_{AM} is the penetration factor of AM.

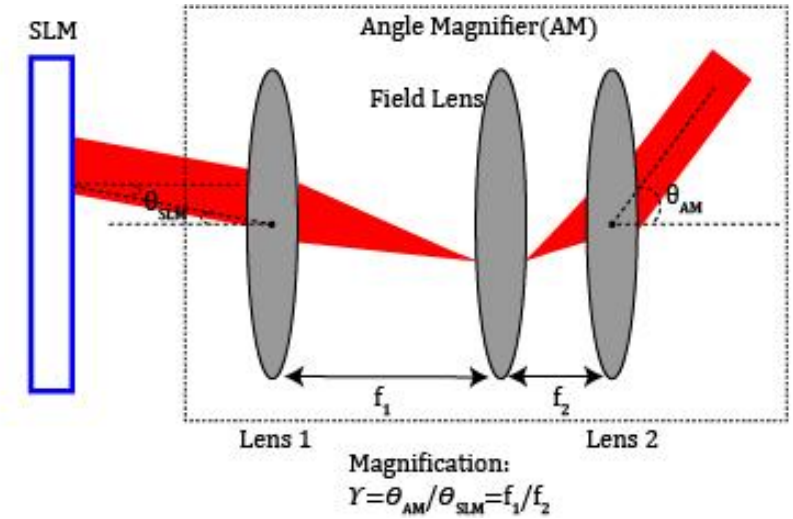

Figure 6- 4 AM system.

Via dividing the surface of SLM into several smaller areas, the beam steering system proposed can steer beams to multiple targets simultaneously. For each area, a unique Fresnel phase zone plate is generated for each user [122], [124]. The phase patterns of SLM with 2 or 4 targets are shown in Fig. 6-5(a) and (b), respectively.

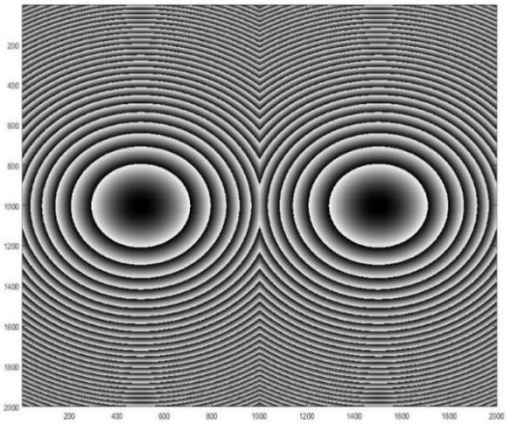

(a) Two targets.

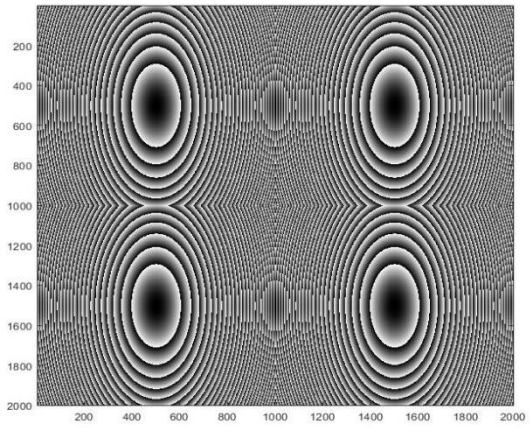

(b) Four targets.

Figure 6- 5 phase pattern of SLM with phase range from 0 to 2π (8 bit).

The phase pattern of FZP of user i ($i \in U_l$, where U_l is the set of all users served by lth AP) is given as [134]:

$$\begin{aligned} &E(x_i, y_i) = \exp\left(-i\pi \frac{(x-x_i)^2+(y-y_i)^2}{\lambda f}\right), \\ &x_{min}^i \le x \le x_{max}^i, \\ &y_{min}^i \le y \le y_{max}^i, \end{aligned} \tag{6-6}$$

where $(x_i,\ y_i)$ is the zone centre of user i, and $(x_{min}^i,\ x_{max}^i)$, $(y_{min}^i,\ y_{max}^i)$ are the range of the area allocated to target j on x and y axis. For multiple targets, Equation (6-5), used to calculate the optical power, is re-defined as:

$$I_i = I_0 sinc\left(\frac{\rho \sin(\phi)}{\lambda}\right)^2 sinc\left(\frac{1}{L}\right)^2 \rho_{SLM}\rho_{AM}\beta_i, \tag{6-7}$$

where β_i is percentage of the area on SLM which is allocated to the user i and $\sum_{j\in U_l}\beta_i = 1$.

6.2.2 NOMA

We consider a realistic indoor environment where multiple APs are mounted on the ceiling as shown in Fig. 6-6. All APs are inter-connected with fibre and connected to a central unit that controls the allocation of the network. Multiple users are distributed in the room. We assume an AP finds the location of the users based on LEA proposed in

[123] and acquire perfect CSI. Considering a maximum AP beam steering angle of 30 degrees, the beam steering range of an AP is partially covered by the service area of adjacent APs. When the user stays in this area, the user will receive the signals from multiple APs. Using NOMA and unipolar intensity modulation (LDs only works in positive area), each AP transmits real and positive signals to intended users. The information for different users are modulated separately, and assigned different power level based on their CSI. After modulating and assigning power, the signals of different users are superimposed or combined together, allowing them to be modulated on LD and conveyed simultaneously. Let us now denote the set of users serviced by the l^{th} AP by U_l. The superposition signal transmitted from the l^{th} AP can be given as [123]:

$$z_l = \sum_{j \in U_l} \eta \sqrt{P_{lj}} x_j, \tag{6-8}$$

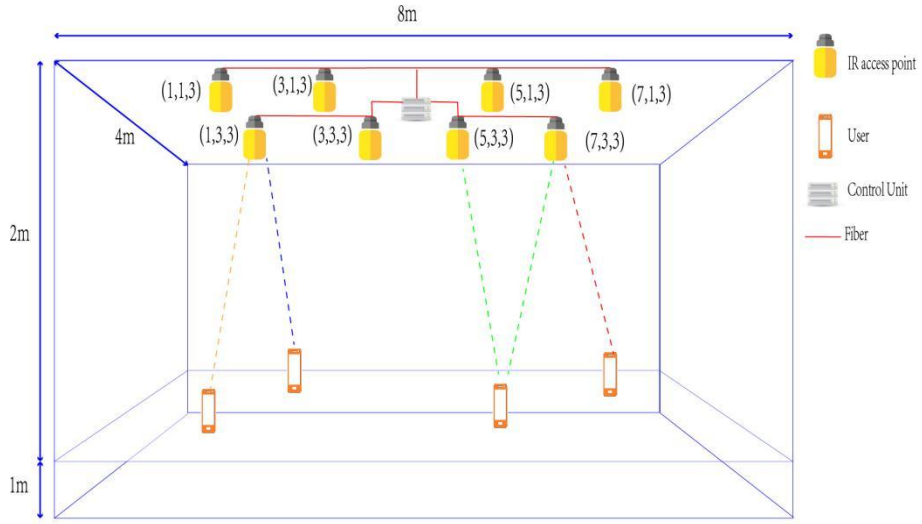

Figure 6- 6 beam steering OWC system for multiuser.

where η is quantum efficiency of the AP, x_i is the signal to user i, z_l is the superposition optical signal from the AP, I_l is the total transmit optical power of the AP and P_l is the total electric power of l^{th} AP. These are defined as:

$$I_l = \sum_{i \in U_l} \eta \sqrt{P_{li}}, \tag{6-9}$$

$$P_l = \sum_{i \in U_l} P_{li}$$

Considering that the users in the room are represented by set S ($i \in U_l$, $U_l \subseteq S$), the received signal at the receiver of user i can be represented as [122]:

$$y_i = \sum_{l=1}^{L} RI_l z_l \otimes h_{li} + n_i, \; i \in U_l \tag{6-10}$$

where L is the total number of APs, n_i is the additive Gaussian noise, which is the sum of the shot noise and thermal noise at the receiver of user i, and h_{li} is the impulse response of the link between AP l and user i. Based on the result in [132], the light beam after the SLM is still a Gaussian beam.

Using SIC, user i decodes the signal of the lower decoding order and treat the signal of high decoding order as noise. The SINR of user i is given as [126]:

$$SINR_i = \sum_{l=1}^{L} \frac{(I_l R_i H_{li})^2}{\sigma_i^2 + \sum_{k>i} (I_{lk} R_i H_{li})^2} \tag{6-11}$$

H_{li} is the channel gain from AP l to the user i. H_{li} can be given as:

$$H_{li} = \int_{-\infty}^{\infty} h_{li}(t) dt. \tag{6-12}$$

The achievable rate of user i is given as:

$$r_i = \frac{1}{2} B \, log_2 \, (1 + SINR_i), \tag{6-13}$$

where the scaling factor ($\frac{1}{2}$) is due to the Hermitian symmetry. The decoding order of the users is related to the CSI, h_{li}, which is collected during the process of the AP locating the user. After APs report the CSIs of all users to the central unit, the decoding order of user i is decided by the sum of CSIs, h_{li}, of all APs:

$$x_1 < x_2 < \cdots < x_i \cdots < x_{N-1} < x_N \Rightarrow \sum_{l=1}^{L} H_{l1} > \sum_{l=1}^{L} H_{l2} > \cdots \sum_{l=1}^{L} H_{li} \cdots > \sum_{l=1}^{L} H_{lN-1} > \sum_{l=1}^{L} H_{lN} \quad (6\text{-}14)$$

where N is total number of users in the room. For l^{th} AP, the power allocation of the i and $i-1$ sorted users ($i, i-1 \in U_l$ and $x_{i-1} < x_i$) are related as:

$$P_{i-1} = \alpha P_i \quad (6\text{-}15)$$

where α is the power allocation factor.

6.2.3 SIC

SIC algorithm is implemented at users with maximum likelihood detector. After the receiver receives and samples the signals of all user groups, decode the user group with the highest power using SIC. By subtracting the decoded user group signals from the received signals, interference from other user groups can be eliminated. Assuming perfect CSI is acquired, user u_1 obtains the superposition optical signal of N users from APs and it is the lowest order of decoding of the received signal ($u_1 < u_2 \cdots < u_N$). The probability of error for user u_1 can be given as [124]:

$$P_{u_1}^{error} = \sum_{m=1}^{2^{N-1}} P\left(d_{x_1,u_1} = 1 \middle| x_1 = 0\right) P(x_1 = 0) \prod_{n=2}^{N} P_m(x_n) + \sum_{m=1}^{2^{N-1}} P\left(d_{x_1,u_1} = 0 \middle| x_1 = 1\right) P(x_1 = 1) \prod_{n=2}^{N} P_m(x_n) \quad (6\text{-}16)$$

where x_1 is the received signal symbol of user u_1, d_{x_1,u_1} is the decoded signal symbol of user u_1, $P(x_1 = 0) and\, P(x_1 = 1)$ are the probability of receiving symbols 0 and 1 respectively, $P\left(d_{x_1,u_1} = 1 \middle| x_1 = 0\right)$ is the probability of user u_1 receiving signal symbol $x_1 = 0$ while the decoded signal symbol of user u_1 is $d_{x_1,u_1} = 1$, $P(d_{x_1,u_1} = 0 | x_1 = 1)$ is the error decoding probability when the received signal symbol of user u_1 is $x_1 = 1$ and $P_m(x_n)$ is the probability of the received symbol to be of high decoding order users. Considering that the symbol of a user may be 1 or 0, there are 2^{N-1} symbol combinations of high decoding order users and the signal received at this user u_1 can be represented as:

$$y_1 = \sum_{l=1}^{L} \left(\sum_{j \in U_l} R\eta \sqrt{P_{l1}} x_1 H_{l1} + \sum_{n=2}^{N} R\eta \sqrt{P_{l1}} x_n H_{l1} \right) + n_1 \quad (6\text{-}17)$$

where n_1 is the additive noise and R is the responsivity of photodetector.

Considering that the symbol of a user can be 1 or 0, x_n can be represented as matrix $\boldsymbol{X_{nm}}$ including all symbol combinations of high decoding order users which is given as:

$$\boldsymbol{X_{nm}} = \begin{bmatrix} x_{2,1} & x_{3,1} & x_{4,1} & \cdots & x_{N-1,1} & x_{N,1} \\ x_{2,2} & x_{3,2} & x_{4,2} & \cdots & x_{N-1,2} & x_{N,2} \\ x_{2,3} & x_{3,3} & x_{4,3} & \cdots & x_{N-1,3} & x_{N,3} \\ \vdots & \vdots & \vdots & \vdots & \vdots & \vdots \\ x_{2,2^{N-1}} & x_{2,2^{N-1}} & x_{3,2^{N-1}} & \cdots & x_{N-1,2^{N-1}} & x_{N,2^{N-1}} \end{bmatrix} = \begin{vmatrix} 0 & 0 & 0 & \cdots & 0 & 0 \\ 0 & 0 & 0 & \cdots & 0 & 1 \\ 0 & 0 & 0 & \cdots & 1 & 0 \\ 0 & 0 & 0 & \cdots & 1 & 1 \\ \vdots & \vdots & \vdots & \vdots & \vdots & \vdots \\ 1 & 1 & 1 & 1 & 1 & 1 \end{vmatrix} \quad (6\text{-}18)$$

where each row (m) of the matrix $\boldsymbol{X_{nm}}$ represents a possible combination of the signal symbols of high decoding order users. The element of $\boldsymbol{X_{nm}}$ can be represented as x_{nm} which represents the signal symbol of user n of the combination m.

We assume the symbols of different users are independent and are equi-probable. Equation (6-16) is re-defined as:

$$\begin{aligned} P_{u_1}^{error} = & \sum_{m=1}^{2^{N-1}} \frac{1}{2^N} P\Big(\sum_{n=2}^{N}\sum_{j\in U_l} R\eta\sqrt{P_{l1}}x_{nm}H_{l1} + n_1 > i_{x_1,u_1}\Big) \\ & + \sum_{m=1}^{2^{N-1}} \frac{1}{2^N} P\Big(\sum_{n=2}^{N}\sum_{j\in U_l} R\eta\sqrt{P_{l1}}x_{nm}H_{l1} + n_1 \\ & + \sum_{j\in U_l} R\eta\sqrt{P_{l1}}\,H_{l1}\Big) < i_{x_1,u_1}\Big) \end{aligned} \quad (6\text{-}19)$$

where $i_{x_1,u_1} = R\eta\sqrt{P_{l1}}x_1H_{l1}/2$ is the threshold of user u_1 for distinguishing the received symbol x_1. Equation (6-19) can be transformed based on Gauss error function as follows [124]:

$$\begin{aligned} P_1^{error} = & \sum_{m=1}^{2^{N-1}} \frac{1}{2^N} Q\Big(\frac{R\eta\sqrt{P_{l1}}H_{l1} - 2\sum_{n=2}^{N} R\eta\sqrt{P_{l1}}x_{nm}H_{l1}}{2\sigma_{u_1}}\Big) \\ & + \sum_{m=1}^{2^{N-1}} \frac{1}{2^N} Q\Big(\frac{2\sum_{n=2}^{N} R\eta\sqrt{P_{l1}}x_{nm}H_{l1} + R\eta\sqrt{P_{l1}}H_{l1}}{2\sigma_{u_1}}\Big) \end{aligned} \quad (6\text{-}20)$$

where σ_{u_1} is additive noise at user u_1. Considering user u_2 as the second priority in the decoding order, the probability of error for user $u_2$can be given as:

$$P_{u_2}^{error} = (P_{x_2,u_2}^{error})' P_{x_1,u_2}^{error} + (1 - P_{x_1,u_2}^{error})(P_{x_2,u_2}^{error})'' \tag{6-21}$$

where P_{x_1,u_2}^{error} is the error probability of the symbol x_1 of user u_1 being decoded at user u_2, $(P_{x_2,u_2}^{error})''$ is the error probability of user u_2 decoding the symbol x_2, when the symbol x_1 of user u_1 is successfully decoded at user u_2 and $(P_{x_2,u_2}^{error})'$ is the error probability of user u_2 decoding the symbol x_2 when the symbol x_1 of user u_1 is unsuccessfully decoded at user u_2. P_{x_1,u_2}^{error} can be give as:

$$\begin{aligned} P_{x_1,u_2}^{error} = \\ \sum_{m=1}^{2^{N-1}} P\left(d_{x_1,u_2} = 1 \middle| x_1 = 0\right) P(x_1 = 0) \prod_{n=2}^{N} P_m(x_n) \\ + \sum_{m=1}^{2^{N-1}} P(d_{x_1,u_2} = 0 | x_1 = 1) P(x_1 = 1) \prod_{n=2}^{N} P_m(x_n) \end{aligned} \tag{6-22}$$

where d_{x_1,u_2} is the decoded signal symbol of user u_1 at user u_2. Based on Equations (6-18), and (6-19), Equation (6-22) can be rewritten as:

$$\begin{aligned} P_{x_1,u_2}^{error} = \sum_{m=1}^{2^{N-1}} \frac{1}{2^N} P\left(\sum_{n=2}^{N} R\eta\sqrt{P_{l1}} x_{nm} H_{l2} + n_2 > i_{x_1,u_2}\right) + \\ \sum_{m=1}^{2^{N-1}} \frac{1}{2^N} P\left(\sum_{n=2}^{N} R\eta\sqrt{P_{l1}} x_{nm} H_{l2} + n_2 + R\eta\sqrt{P_{l1}} H_{l2} < i_{x_1,u_2}\right) \end{aligned} \tag{6-23}$$

where $i_{x_1,u_2} = R\eta\sqrt{P_{l1}} x_1 h_{l2}/2$ is the threshold for distinguishing the symbol x_1 at user u_2. Equation (6-23) can be transformed based on Gauss error function as follows:

$$P_{x_1,u_2}^{error} = \sum_{m=1}^{2^{N-1}} \frac{1}{2^N} Q\left(\frac{R\eta\sqrt{P_{l1}}H_{l2} - 2\sum_{n=2}^{N} R\eta\sqrt{P_{l1}}x_{nm}H_{l2}}{2\sigma_{u_2}}\right) + \sum_{m=1}^{2^{N-1}} \frac{1}{2^N} Q\left(\frac{2\sum_{n=2}^{N} R\eta\sqrt{P_{l1}}x_{nm}H_{l2} + R\eta\sqrt{P_{l1}}H_{l2}}{2\sigma_{u_2}}\right) \tag{6-24}$$

The signal at user u_2 after successful implementation of SIC is given as:

$$y_2^{'} = \sum_{j\in U_l} R\eta\sqrt{P_{l2}}x_2h_{l2} + \sum_{n=3}^{N} R\eta\sqrt{P_{l2}}x_nh_{l2} + n_2 \tag{6-25}$$

With the threshold $i_{x_2,u_2} = \sum_{j\in U_l} R\eta\sqrt{P_{l2}}x_2h_{l2}/2$ for the symbol x_2 decode at user u_2, the error probability $(P_{x_2,u_2}^{error})^{''}$ is given as:

$$(P_{x_2,u_2}^{error})^{''} = \sum_{m=1}^{2^{N-2}} \frac{1}{2^{N-1}} P\left(\sum_{n=3}^{N} R\eta\sqrt{P_{l2}}x_{nm}h_{l2} + n_2 > i_{x_2,u_2}\right) + \sum_{m=1}^{2^{N-2}} \frac{1}{2^{N-1}} P\left(\sum_{n=3}^{N} R\eta\sqrt{P_{l2}}x_{nm}h_{l2} + n_2 + R\eta\sqrt{P_{l2}}h_{l2}\right) < i_{x_2,u_2}\Big) \tag{6-26}$$

Based on Equation (6-18) and (6-19), Equation (6-26) can be transformed into:

$$\left(P_{x_2,u_2}^{error}\right)^{''} = \sum_{m=1}^{2^{N-2}} \frac{1}{2^{N-1}} Q\left(\frac{R\eta\sqrt{P_{l2}}h_{l2} - 2\sum_{n=3}^{N} R\eta\sqrt{P_{l2}}x_{nm}h_{l2}}{2\sigma_{u_2}}\right) + \sum_{m=1}^{2^{N-2}} \frac{1}{2^{N-1}} Q\left(\frac{2\sum_{n=3}^{N} R\eta\sqrt{P_{l2}}x_{nm}h_{l2} + R\eta\sqrt{P_{l2}}h_{l2}}{2\sigma_{u_2}}\right) \tag{6-27}$$

On the contrary, if the implementation of SIC failed at user u_2, the received signal $y_2^{''}$ is given as:

$$y_2^{''} = R\eta\sqrt{P_{l1}}x_1H_{l2} + R\eta\sqrt{P_{l2}}x_2H_{l2} + \sum_{n=3}^{N} R\eta\sqrt{P_{l2}}x_nH_{l2} + n_2 - R\eta\sqrt{P_{l1}}\widehat{x_1}H_{l2} \tag{6-28}$$

where $\widehat{x_1}$ represents the error decoding sample of x_1 at user u_2. The relevant error probability $(P_{x_2,u_2}^{error})^{'}P_{x_1,u_2}^{error}$ is represented by the following equation:

$$\begin{aligned}(P_{x_2,u_2}^{error})^{'}P_{x_1,u_2}^{rror} = &\sum_{m=1}^{2^{N-2}} P(d(x_2,u_2)=1)P(d(x_1,u_2)=1)P(x_1=0)P(x_2=0)\prod_{n=3}^{N}P_m(x_n) \\ &+ \sum_{m=1}^{2^{N-2}} P(d(x_2,u_2)=0)P(d(x_1,u_2)=1)P(x_1=0)P(x_2=1)\prod_{n=3}^{N}P_m(x_n) \\ &+ \sum_{m=1}^{2^{N-2}} P(d(x_2,u_2)=1)P(d(x_1,u_2)=0)P(x_1=1)P(x_2=0)\prod_{n=3}^{N}P_m(x_n) \\ &+ \sum_{m=1}^{2^{N-2}} P(d(x_2,u_2)=0)P(d(x_1,u_2)=0)P(x_1=1)P(x_2=1)\prod_{n=3}^{N}P_m(x_n)\end{aligned} \tag{6-29}$$

With the threshold $i_{x_2,u_2} = \sum_{j\in U_l} R\eta\sqrt{P_{l2}}x_2h_{l2}/2$ for symbol x_2 decoded at user u_2, the error probability $(P_{x_2,u_2}^{error})^{'}P_{x_1,u_2}^{error}$ is transformed into Q function mode as：

$$\begin{aligned}(P_{x_2,u_2}^{error})^{'}P_{x_1,u_2}^{error} = &\sum_{m=1}^{2^{N-2}} \frac{1}{2^N}\Big(Q\big((\sqrt{P_{l1}} - 2\sum_{n=3}^{N}\sqrt{P_{l1}}x_{nm})\omega\big)Q\big((\sqrt{P_{l2}} - 2\sum_{n=3}^{N}\sqrt{P_{l2}}x_{nm} + 2\sqrt{P_{l1}})\omega\big) \\ &+ Q\Big(\big(\sqrt{P_{l1}} - 2\sum_{n=3}^{N}\sqrt{P_{l1}}x_{nm} - 2\sqrt{P_{l2}}\big)\omega\Big)Q\Big(\big(2\sum_{n=3}^{N}\sqrt{P_{l2}}x_{nm} + \sqrt{P_{l2}} - 2\sqrt{P_{l1}}\big)\omega\Big) \\ &+ Q\Big(\big(\sqrt{P_{l1}} + 2\sum_{n=3}^{N}\sqrt{P_{l1}}x_{nm}\big)\omega\Big)Q\Big(\big(-2\sum_{n=3}^{N}\sqrt{P_{l2}}x_{nm} + \sqrt{P_{l2}} - 2\sqrt{P_{l1}}\big)\omega\Big) \\ &+ Q\Big(\big(\sqrt{P_{l1}} + 2\sum_{n=3}^{N}\sqrt{P_{l1}}x_{nm} + 2\sqrt{P_{l2}}\big)\omega\Big)Q\Big(\big(2\sum_{n=3}^{N}\sqrt{P_{l2}}x_{nm} + \sqrt{P_{l2}} + 2\sqrt{P_{l1}}\big)\omega\Big)\Big)\end{aligned} \tag{6-30}$$

where $\omega = R\eta h_{l2}/2\sigma_{u_2}$. Finally, substituting Equation (6-22), (6-27) and (6-30) into (6-21), we can get the error probability of user u_2. Similarly, for user $u_k(\,1 \le k < N)$, the error probability of user u_k is given as [135]:

$$P_{u_k}^{error} = \sum_{m=1}^{2^{k-1}} P_{x_k,u_k,m}^{error} \prod_{n=1}^{k-1} \left| y_{mn} - P_{x_n,u_k}^{error} \right| \tag{6-31}$$

where P_{x_n,u_k}^{error} represents the error probability of symbol x_n for user $u_n(n < k)$ being decoded at user u_k, $P_{x_k,u_k,m}^{error}$ represents the error probability of decoding x_k at user u_k of SIC implementation situation m, and y_{mn} is the elements of matrix $\boldsymbol{Y_{mn}}$ which is given as:

$$\boldsymbol{Y_{mn}} = \begin{bmatrix} y_{1,1} & y_{1,2} & \cdots & y_{1,k-1} \\ y_{2,1} & y_{2,2} & \cdots & y_{2,k-1} \\ \vdots & \vdots & \vdots & \vdots \\ y_{2^{k-1},1} & y_{2^{k-1},2} & \cdots & y_{2^{k-1},k-1} \end{bmatrix} = \begin{vmatrix} 0 & 0 & 0 & \cdots & 0 & 0 \\ 0 & 0 & 0 & \cdots & 0 & 1 \\ 0 & 0 & 0 & \cdots & 1 & 0 \\ 0 & 0 & 0 & \cdots & 1 & 1 \\ \vdots & \vdots & \vdots & \vdots & \vdots & \vdots \\ 1 & 1 & 1 & 1 & 1 & 1 \end{vmatrix} \quad (6\text{-}32)$$

where $y_{m,n} = 0$ represents that the decoding of symbol x_n at user u_k is a failure while $y_{m,n} = 1$ represents that the decoding of symbol x_n at user u_k is a success. Each row of the matrix $\boldsymbol{Y_{mn}}$ represents a possible situation of the symbols.

6.3 Simulation setup and results for a NOMA system without relay terminals

To evaluate the performance of a NOMA system in an indoor IR-based OWC system, we consider an empty room with the dimensions of 8m × 4m × 3m (length × width × height) as in Fig. 6-7. The room configuration is the same setup in Chapter 3. Additional simulation parameters to those in Table3-1 are given in Table 6-1.

Table 6- 1 ROOM SETUP

Parameter	Configuration
IR AP	
Quantity	8
Location of Access Points	(1, 1, 3) (1, 3, 3) (1, 5, 3) (1, 7, 3) (3, 1, 3) (3, 3, 3) (3, 5, 3) (3, 7, 3)

Power	1 mW	
beam divergency	2.1 mrad	
user		
Quantity	1	
Elevation	90º	
Azimuth	0º	
FOV	90º	
area	1 cm^2	
The responsivity of IR	0.5 A/W	
The responsivity of illumination	0.4 A/W	
Resolution		
Time bin duration	0.01 ns	
Bounces	1st reflection	2nd reflection
Surface elements	32000	2000
Wavelength	850 nm	
Bandwidth (BW)	10 GHz	

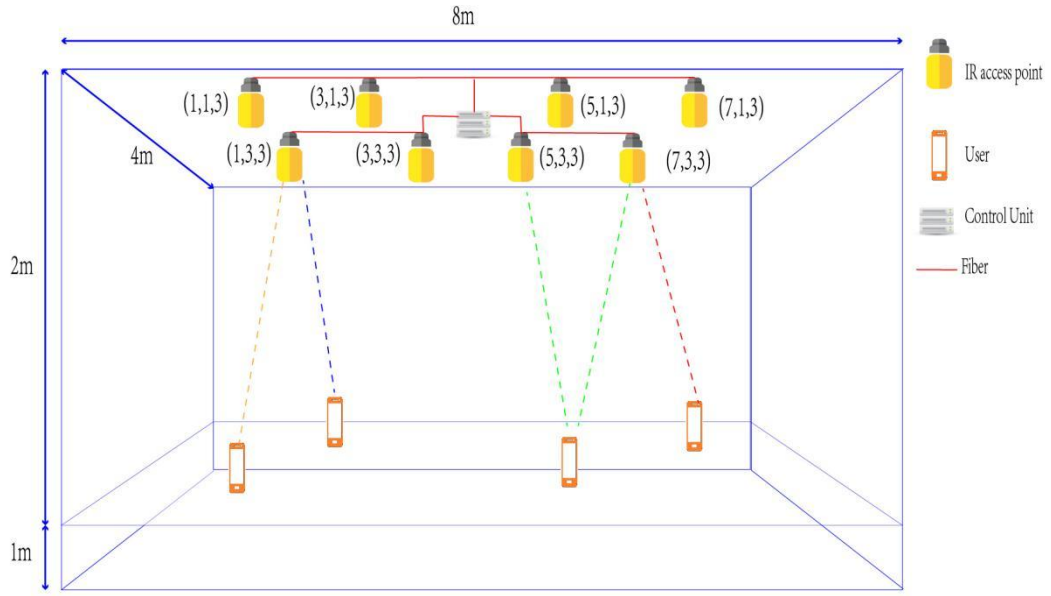

Figure 6- 7 The room setup of beam steering multiuser system

The locations of the APs are shown as Fig. 6-7. 8 APs are interconnected by fibre and controlled by a central controller. Considering 4 to 10 users in the room, their locations are randomly generated following a uniform distribution [141]. According to [134], the light beam after the SLM is still a Gaussian beam. The transmitted Gaussian beam has an irradiance distribution as follows [142]:

$$I(r) = \frac{2I}{\pi\omega^2} e^{\frac{-2r^2}{\omega^2}}, \tag{6-33}$$

where I is the total transmitted optical power by the SLM as in Equation (6-5), r is the transverse distance from the normal axis of AP, and ω is the distance from the centre axis of the beam where the irradiance drops to $\frac{1}{e^2}$ which is defined as [142]:

$$\tan\theta = \frac{\omega(z)}{z}, \tag{6-34}$$

where θ is the angle of divergence of the Gaussian light beam, and z is distance between the AP and the user plane as shown in Fig.6-8. The power contained within radius r, is obtained by integrating power from 0 to r as [142]:

$$P(r) = \int_0^r I(r)dr \tag{6-35}$$

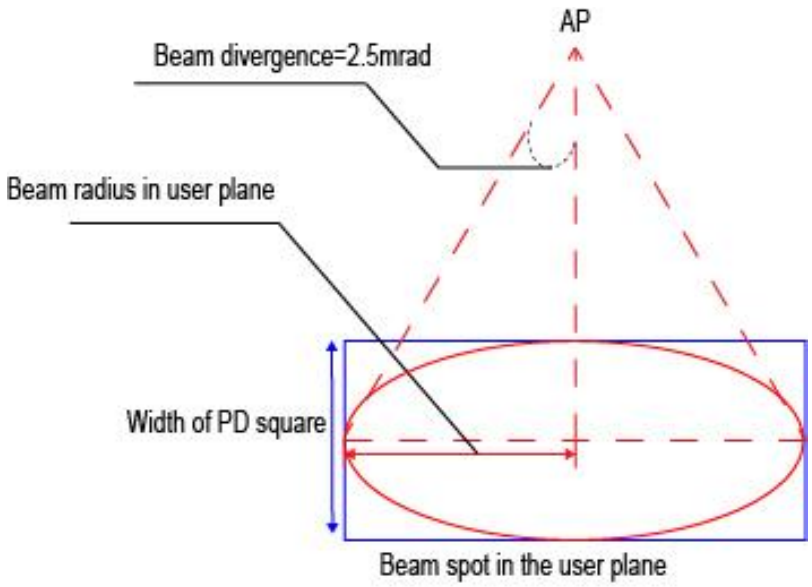

Figure 6- 8 Gaussian beam spot at user plane.

The on-axis beam divergency of the Gaussian beam from the AP is 2.5 mrad [142]. Considering that the user moves on the communication plane, which is 1m above the floor as shown in Fig.6-7, APs only scan the square area whose length equals to 1m in the vicinity of the AP. The beam spot with $r = 0.05\,m$ on the user plane contains 87% of the optical power from the AP. For $r = 0.25\,m$, the beam spot on the user plane is almost 100% of the optical power from the AP. Because the walls and floor are already modelled as Lambertian reflectors, when partial power of light beam is reflected by the floor, it becomes a second order Lambertian source. The received power P_u is the sum of contribution from the Gaussian LOS beam and the Lambertian NLOS reflection from the walls, ceiling and floor. $P_u$is given as:

$$P_u = P_{LOS} + P_{NLOS1} + P_{NLOS2} \tag{6-36}$$

where P_{LOS} is the LOS component of received light power as in Equation (3-4), and P_{NLOS1} and P_{NLOS2} are the first order and second order NLOS component of the received light power. P_{LOS} is given as:

$$P_{LOS} = \int_0^{\frac{d}{2}} \frac{2\mathrm{I}}{\pi\omega^2} e^{\frac{-2r^2}{\omega^2}} \cos\delta \, dr, \tag{6-37}$$

where d is the diameter of the photodetector. P_{NLOS1} is given as:

$$P_{NLOS1} = \sum_{i=1}^{N} \int_0^{\frac{d_1}{2}} \frac{2I}{\pi\omega^2} e^{\frac{-2r^2}{\omega^2}} cos\,\alpha \, dr \frac{(n_1+1)}{4\pi^2 R_1^2} \rho_1 \cos^{n_2}\beta \cos\delta dA \, rect(\delta/FOV) \tag{6-38}$$

where d_1 is the diameter of reflecting element for first order, n_1 is the radiation mode of a reflection element for the first order, R_1 is the Euclidian distance between the reflection element and receiver, ρ_1 is the reflection efficiency of the reflecting element for the first order, α is the ray incident angle to the normal of the reflecting element, β is the angle between the normal to the reflecting element and the emitting direction, and dA_1 is the integration of the photodetector area of the reflection element for the first order. P_{NLOS2} is defined as:

$$P_{NLOS2} = \sum_{i=1}^{M} \int_0^{\frac{d_1}{2}} \frac{2\mathrm{I}}{\pi\omega^2} e^{\frac{-2r^2}{\omega^2}} \cos\alpha \, dr \frac{(n_1+1)(n_2+1)}{4\pi^2 R_1^2 R_2^2} \rho_1\rho_2 \cos^{n_1}\beta \cos\gamma \cos^{n_2}\varepsilon \cos\delta dA \, dA_2 rect(\delta/FOV) \tag{6-39}$$

where n_2 is the mode number of the radiation pattern of the reflecting element for the second order, R_1 is the Euclidian distance between the reflection element for the first order and the reflection element for second order, R_2 is the Euclidian distance between the reflection element for second order and receiver, ρ_2 is reflection efficiency of the reflecting element for second order, γ is the angle between the normal of reflecting element for second order and incident signal, ε is the angle between the normal of reflecting element for second order and emitting direction, dA_2 is the integration of the photodetector area of the reflection element in second order and M is total number of element for second order.

We study different scenarios representing different number of users. For each scenario, the simulation is repeated for 100 times to generate different user locations and the power allocation factor α is varied between 0.2 to 0.8. Fig. 6-9 shows the sum rate of

the system versus the power allocation factor considering different numbers of users. It can be seen that the sum rate decreases as the power allocation factor increases. Note that, an increase in α means that the users classified as weak users according to their channel gains receive low power, and therefore low SINR is experienced by these users. On the other hand, the strong users receive high power as α increases. However, the sum rate decreases due to the fact that the strong users apply SIC to decode their information, and high power allocated to the strong users increases noise. The figure further shows that the sum rate increases with the number of users, which is expected as all the users in the network experience different channel gains.

Fig. 6-10(a) shows the average BER for different number of users versus power factor α and Fig. 6-10(b) zooms up the BER of the scenarios where 4, 5, and 6 users are considered. For $\alpha \leq 0.5$, the BER of all scenarios decreases as the power allocation factor increases, since each user receives a decent power level to decode the desired information. However, when $\alpha > 0.5$, high power is allocated to the users with high channel gains, which negatively impacts the SINR of the system. Note that, the signal intensity difference between the users increases when $\alpha = 0.8$, which leads to high probability of successive decoding for the strong users at the cost of low fairness. However, the results show that a power allocation factor of 0.4 is a good choice to achieve high sum rate and low BER.

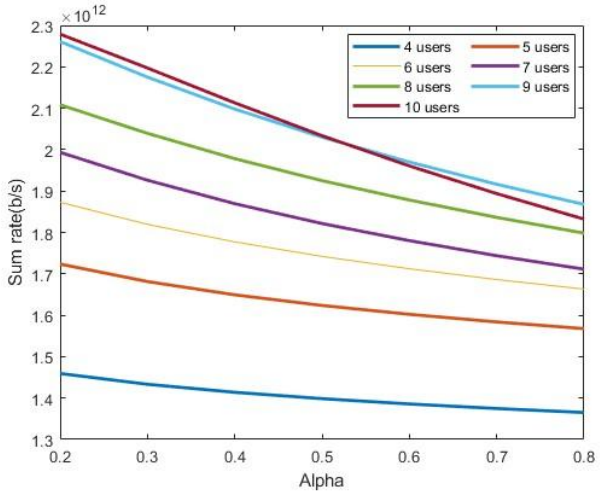

Figure 6- 9 the sum rates of users versus the power allocation factor of NOMA.

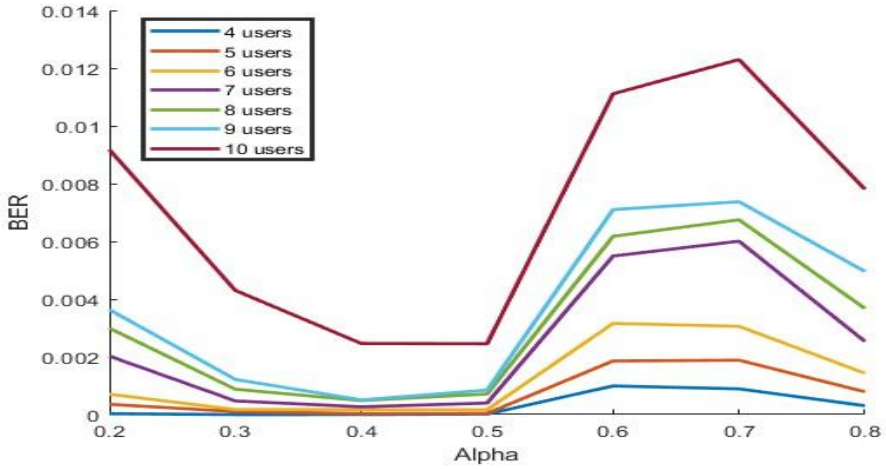

(a)

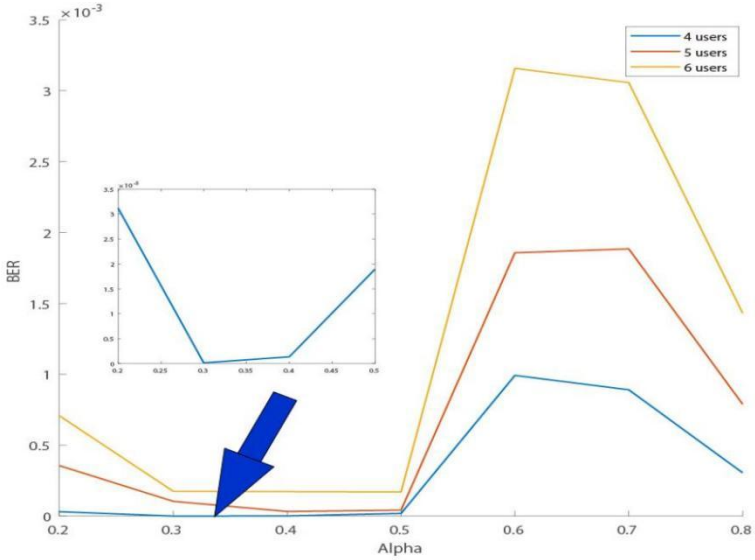

(b)

Figure 6- 10 Average BER against the power allocation factor.

6.4 Relay cooperative NOMA system based on RWP model

6.4.1 RWP model of human moving in the room

Compared with the shadowing and blockage due to the furniture and devices in the room, the shadowing and blockage due to humans moving in the room (Fig. 6-11) is

unpredictable and irregular, we consider the RWP model where the human moves along a straight line at a uniform velocity to a random destination in the room, before reaching its destination, the human selects another destination randomly according to a uniform distribution and moves toward it at a different velocity. For the sake of simplicity and without loss of generality, we use the RWP model without any pause time at any destination. As the human continues moving in the room, the probability density function P_{pdf} of this human location in a rectangle room is defined as follows [84]:

$$P_{pdf} = f(x)f(y) = \frac{36}{x_m^3 y_m^3}\left(x^2 - \frac{x_m^2}{4}\right)\left(y^2 - \frac{y_m^2}{4}\right), \quad -\frac{X_m}{2} \le x \le \frac{X_m}{2}, -\frac{Y_m}{2} \le y \le \frac{Y_m}{2} \tag{6-40}$$

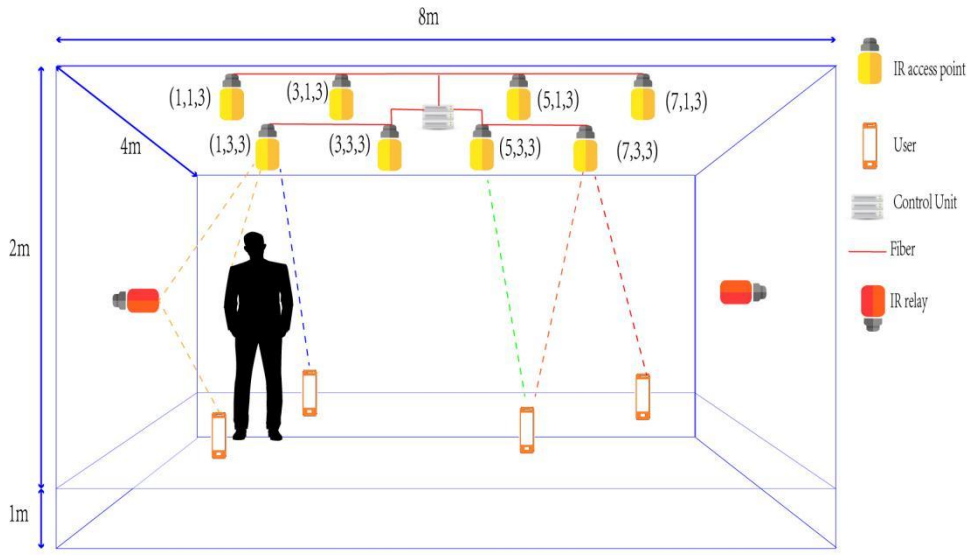

Figure 6- 11 Human body block the signal from the access points.

where (x, y) is the location of this human on the floor, (x_m, y_m) are the dimensions of the floor. The probability density function of the location of the human in the room can be represented as in Fig. 6-12. A human is modelled as a cylinder (Height=1.8m, Radius=0.3m). For a link between transmitter (x_t, y_t, z_t) and receiver (x_r, y_r, z_r), where the transmitter can be an AP or a relay terminal, and the receiver can be a relay terminal

or a user, we can find an area S in the (x, y) plane that the human (cylinder) may block the direct link between the transmitter and the receiver. The method for calculating the blocked area is given in Appendix A. To reduce computing complexity, the narrow Gaussian beam is simplified as a straight line.

The cumulative probability density function $P_{l_{tr}}$ for a blocked LOS link l_{tr} between the transmitter (x_t, y_t, z_t) and the receiver (x_r, y_r, z_r) is given by:

$$P_{l_{tr}} = P_{cdf} = \iint_S f(\quad) f(y) \tag{6-41}$$

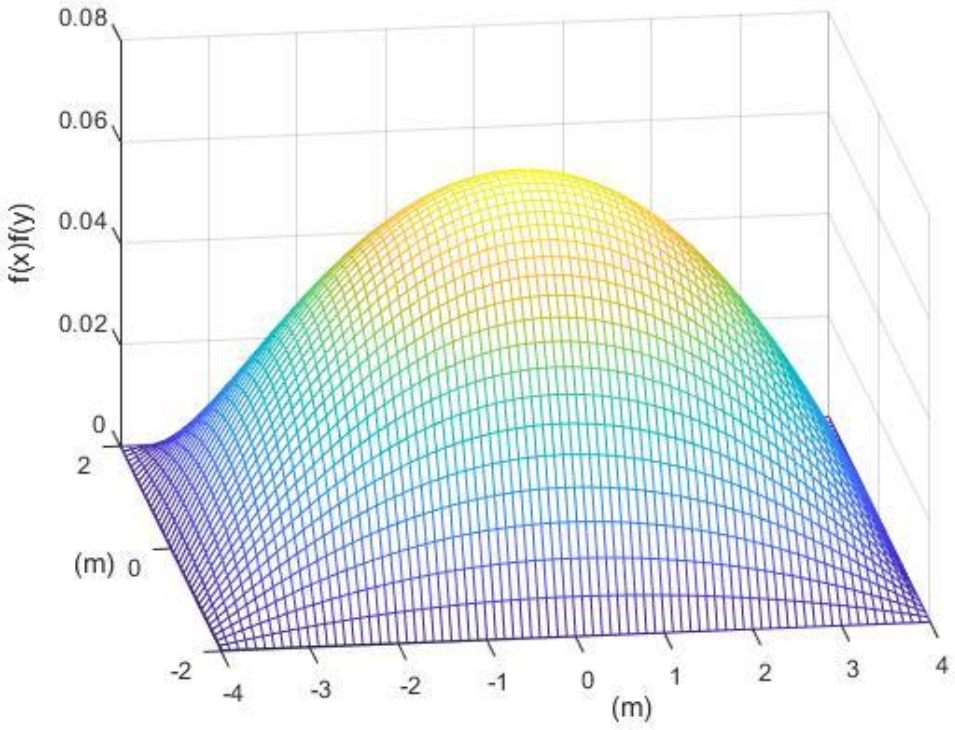

Figure 6- 12 Probability density of RWP in the room.

where $P_{l_{tr}}$ is the probability that link l_{tr} is blocked by the human. Considering M persons randomly and independently moving in the room. The probability $P_{l_{tr}}^{M}$ of link l_{tr} been blocked is defined by:

$$P_{l_{tr}}^{M} = 1 - (1 - P_{l_{tr}})^{M} \tag{6-42}$$

Considering a signal from AP (x_a, y_a, z_a) to reach user (x_u, y_u, z_u) via a relay node (x_n, y_n, z_n), the probability $P_{l_{tnu}}^{M}$ of link l_{tnu} to be blocked is defined as following:

$$P_{l_{tnu}}^{M} = 1 - (1 - P_{l_{tn}})^{M} \times (1 - P_{l_{nu}})^{M} \tag{6-43}$$

where $P_{l_{tn}}^{M}$ is the probability that a link between the AP and the relay node is blocked and $P_{l_{nu}}$ is the probability that the link between the user and the relay node is blocked.

To evaluate the impact of the human body blockage, the outage probability, adopted as the performance metric, is defined as follows:

$$P_{out} = \mathrm{P}(SNR_u \leq SNR_{th}) \tag{6-44}$$

where SNR_{th} is the SNR threshold (15.6dB) for normal communication which is equivalent to bit error rate of 10^{-9} [25].

6.4.2 Direct and relay cooperative communication modes

Two different communication modes are considered in studying the influence of human blockage. The first mode is direct communication mode. APs directly send signal to users as in Section 6.3. The second mode is cooperative communication mode based on relay terminals. For cooperative communication mode, APs send signals to users and relay terminals in its vicinity. Compared with DF relay terminal, the structure of O-E-O amplify-and-forward relay terminal is relatively simpler, but the optical signal needs to be decoded at DF relay terminal before being forwarded to a user. The superposition of signals of multiple users increases the probability of decoding error at DF relay terminals. Therefor O-E-O amplify-and-forward relay terminals are considered in this chapter. As is given in Fig. 4-2, the optical signal from the AP is transformed into an electrical signal via a PIN photodetector. Then, the electrical signal as well as

the noise are amplified by an electrical amplifier before using it to modulate an IR laser. Then the amplified signal is forwarded to the user. We assume that the parameters of the O-E-O amplify-and-forward relay terminal are constant within the noise equivalent bandwidth. The MRC algorithm is used at the user's device to combine the received signals. For the direct communication mode, considering the influence of the blockage and shadowing, Equation (6-11) is redefined as:

$$SINR_i = \frac{\sum_{l=1}^{L} (\beta_{li} P_{li} R_i H_{li})^2}{\sigma_i^2 + \sum_{l=1}^{L} \sum_{k>i} (\beta_{li} P_{lk} R_i H_{li})^2} \tag{6-45}$$

where β_{li} is the blockage factor for the link between AP l and user i which is defined as:

$$\beta_{li} = \begin{cases} 1 & if\ link\ is\ not\ blocked \\ 0 & if\ link\ li\ is\ blocked \end{cases} \tag{6-46}$$

We can get the probability P_{li} of $\beta_{li} = 1$ as follows:

$$P_{li} = 1 - \left(1 - P_{cdf}\right)^m = 1 - \left(1 - \iint_S P_{pdf}\right)^m \tag{6-47}$$

where P_{cdf} is the cumulative density function of a human moving in the room, P_{pdf} is the probability density function of a human moving in the room, m is the number of humans in the room, and S is the area that a human will block.

For cooperative communication, in the first phase, each AP sends the signal to the user and only one relay node in its vicinity. The AP produces an extra beam steering target to that relay node. The received signal in the first phase at user i (y_i^1) and relay node r (y_r^1), where $r \in R,$ are defined as the following:

$$y_i^1 = \sum_{l=1}^{L} R P_i z_l \otimes h_{li} + n_i \tag{6-48}$$

$$y_r^1 = \sum_{l=1}^{L} RP_r z_l \otimes h_{lr} + n_r \tag{6-49}$$

where z_l is the superposition symbols of different users, P_i and P_t are the optical power allocated to user i and relay node r, and h_{li} and h_{lr} are the channels from AP l to user i and relay node r, and $n_i \; and \; n_r$ are the additive Gaussian noise at user i and relay node r.

In the second phase, relay r sends an amplified signal to user i. The received signal from the relay nodes is defined as:

$$y_i^2 = \sum_{r \in R} R(\frac{hf}{q}\eta_g \quad {}_A y_r^1 \otimes h_{ti}) + n_i, \tag{6-50}$$

where R is the set of relay nodes, f is the centre frequency, h is Planck's constant, q is the elementary charge, η_g is the external quantum efficiency of the relay terminal, and G_A is the amplifier gain of the O-E-O relay terminal. MRC is used to combine the received signal from both phases applied at user (i.e., y_i^1 and y_i^2) through an adder circuit. The output signals are combined using MRC. Each input to the circuit is directly proportional to its SNR by adding a relevant weight as in Equation (2-3) and (2-4). The SINR of user i based on cooperative communication is given as:

$$\begin{aligned} SINR_i^{MRC} &= SINR_i^{1st\ phase} + SINR_i^{2nd\ phase} \\ &= \frac{\sum_{l=1}^{L} (\beta_{li} P_{li} R_i H_{li})^2}{\sigma_i^2 + \sum_{l=1}^{L} \sum_{k>i} (\beta_{li} P_{lk} R_i H_{li})^2} \\ &+ \frac{\sum_{r \in R} (\gamma_{lri} P_{li} R_i H_{lr} H_{ri})^2}{\sigma_i^2 + \sum_{k>i} (\gamma_{lri} I_{lk} R_i H_{lr} H_{ri})^2 + \sum_{r \in R} \gamma_{lri} \sigma_r^2} \end{aligned} \tag{6-51}$$

where γ_{lri} is the blockage factor for the link between AP l and user i via relay r which is defined as:

$$\gamma_{lri} = \begin{cases} 1 \quad if\ the \text{ link between AP } l \\ \text{and user } i \text{ via relay } ris\ not\ blocked \\ 0 \quad if\ the\ the \text{ link between AP } l \\ \text{and user } i \text{ via relay } r \ \ is\ blocked \end{cases} \tag{6-52}$$

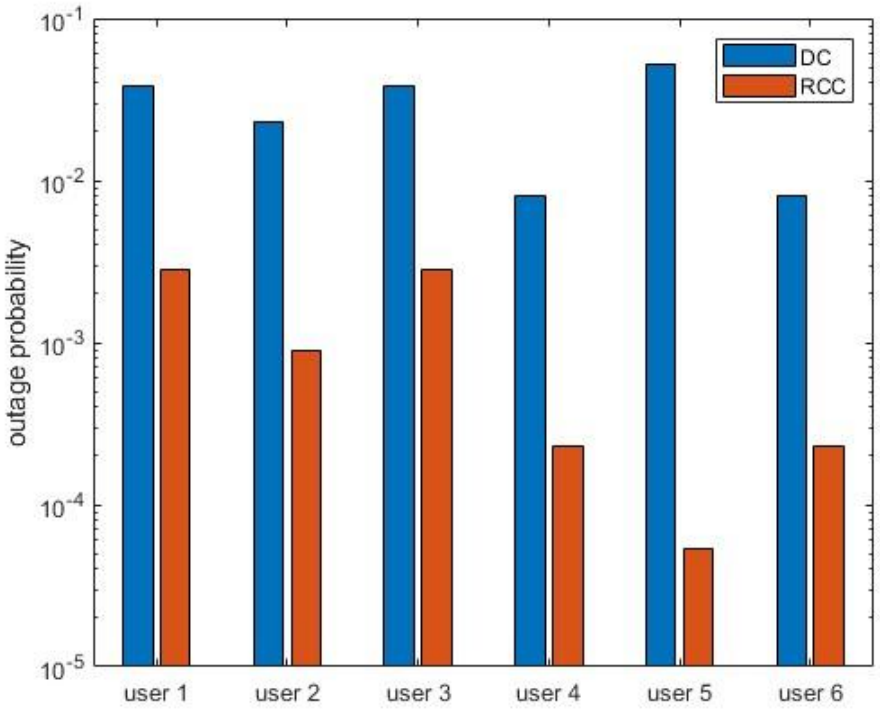

Figure 6-13 The outage probability of direct communication mode and relay cooperative communication mode.

The equation for calculating the probability of $\gamma_{lri} = 1$ is the same as Equation (6-50). The noise term σ_r^2 is discussed in Section 4.2.2.1 in Equations (4-7), (4-8), (4-9) and (4-10). We assume that there are six users in the room. Their locations are given as (1m,1m,1m), (1m,4m,1m), (1m,7m,1m), (2m,1m,1m), (2m,4m,1m) and (2m,7m,1m). The locations of the users are set to represent different situations where the users are served by 1, 2 or 4 APs. There are eight relay terminals mounted on the walls. Each of the relays can receive the signal from one AP. The locations of the relay terminals are (0m, 1m, 1.5m), (0m, 3m, 1.5m), (0m, 5m, 1.5m), (0m, 7m, 1.5m), (4m, 1m, 1.5m), (4m, 3m, 1.5m), (4m, 5m, 1.5m) and (4m, 7m, 1.5m). The outage probability of the two communication modes are shown in Fig. 6-13. The outage probability of cooperative

communication mode is lower than direct communication mode for all users. For user 5, the outage probability of the cooperative communication mode is almost three orders of magnitude lower than the direct communication mode. User 5 is located at the centre of the room. The outage probability of direct communication mode of user 5 is higher than other users. With cooperative communication, user 5 can receive signals from 4 relay terminals which efficiently reduces the influence of the blockage. Compared with user 5, the outage probability degradations of the other users are distributed in the range from one order of magnitude to two orders of magnitude. The degradation degree is related to the number of relay nodes that provide service to each user.

6.5 Summary

In this chapter, a beam steering OWC multi-user system based on NOMA is introduced. We investigated the achievable bit rate and BER of the proposed system while changing the power allocation factor, α. The achievable rate of users is degraded when increasing the power allocation factor while the BER fluctuates with increase in the power allocation factor. The results show that a balance between the BER and the achievable rate can be achieved when $\alpha = 0.4$.

We also proposed using cooperative communication based on optoelectronic (O-E-O) amplify-and-forward relay terminals to reduce the influence of the blockage and shadowing resulting from human movement in a beam steering Optical Wireless Communication (OWC) system. The cooperative communication system consists of two phases. In the first phase, APs transmit the signal to relay terminals and user. In second phase, relay terminals forward the received signal to users. The user combines the signals of the two phases using MRC. The simulation results show that outage probability of the cooperative communication mode is two orders of magnitude lower on average than direct communication without relay terminals. The results show that the user that has links with more relay terminals observes higher robustness to the human body blockage.

Chapter 7: Conclusions and Future Work

7.1 Conclusions

Understanding and tackling the design challenges of indoor OWC systems, such as ambient noise, multipath dispersion, the shadowing and blockage due to humans, and eye and skin safety regulations is important for practical implementation of indoor OWC systems. In Chapter 3, we modelled and analysed the characteristics of the indoor optical wireless channel by developing a ray-tracing algorithm that considers direct LOS (Lambertian and Gaussian light source) and first and second order reflections (Lambertian reflections). We first studied a CDS system, which is a basic infrared OWC system that depends more on the diffuse reflections due to the ceiling and walls and less on the LOS link. It allows the system to operate even when the receiver is obstructed from the transmitter. Nonetheless, a diffuse transmitter is subject to multipath dispersion, which may result in pulse spread and ISI. The considered systems were evaluated in a typical rectangular room with a size of (4m × 8m× 3m) (width × length× height). The simulation results were performed by using a light ray-tracing algorithm where the transmitted optical signal travels through various paths (direct, first, and second order reflections) with different distances before it reaches the receiver. Computations and ray-tracing algorithm in this thesis were implemented using MATLAB. The impulse response, RMS delay spread SINR, outage probability and SNR were considered as the performance indicators of the system and were evaluated using the ray-tracing algorithm. We compared our simulation results with CDS and LSMS systems in previous studies. Good agreement was observed, giving confidence in the ability of our simulator to assess new novel optical wireless systems.

Previous work focused on improving the structure, mechanical or working mode of OWC APs. In this thesis, we focused on optimising the channel between the transmitter and the receiver. In Chapter 4, we reduced the influence of multipath dispersion and free space propagation loss by utilising relay terminals. We also reduced the outage

probability by utilising relay terminals that create more potential alternative links. We studied three different types of relay terminal (OEO, SOA and DF) for indoor OWC system and proposed a delay adaptation method for reducing the delay spread due to multiple relay terminals. These three types of relay terminals are applied in two different relay terminal deployment schemes (i.e., an AP in the centre of the ceiling and an AP in the centre of the communication floor). With SNR as a performance indicator, we compared three different types of relay terminals in the two scenarios while varying the number and location of relay terminals and considering various locations for the user. The results show that the DF relay terminal has better SNR performance in different scenarios compared with the other two types of relay terminals.

To optimise relay terminal deployment, in Chapter 5 we proposed ORTA to optimise the location and type of relay terminals (i.e., the deployment scheme) considering different numbers of relay terminals and considered three scenarios for the AP location which are the centre of the ceiling, the centre of the communication floor and a corner of the room. We developed a MILP model that we coded and compiled using A Mathematical Programming Language (AMPL) and solved using the CPLEX Optimiser. For the first scenario, where the AP is located at the centre of the ceiling. The best performance of ORTA is obtained with 2 relay terminals resulting in 19% and 9% improvement in downlink SNR and 127% and 86% improvement in uplink SNR compared to fixed deployments of relay terminals at 0.5m and 1.5m below the ceiling, respectively. For the second scenario where the optical AP is in the centre of the communication floor at the same level as the user, the results show that the best sum SNR uplink of ORTA using DF relay terminal is 54%, and 70% better than the fixed deployment of relay terminals at 0.5m, and 1.5m below the ceiling, respectively. For the third scenario where the optical AP is placed on the communication floor at the corner of the room, the best performance of ORTA is achieved when 4 relay terminals are active. By adjusting the variables and constraints of ORTA to deploy different numbers of relay terminals for downlink and uplink, the results show that the sum SNR is better compared to the case where the downlink and uplink go through same relay terminals by 3% and 5% for downlink and uplink, respectively.

In Chapter 6, a beam steering OWC multi-user system based on NOMA is introduced. The achievable rate and BER, as the performance indicator of proposed system, were investigated under different values of the power allocation factor α. The achievable rate of users degrades when the power allocation factor is increased while the BER fluctuates with the increase in the power allocation factor. The results show that a balance between the BER and the achievable rate can be achieved when $\alpha = 0.4$. We also proposed a cooperative communication mode with two phases based on O-E-O amplified-and-forward relay terminal to reduce the influence of the blockage and shadowing resulting from human movement in a beam steering OWC system. In the first phase, APs transmit the signal to relay terminals and the user. In the second phase, relay terminals forward the received signal to the user. The user combines the signals of two phases using MRC. The simulation results show that outage probability of the cooperative communication mode is two orders of magnitude lower on average than direct communication without relay terminals. The results show that the user that has links with more relay terminals observes higher robustness to human body blockage.

7.2 Potential areas of future work

The following is a list of proposed future areas of research that require further investigation:

1) In relay-based systems, there is a potential to reduce wastage in the time domain by studying coded diversity methods and network coding. By allocating different code sequences for downlink and uplink separately, it is possible to operate both the downlink and uplink in the same time phase. This approach enhances the bandwidth efficiency in the time domain by reducing wastage.
2) DF relay terminals can be studied in the context of multiuser OWC systems and compared with O-E-O amplified-and-forward relay terminals. In multiuser OWC systems, the superposition signal combines the signals from different users. In order to deploy the DF relay terminals to successfully decode and forward the signal to the intended user, a mechanism needs to be developed. This mechanism should enable the DF relay terminals to decode the received signal and efficiently forward it to the target user.

3) Reconfigurable Intelligent Surface (RIS) consists of a large number of passive reflecting elements, such as antennas or metamaterial elements, that are capable of altering the propagation of the wireless signals. The key idea behind RIS is to manipulate the wireless signal's amplitude, phase, and direction by adjusting the configuration of the reflecting elements. By intelligently controlling the reflection properties of the surface, RIS can enhance the signal strength, improve coverage, reduce interference, and enable secure and energy-efficient communication. RIS can be investigated in multiuser OWC system and compared with O-E-O amplified-and-forward relay terminals.
4) OFDM is a digital modulation technique widely used in modern wireless communication systems. It is a multi-carrier modulation scheme that divides the available bandwidth into multiple subcarriers and transmits data simultaneously on each subcarrier. By using many narrowband subcarriers, OFDM can efficiently utilize the available bandwidth and achieve a higher data rate compared to other modulation techniques. OFDM can be considered to improve the spectrum efficiency of multiuser OWC systems.
5) Currently, SLMs pre-store many phase patterns (Fresnel zone plates). However, the actual indoor environment may be more complex. Instead of predefined phase pattern, the phase pattern can be generated by Artificial Intelligence (AI) (e.g., Deep Neural Networks (DNN) or Reinforcement Learning (RL)). It can efficiently and instantly adjust the phase pattern of LSM while adopting to the real environment. Based on this method, a future area is to develop a real time user tracking algorithm for low and high speed users.
6) The huge size of current optical access points and user limit the application of OWC system. Integrating the optical transceiver, phase modulator and other optical devices on photon silicon chip is a potential idea to realize miniaturization of optical equipment. These chips serve as a promising solution to replace conventional transceivers in OWC systems, achieving more compact and efficient system-on-chip designs. The photon silicon chip has gained significant attention in both academia and industry as a light detection and ranging device. Its potential for integrating communication function makes it a promising candidate for achieving integrated sensing and communication in the 6G system.

Appendix A

The blocking area calculation for fixed location of transmitter and receiver

Considering a man (cylinder) with height H and diameter ϕ with horizontal movement on the floor only, the blocked areas of the link between the transmitter and the user can be defined as in Fig. A-1(a)(b)(c)

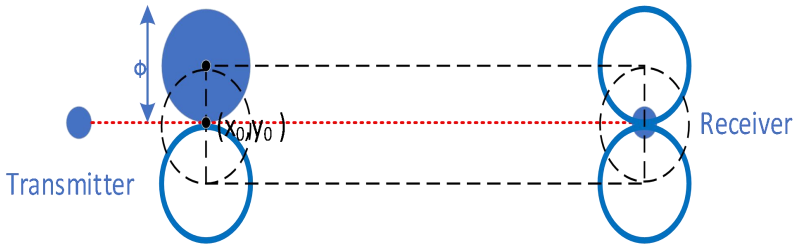

(a)

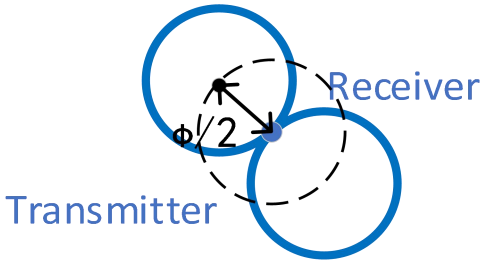

(b)

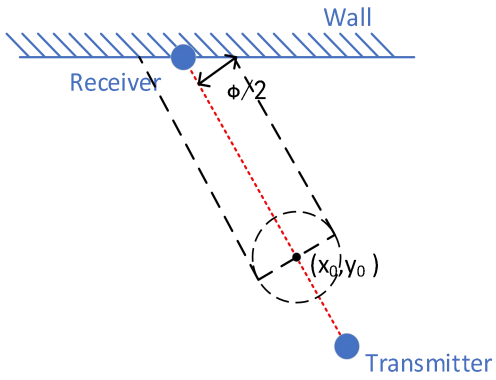

(c)

Figure A- 1 The block area of different scenarios.

The black dash line in Fig. A-1(a), (b), (c) is the area that the human blocks the link (red dash line) between transmitter (relay node) and user (relay node) if located in those locations. In Fig. A-1 (a), the location of transmitter and receiver are different, while the user is not at the edge of the room. In Fig. A-1 (b), the location of the transmitter and the receiver are the same on the communication plane. In Fig. A-1 (c), the location of transmitter and receiver are different, while the receiver is at the edge of the room.

While the receiver is not at the edge of the room and $(x_u \neq x_t, y_u \neq y_t)$, the location of receiver and transmitter in communication plane are different, the block area is shown as black dash line as above in Fig. A-1 (a). We can divide this area into 2 semicircles and a rectangle. For the area of the rectangle:

Let $y = kx + b$ represent the line that passes through $(x_t, y_t), (x_u, y_u)$

$$k = \frac{y_t - y_u}{x_t - x_u}, b = y_t - \frac{y_t - y_u}{x_t - x_u} x_t \tag{8-1}$$

where $(x_t, y_t, z_t), (x_u, y_u, z_u)$ are the locations of the transmitter and the user respectively in the room. Let (x_0, y_0) represents the centre of circle on the left of rectangle. We can get following equation:

$$(1+k^2)x_0^2 + (2\mathrm{k}(b-y_u) - 2x_u)x_0 + \mathrm{x}_u^2 + (b-y_u)^2 - D_1^2 = 0$$

$$a = (1+k^2),\ \mathrm{d} = 2\mathrm{k}(b-y_u) - 2x_u,\ c = \mathrm{x}_u^2 + (b-y_u)^2 - D_1^2 \tag{8-2}$$

$$x_0 = \frac{-d \pm \sqrt{d^2 - 4ac}}{2a}$$

where D_1 can be represented as:

$$D_1 = \frac{D_{tu}H}{z_t - z_u}$$

$$D_{tu} = \sqrt[2]{(x_u - x_t)^2 + (y_u - y_t)^2} \tag{8-3}$$

where H is the height of human. The distance between (x_0, y_0) and (x_t, y_t) should satisfy following equation:

$$\sqrt[2]{(x_0 - x_t)^2 + (y_0 - y_t)^2} = D_{tu} - D_1 \tag{8-4}$$

Based on equation (8-4), we can determine (x_0, y_0). Let $y = -\frac{1}{k}x + b_1\ and\ y = -\frac{1}{k}x + b_2$ represent the dash line which are perpendicular to $y = kx + b$ direct link pass points (x_0, y_0) and (x_u, y_u), then:

$$b_1 = \frac{1}{k}x_0 + y_0,\ b_2 = \frac{1}{k}x_u + y_u\ D_{tu} - D_1 \tag{8-5}$$

Let $y = kx + b_3 \; and \; y = kx + b_4$ represent the dash line which are parallel to the direct link. The distance from (x_0, y_0) to $y = kx + b_3$ equals to $\frac{\emptyset}{2}$ as following equation:

$$\frac{\emptyset}{2} = \frac{|kx_0 - y_0 + b_3|}{\sqrt{1 + k^2}} \tag{8-6}$$

where $\emptyset$ is diameter of human. We can get:

$$\begin{aligned} b_3 &= \sqrt{\frac{\emptyset^2}{4}(1 + k^2)} - (kx_0 - y_0)\,, \\ b_4 &= -\sqrt{\frac{\emptyset^2}{4}(1 + k^2)} - (kx_0 - y_0) \end{aligned} \tag{8-7}$$

The cumulative probability density function for rectangle area is defined as:

$$P_R = \iint_S f(x)f(y) = \int_S \frac{36}{x_m^3 y_m^3}\left(x^2 - \frac{x_m^2}{4}\right)\left(y^2 - \frac{y_m^2}{4}\right) \tag{8-8}$$

Let$u = \mathrm{y} - \mathrm{kx}$ and $v = \mathrm{y} + \frac{1}{k}x$, we can get $u_1 = b_3, u_2 = b_4, v_1 = b_1, v_2 = b_2$ as the range of double integration.

$$\begin{aligned} \frac{d(u,v)}{d(x,y)} &= \begin{vmatrix} \frac{du}{dx} & \frac{du}{dy} \\ \frac{dv}{d} & \frac{dv}{dy} \end{vmatrix} = \begin{vmatrix} -k & 1 \\ \frac{1}{k} & 1 \end{vmatrix} = -k - \frac{1}{k} = -\frac{k^2 + 1}{k} \\ \left|\frac{d(x,y)}{d(u,v)}\right| &= \left|\left(\frac{d(u,v)}{d(x,y)}\right)^{-1}\right| = \left|-\frac{k}{k^2 + 1}\right| \end{aligned} \tag{8-9}$$

We can get $x(u,v)=\frac{v-u}{k+\frac{1}{k}}$ and $y(u,v)=\frac{u+k^2v}{1+k^2}$. The probability function for rectangle area is given as:

$$P_R=\iint \frac{36}{x_m^3y_m^3}\left(\left(x(u,v)\right)^2-\frac{x_m^2}{4}\right)\left(\left(y(u,v)\right)^2-\frac{y_m^2}{4}\right)\left|\frac{d(x,y)}{d(u,v)}\right|du\,dv \tag{8-10}$$

$$=\iint \frac{36}{x_m^3y_m^3}\left(\left(\frac{v-u}{k+\frac{1}{k}}\right)^2-\frac{x_m^2}{4}\right)\left(\left(\frac{u+k^2v}{1+k^2}\right)^2-\frac{y_m^2}{4}\right)\left|-\frac{k}{k^2+1}\right|du\,dv$$

For the area of half circle (x_0,y_0) on the left of rectangle, let $x-x_0=rcos\theta, y-y_0=r\sin\theta$

$$\left|\frac{d(x,y)}{d(r,\theta)}\right|=\begin{vmatrix}\frac{dx}{dr} & \frac{dx}{d\theta}\\ \frac{dy}{dr} & \frac{dy}{d\theta}\end{vmatrix}=\begin{vmatrix}\cos\theta & -r\sin\theta\\ \sin\theta & r\cos\theta\end{vmatrix}=\left|r(\cos\theta)^2+r(\sin\theta)^2\right|=r \tag{8-11}$$

If $-\frac{1}{k}>0, \theta_1=\tan^{-1}\left(-\frac{1}{k}\right)$, the direction vector $\vec{L}$ of $y=-\frac{1}{k}x+b_1$ is $(1,-\frac{1}{k})$. If $-\frac{1}{k}<0, \theta_1=\tan^{-1}\left(-\frac{1}{k}\right)+\frac{\pi}{2}$, the direction vector $\vec{L}$ of $y=-\frac{1}{k}x+b_1$ is $(-1,-\frac{1}{k})$. The direction vector $\overrightarrow{C_0}$ of (x_0,y_0) is defined as (x_0-x_u,y_0-y_u). If $\vec{L}\times\overrightarrow{C_0}>0$, $\overrightarrow{C_0}$ is rotating on the anti-clockwise direction of $\vec{L}$. The boundaries of the half circle(x_0,y_0) are $0\le r\le\frac{\Phi}{2}, \theta_1\le\theta\le\theta_1+\pi$. If $\vec{L}\times\overrightarrow{C_0}<0$, $\overrightarrow{C_0}$ is rotating on the clockwise direction of $\vec{L}$. The boundaries of the half circle(x_0,y_0) are $0\le r\le\frac{\Phi}{2}, \theta_1-\pi\le\theta\le\theta_1$. The probability of the area of the half circle(x_0,y_0) is defined as:

$$P_{R0} = \iint_S f(r)f(\theta)$$

$$= \iint \frac{36}{x_m^3 y_m^3}\left(\left(x(r,\theta)\right)^2 - \frac{x_m^2}{4}\right)\left(\left(y(r,\theta)\right)^2 - \frac{y_m^2}{4}\right)\left|\frac{d(x,y)}{d(r,\theta)}\right| \boldsymbol{dr\, d\theta} \qquad (8\text{-}12)$$

$$= \iint \frac{36}{x_m^3 y_m^3}\left((x_0 + r\cos\theta)^2 - \frac{x_m^2}{4}\right)\left((y_0 + r\sin\theta)^2 - \frac{y_m^2}{4}\right) r\, \boldsymbol{dr\, d\theta}$$

For the half circle (x_u, y_u) on the right side of rectangle. Let $x - x_u = rcos\theta, y - y_u = r\sin\theta$. The direction vector $\overrightarrow{C_u}$ of (x_u, y_u) is defined as $(x_u - x_0, y_u - y_0)$. If $\vec{L} \times \overrightarrow{C_u} > 0$, $\overrightarrow{C_u}$ is rotating on the anti-clockwise direction of $\vec{L}$. The boundaries of the half circle(x_u, y_u) are $0 \le r \le \frac{\Phi}{2}, \theta_1 \le \theta \le \theta_1 + \pi$. If $\vec{L} \times \overrightarrow{C_u} < 0$,$\overrightarrow{C_u}$ is rotating on the clockwise direction of $\vec{L}$. The boundaries of the half circle (x_u, y_u) are $0 \le\le \frac{\Phi}{2}, \theta_1 - \pi \le \theta \le \theta_1$. The probability of the area of the half circle(x_u, y_u) is defined as:

$$P_{Ru} = \iint_S f(r)f(\theta)$$

$$= \iint \frac{36}{x_m^3 y_m^3}\left(\left(x(r,\theta)\right)^2 - \frac{x_m^2}{4}\right)\left(\left(y(r,\theta)\right)^2 - \frac{y_m^2}{4}\right)\left|\frac{d(x,y)}{d(r,\theta)}\right| \boldsymbol{dr\, d\theta} \qquad (8\text{-}13)$$

$$= \iint \frac{36}{x_m^3 y_m^3}\left((x_u + r\cos\theta)^2 - \frac{x_m^2}{4}\right)\left((y_u + r\sin\theta)^2 - \frac{y_m^2}{4}\right) r\, \boldsymbol{dr\, d\theta}$$

Then we can get the blocking probability of the entire area in Fig. A-1(a) as:

$$P_B = P_R + P_{R0} + P_{Ru} \qquad (8\text{-}14)$$

When $(x_u \neq x_t, y_u = y_t)$, the black area is shown as black dash line as Fig. A-1(a) and parallel to x axis. Let (x_0, y_0) represent the centre of circle on the left of the rectangle.

$$y_0 = y_u, x_0 = x_u + \frac{H}{Z} * (x_t - x_u) \tag{8-15}$$

If $x_0 \leq x_u$, the boundaries of P_R are $x_0 \leq x \leq x_u \; and \; y_0 - \frac{\Phi}{2} \leq y \leq y_0 + \frac{\Phi}{2}$, else the boundaries of P_R are $x_u \leq x \leq x_0 \; and \; y_0 - \frac{\Phi}{2} \leq y \leq y_0 + \frac{\Phi}{2}$. For the half circle (x_0, y_0), the direction vector $\overrightarrow{C}$ of (x_0, y_0) is defined as $(x_0 - x_u, y_0 - y_u)$. Let $x - x_0 = rcos\theta, y - y_0 = r\sin\theta$

If $(0,1) \times \overrightarrow{C_o} > 0$, $\overrightarrow{C_o}$ is rotating on the anti-clockwise direction of $(0,1)$. The boundaries of the P_{R0} are $0 \leq r \leq \frac{\Phi}{2}, \frac{\pi}{2} \leq \theta \leq \frac{\pi}{2} + \pi$. If $(0,1) \times \overrightarrow{C_o} < 0$, $\overrightarrow{C_o}$ is rotating on the clockwise direction of $(0,1)$. The boundaries of the P_{R0} are $0 \leq r \leq \frac{\Phi}{2}, \frac{\pi}{2} - \pi \leq \theta \leq \frac{\pi}{2}$. P_{R0} can be calculated based on equation (8-12) and the above boundaries. Similarly, we can get the boundaries of P_{Ru}, (x_u, y_u) represented as $0 \leq r \leq \frac{\Phi}{2}, \frac{\pi}{2} \leq \theta \leq \frac{\pi}{2} + \pi$ or $0 \leq r \leq \frac{\Phi}{2}, \frac{\pi}{2} - \pi \leq \theta \leq \frac{\pi}{2}$. P_{Ru} can be calculated based on equation (8-13). The direction of vector $\overrightarrow{C_u}$ of P_{Ru} is on the contrary of $\overrightarrow{C_o}$. Then we can get the block probability of entire area.

When $(x_u = x_t, y_u \neq y_t)$, the black area is shown as black dash line as above Fig 8-1(a) and parallel to y axis. let (x_0, y_0) represents the centre of circle on the left of rectangle.

$$x_0 = x_u, y_0 = y_u + \frac{H}{Z} * (y_t - y_u) \tag{8-16}$$

The probability function for rectangle area is defined as equation (8-10). If $y_0 \le y_u$, the boundaries of P_R are $y_0 \le y \le y_u \; and \; x_0 - \frac{\Phi}{2} \le x \le x_0 + \frac{\Phi}{2}$, else $y_u \le y \le y_0 \; and \; x_0 - \frac{\Phi}{2} \le x \le x_0 + \frac{\Phi}{2}$. For the half circle (x_0, y_0), the direction vector $\overrightarrow{C}$ of (x_0, y_0) is defined as $(x_0 - x_u, y_0 - y_u)$. Let $x - x_0 = rcos\theta, y - y_0 = r\sin\theta$, $\left|\frac{d(x,y)}{d(r,\theta)}\right| = r$. If $(0,1) \times \vec{C} > 0$, $\vec{C}$ is rotating on the anti-clockwise direction of $(0,1)$. The boundaries of $P_{R0}(x_0, y_0)$ are $0 \le r \le \frac{\Phi}{2}, 0 \le \theta \le \pi$. If $(0,1) \times \vec{C} < 0$, $\vec{C}$ is rotating on the clockwise direction of $(0,1)$. The boundaries of $P_{R0}(x_0, y_0)$ are $0 \le r \le \frac{\Phi}{2}, -\pi \le \theta \le 0$. Similarly, we can get the boundaries P_{Ru} of the half circle of (x_u, y_u) are $0 \le r \le \frac{\Phi}{2}, 0 \le \theta \le \pi$ or $0 \le r \le \frac{\Phi}{2}, -\pi \le \theta \le 0$. P_{Ru} can be calculated based on equation (8-13). The direction of vector $\overrightarrow{C_u}$ of P_{Ru} is on the contrary of $\overrightarrow{C_o}$.Then we can get the block probability of entire area.

When $(x_u = x_t, y_u = y_t)$ the location of receiver and transmitter in communication plane are the same as Fig. A-1(b). The black area is a circle. Let $x - x_0 = rcos\theta, \; y - y_0 = r\sin\theta$, $\left|\frac{d(x,y)}{d(r,\theta)}\right| = r$. Then we can get the blocking probability of entire area:

$$P_B = \iint \frac{36}{x_m^3 y_m^3}\left(\left(x(r,\theta)\right)^2 - \frac{x_m^2}{4}\right)\left(\left(y(r,\theta)\right)^2 - \frac{y_m^2}{4}\right)\left|\frac{d(x,y)}{d(r,\theta)}\right| dr\, d\theta$$

$$= \int_0^{\frac{\phi}{2}} \int_0^{2\pi} \frac{36}{x_m^3 y_m^3}\left((x_0 + r\cos\theta)^2 - \frac{x_m^2}{4}\right)\left((y_0 + r\sin\theta)^2 - \frac{y_m^2}{4}\right) r\, dr\, d\theta \tag{8-17}$$

if the receiver is located at edge of the room, $(x_u \ne x_t, y_u \ne y_t)$ and the location of receiver and transmitter in communication plane are different. k, b_1, b_2, b_3, b_4 can be obtained from Equations (8-1), (8-2) and (8-3). When receiver at the wall on x axis ($x_u = -\frac{x_m}{2} or \frac{x_m}{2}$), Let $u = \mathrm{y} - \mathrm{kx}$ and $v = \mathrm{y} + \frac{1}{k}x$, we can get $u_1 = b_3, u_2 = b_4, v_1 = b_1, v_2 = x_u\left(k + \frac{1}{k}\right) + u$ as the range of right-angled trapezoid in Fig. A-1(c). When receiver at the wall on Y axis ($y_u = -\frac{y_m}{2} or \frac{y_m}{2}$), Let $u = \mathrm{y} - \mathrm{kx}$ and $v = \mathrm{y} + \frac{1}{k}x$, we

can get $u_1 = b_3, u_2 = b_4, v_1 = b_1, v_2 = \frac{y_u(1+k^2)-u}{k^2}$ as the range of right-angled trapezoid in Fig. A-1 (c). The cumulative probability density equation of right-angled trapezoid in Fig. A-1 (c) is same as (8-9). We can get the probability P_C. The probability P_{R0} of half circle of (x_0, y_0) can be obtained based on equation (8-13). The probability P_B of entire area of black dash line in Fig. A-1 (c) is defined as:

$$P_B = P_C + P_{R0} \tag{8-18}$$

References

1. T. Coonan, "Indoor Optical Wireless Systems: Technology, Trends, and Applications", Journal of Lightwave Technology, vol. 36, no. 8, pp. 1459-1467, 2018. Available: 10.1109/jlt.2017.2787614.

2. C. Mobile, Cisco Visual Networking Index: Cisco Annual Internet Report (2018 – 2023) White Paper. 2020.

3. A. Gupta and R. Jha, "A Survey of 5G Network: Architecture and Emerging Technologies", IEEE Access, vol. 3, pp. 1206-1232, 2015.

4. W. Chin, Z. Fan and R. Haines, "Emerging technologies and research challenges for 5G wireless networks", IEEE Wireless Communications, vol. 21, no. 2, pp. 106-112, 2014.

5. EPSRC, "Terabit Bidirectional Multi-user Optical Wireless System (TOWS)for6G."[Online].Available:https://gow.epsrc.ukri.org/NGBOViewGrant.aspx?GrantRef=EP/S016570/1. [Accessed: 20-Dec-2018].

6. EPSRC, "Super Receivers for Visible Light Communications." [Online]. Available:https://gow.epsrc.ukri.org/NGBOViewGrant.aspx?GrantRef=EP/R00689X/1. [Accessed: 20-Dec-2018].

7. EPSRC, "Multifunctional Polymer Light-Emitting Diodes with Visible Light Communications(MARVEL)."[Online].Available:https://gow.epsrc.ukri.org/NGBOViewGrant.aspx?GrantRef=EP/P006280/1. [Accessed: 20-Dec-2018].

8. R. Yuan and J. Ma, "Review of ultraviolet non-line-of-sight communication", China Communications, vol. 13, no. 6, pp. 63-75, 2016. Available: 10.1109/cc.2016.7513203.

9. H. Haas, L. Yin, Y. Wang, and C. Chen, "What is Lifi?," Journal of Lightwave Technology, vol. 34, no. 6, pp. 1533–1544, 2016. doi:10.1109/jlt.2015.2510021

10. A. G. Al-Ghamdi and M. H. Elmirghani, “Optimization of a triangular PFDR antenna in a fully diffuse OW system influenced by background noise and multipath propagation,” IEEE Trans. Commun., vol. 51, no. 12, pp. 2103–2114, 2003.

11. A. G. Al-Ghamdi and J. M. H. Elmirghani, “Line Strip Spot-Diffusing Transmitter Configuration for Optical Wireless Systems Influenced by Background Noise and Multipath Dispersion,” IEEE Trans. Commun., vol. 52, no. 1, pp. 37–45, 2004.

12. F. E. Alsaadi, M. A. Alhartomi, and J. M. H. Elmirghani, “Fast and efficient adaptation algorithms for multi-gigabit wireless infrared systems,” J. Light. Technol., vol. 31, no. 23, pp. 3735–3751, 2013.

13. F. E. Alsaadi and J. M. H. Elmirghani, “Mobile Multigigabit Indoor Optical Wireless Systems Employing Multibeam Power Adaptation and Imaging Diversity Receivers,” J. Opt. Commun. Netw., vol. 3, no. 1, p. 27, 2011.

14. A. G. Al-Ghamdi and J. M. H. Elmirghani, “Analysis of diffuse optical wireless channels employing spot-diffusing techniques, diversity receivers, and combining schemes,” IEEE Trans. Commun., vol. 52, no. 10, pp. 1622–1631, 2004.

15. A. G. Al-Ghamdi and J. M. H. Elmirghani, “Performance analysis of mobile optical wireless systems employing a novel beam clustering method and diversity detection,” IEE Proc. Optoelectron., vol. 151, no. 4, pp. 223–231, 2004.

16. F. E. Alsaadi and J. M. H. Elmirghani, “Beam power and angle adaptation in multibeam 2.5 Gbit/s spot diffusing mobile optical wireless system,” IEEE J. Sel. Areas Commun., vol. 28, no. 6, pp. 913–927, 2010.

17. F. E. Alsaadi and J. M. H. Elmirghani, “Adaptive mobile line strip multibeam MC-CDMA optical wireless system employing imaging detection in a real indoor environment,” IEEE J. Sel. Areas Commun., vol. 27, no. 9, pp. 1663–1675, 2009.

18. F. E. Alsaadi and J. M. H. Elmirghani, “High-speed spot diffusing mobile optical wireless system employing beam angle and power adaptation and imaging receivers,” J. Light. Technol., vol. 28, no. 16, pp. 2191–2206, 2010.

19. F. E. Alsaadi and J. M. H. Elmirghani, “Performance evaluation of 2.5 Gbit/s and 5 Gbit/s optical wireless systems employing a two dimensional adaptive beam clustering method and imaging diversity detection,” IEEE J. Sel. Areas Commun., vol. 27, no. 8, pp. 1507–1519, 2009.

20. M. T. Alresheedi and J. M. H. Elmirghani, “10 Gb/s indoor optical wireless systems employing beam delay, power, and angle adaptation methods with imaging detection,” J. Light. Technol., vol. 30, no. 12, pp. 1843–1856, 2012

21. M. T. Alresheedi and J. M. H. Elmirghani, “Performance evaluation of 5 Gbit/s and 10 Gbit/s mobile optical wireless systems employing beam angle and power adaptation with diversity receivers,” IEEE J. Sel. Areas Commun., vol. 29, no. 6, pp. 1328–1340, 2011.

22. Osama Alsulami, Ahmed Taha Hussein, Mohammed T. Alresheedi and Jaafar M. H. Elmirghani, “Optical Wireless Communication Systems, A Survey.”[Online].Available:https://www.researchgate.net/publication/329999968

23. K. L. Sterckx, J. M. H. Elmirghani, and R. A. Cryan, “Pyramidal fly-eye detection antenna for optical wireless systems,” Opt. Wirel. Commun. (Ref. No. 1999/128), IEE Colloq., no. i, p. 5/1-5/6, 1999.

24. Z. Ghassemlooy, W. Popoola, and S. Rajbhandari, Optical Wireless Communications: System and Channel Modelling Press, 2012.

25. J. M. Kahn and J. R. Barry, “Wireless infrared communications,” Proceedings of the IEEE, vol. 85, no. 2, pp. 265-298, Feb. 1997.

26. K. Yiannopoulos, N. Sagias and A. Boucouvalas, "On the Performance of Semiconductor Optical Amplifier-Assisted Outdoor Optical Wireless Links", IEEE

Journal on Selected Areas in Communications, vol. 33, no. 9, pp. 1869-1876, 2015. Available: 10.1109/jsac.2015.2433052.

27. M. ElMossallamy, H. Zhang, L. Song, K. Seddik, Z. Han and G. Li, "Reconfigurable Intelligent Surfaces for Wireless Communications: Principles, Challenges, and Opportunities", IEEE Transactions on Cognitive Communications and Networking, vol. 6, no. 3, pp. 990-1002, 2020. Available: 10.1109/tccn.2020.2992604.

28. C. Singh, J. John, Y. Singh, and K. Tripathi, “A Review on Indoor Optical Wireless Systems,” IETE Technical review, vol. 19, pp. 3-18, 2002.

29. J. Senior, Optical Fiber Communications: Principles and practice. Prentice-Hall, 2013.

30. A. A. Bergh and J. A. Copeland, “Optical sources for fiber transmission systems,” Proceedings of the IEEE, vol. 68, no. 10, pp. 1240–1247, 1980.

31. R. J. Green, H. Joshi, M. D. Higgins, and M. S. Leeson, “Recent Developments in Indoor Optical Wireless,” Communications, IET, vol. 2, no. 1, pp. 3–10, Jan. 2008.

32. A. T. Hussein, M. T. Alresheedi, and J. M. H. Elmirghani, “Fast and Efficient Adaptation Techniques for Visible Light Communication Systems,” J. Opt. Commun. Netw., vol. 8, no. 6, pp. 382–397, 2016.

33. A. T. Hussein, M. T. Alresheedi, and J. M. H. Elmirghani, “20 Gb/s Mobile Indoor Visible Light Communication System Employing Beam Steering and Computer Generated Holograms,” J. Light. Technol., vol. 33, no. 24, pp. 5242–5260, 2015.

34. A. T. Hussein, M. T. Alresheedi, and J. M. H. Elmirghani, “25 Gbps mobile visible light communication system employing fast adaptation techniques,” in International Conference on Transparent Optical Networks, 2016, vol. 2016–Augus.

35. Žukauskas Artūras, M. S. Shur, and R. Gaska, Introduction to solid-state lighting. New York: Wiley, 2002.

36. G. Cossu, a M. Khalid, P. Choudhury, R. Corsini, and E. Ciaramella, “3.4 Gbit/s visible optical wireless transmission based on RGB LED.,” Opt. Express, vol. 20, no. 26, pp. B501-6, 2012.
37. A. M. Khalid, G. Cossu, R. Corsini, P. Choudhury, and E. Ciaramella, “1-Gb/s transmission over a phosphorescent white LED by using rate-adaptive discrete multitone modulation,” IEEE Photonics J., vol. 4, no. 5, pp. 1465–1473, 2012.
38. R. Yuan and J. Ma, "Review of ultraviolet non-line-of-sight communication", China Communications, vol. 13, no. 6, pp. 63-75, 2016. Available: 10.1109/cc.2016.7513203
39. W. Chin, Z. Fan and R. Haines, "Emerging technologies and research challenges for 5G wireless networks", IEEE Wireless Communications, vol. 21, no. 2, pp. 106-112, 2014
40. A. Hussein and J. Elmirghani, "10 Gbps Mobile Visible Light Communication System Employing Angle Diversity, Imaging Receivers, and Relay Nodes", Journal of Optical Communications and Networking, vol. 7, no. 8, p. 718, 2015
41. A. Neumann, J. J. Wierer, W. Davis, Y. Ohno, S. R. J. Brueck, and J. Y. Tsao, “Four-color laser white illuminant demonstrating high color-rendering quality,” Opt. Express, vol. 19, no. S4, p. A982, 2011.
42. K. Wang, A. Nirmalathas, C. Lim, and E. Skafidas, “High speed duplex optical wireless communication system for indoor personal area networks,” Optics Express, vol. 18, no. 24, pp. 25199–25216, Nov. 2010.
43. T. Ozugur, J. A. Copeland, M. Naghshineh, and P. Kermani, “Next-generation indoor infrared LANs: issues and approaches,” Personal Communications, IEEE, vol. 6, pp. 6-19, 1999.
44. M. T. Alresheedi, "Adaptation Techniques in Optical Wireless Communications.",[Online].Available:http://etheses.whiterose.ac.uk/6396/1/Final_Thesis_2013.pdf

45. J. Barry, J. Kahn, W. Krause, E. Lee and D. Messerschmitt, "Simulation of multipath impulse response for indoor wireless optical channels", IEEE Journal on Selected Areas in Communications, vol. 11, no. 3, pp. 367-379, 1993. Available: 10.1109/49.219552.

46. L. Zeng, D. C. O'Brien, H. Le-Minh, G. E. Faulkner, K. Lee, D. Jung, Y. Oh, and E.T. Won, "High data rate multiple input multiple output (MIMO) optical wireless communications using white LED lighting," Selected Areas in Communications, IEEE Journal on, vol. 27, pp. 1654-1662, 2009.

47. J. P. Savicki, and S. P. Morgan, "Hemispherical concentrators and spectral filters for planar sensors in diffuse radiation fields," Applied Optics, vol. 33, pp. 8057-8061, 1994.

48. R. Ramirez-Iniguez, S. M. Idrus, and Z. Sun, Optical wireless communications: IR for wireless connectivity: CRC Press, 2008.

49. K. P. Ho and J. M. Kahn, "Compound parabolic concentrators for narrow-band wireless infrared receivers," Optical Engineering, vol. 34, pp. 1385–1395, May 1995.

50. T. Chen, L. Liu, B. Tu, Z. Zheng and W. Hu, "High-Spatial-Diversity Imaging Receiver Using Fisheye Lens for Indoor MIMO VLCs", IEEE Photonics Technology Letters, vol. 26, no. 22, pp. 2260-2263, 2014. Available: 10.1109/lpt.2014.2354458.

51. A. H. Azhar, T. Tran, and D. O'Brien, "A gigabit/s indoor wireless transmission using MIMO-OFDM visible-light communications," IEEE Photon. Technol. Lett., vol. 25, no. 2, pp. 171–174, Jan. 15, 2013.

52. T. Q. Wang, Y. A. Sekercioglu, and J. Armstrong, "Analysis of an optical wireless receiver using a hemispherical lens with application in MIMO visible light communications," J. Lightw. Technol., vol. 31, no. 11, pp. 1744–1754, Jun. 1, 2013.

53. K. Miyamoto, “Fish eye lens,” J. Opt. Soc. Amer., vol. 54, no. 8, pp. 1060–1061, Aug. 1964.

54. S. H. Younus and J. M. H. Elmirghani, “WDM for high-speed indoor visible light communication system,” in International Conference on Transparent Optical Networks, 2017, pp. 1–6.

55. I. Din and H. Kim,” Performance analysis of SC-L-PPM for energy-efficient visible light communication,” in The 18th IEEE International Symposium on Consumer Electronics ,2014.

56. M. J. McCullagh and D. R. Wisely, “155 Mbit/s optical wireless link using a bootstrapped silicon APD receiver,” Electronics Letters, vol. 30, no. 5, pp. 430–432,1994.

57. Z. Ghassemlooy, W. Popoola, and S. Rajbhandari, Optical Wireless Communications: System and Channel Modelling Press, 2012.

58. J. R. Barry, J. M. Kahn, E. A. Lee, and D. G. Messerschmitt, “High-speed nondirective optical communication for wireless networks,” IEEE Netw., vol. 5, no. 6, pp. 44–54, 1991

59. A. Al-Ghamdi and J. Elmirghani, "Optimization of a pyramidal fly-eye diversity receiver for optical wireless systems under the influence of multipath dispersion and background noise", Microwave and Optical Technology Letters, vol. 36, no. 5, pp. 401-406, 2003. Available: 10.1002/mop.10776.

60. J.R. Barry, J.M. Kahn, W.J. Krause, E.A. Lee, and D.G. Messerschmit, Simulation of multipath impulse response for indoor wireless optical channels, IEEE J Select Areas Commun 11 (1993), 367–379

61. F. Alsaadi and J. Elmirghani, "Spot diffusing angle diversity MC-CDMA optical wireless system", IET Optoelectronics, vol. 3, no. 3, pp. 131-141, 2009. Available: 10.1049/iet-opt.2007.0059.

62. P. Djahani and J. Kahn, "Analysis of infrared wireless links employing multibeam transmitters and imaging diversity receivers", IEEE Transactions on Communications, vol. 48, no. 12, pp. 2077-2088, 2000. Available: 10.1109/26.891218.

63. IEEE Std. 802.15.7-2011, Part 15.7:Short-Range Wireless Optical Communication Using Visible Light, Sep.2011.

64. K. K. Wong, T. O'Farrell and M. Kiatweerasakul, "The performance of optical wireless OOK, 2-PPM and spread spectrum under the effects of multipath dispersion and artificial light interference," International Journal of Communication Systems, vol. 13, no. 7 & 8, pp. 551-576, November-December 2000.

65. R. J. Green, H. Joshi, M. D. Higgins, and M. S. Leeson, "Recent Developments in Indoor Optical Wireless," Communications, IET, vol. 2, no. 1, pp. 3–10, Jan. 2008.

66. J. B. Carruthers and J. M. Kahn, "Multiple-subcarrier modulation for nondirected Wireless Infrared Communication," IEEE Journal on Selected Areas in Communications, vol. 14, no. 3, pp. 538–546, 1996.

67. Z. Ghassemlooy, V. R. Wickramasinghe, and L. Chao, "Optical fibre transmission of a broadband subcarrier multiplexed signal using PTM Techniques," IEEE Transactions on Consumer Electronics, vol. 42, no. 2, pp. 229–238, 1996.

68. O. Gonzalez, R. Perez-Jimenez, S. Rodriguez, J. Rabadan, and A. Ayala, "OFDM over Indoor Wireless Optical Channel," IEE Proceedings - Optoelectronics, vol. 152, no. 4, p. 199, 2005.

69. " The spectral sensitivity characteristics simulation of the silicon p-I ..." [Online].Available:https://www.researchgate.net/publication/298712994_The_spectral_sensitivity_characteristics_simulation_of_the_silicon_p-i-n structure_with_high_resistance_wells/fulltext/57aacd5e08ae0932c96fcd16/The-spectral-sensitivity-characteristics-simulation-of-the-silicon-p-i-n-structure-with-high-resistance-wells.pdf. [Accessed: 06-Dec-2022].

70. “ Firelight led source: Toward a balanced approach to the performance of ...” [Online].Available:https://www.researchgate.net/publication/262056081_Firelight_LED_Source_Toward_a_Balanced_Approach_to_the_Performance_of_Solid-State_Lighting_for_Outdoor_Environments. [Accessed: 06-Dec-2022].

71. C. W. Oh, E. Tangdiongga, and A. M. J. Koonen, “42.8 Gbit/s indoor optical wireless communication with 2-dimensional optical beamsteering,” in Proc. Opt. Fiber Commun. Conf. Exhib. 2015, Los Angeles, CA, USA, Paper no. M2F.3.

72. L. Dai, B.Wang, Y. Yuan, S. Han, C.-L. I, and Z.Wang, “Non-orthogonal multiple access for 5G: Solutions, challenges, opportunities, and future research trends,” IEEE Commun. Mag., vol. 53, no. 9, pp. 74–81, Sep. 2015.

73. L. Yin, X. Wu, and H. Haas, “On the performance of non-orthogonal multiple access in visible light communication,” in Proc. IEEE 26th Annu. Symp. Personal, Indoor Mobile Radio Commun., Hong Kong, Sep. 2015, pp. 1376–1381.

74. N. Lanenan, “Cooperative Diversity in Wireless Networks: Algorithms and Architectures,” Ph.D. dissertation, Massachusetts Institute of Technology, Cambridge, MA, Aug. 2002.

75. M. Yu and J. Li, “Is amplify-and-forward practically better than decodeand-forward or vice versa?” in Proc. IEEE Int. Conf. Acoustics, Speech, and Signal Processing (ICASSP), vol. 3, March 2005, pp. 365–368.

76. K. Van Acoleyen, W. Bogaerts and R. Baets, "Two-Dimensional Dispersive Off-Chip Beam Scanner Fabricated on Silicon-On-Insulator", IEEE Photonics Technology Letters, vol. 23, no. 17, pp. 1270-1272, 2011. Available: 10.1109/lpt.2011.2159785.

77. A. Gomez et al., "Beyond 100-Gb/s Indoor Wide Field-of-View Optical Wireless Communications", IEEE Photonics Technology Letters, vol. 27, no. 4, pp. 367-370, 2015. Available: 10.1109/lpt.2014.2374995.

78. S. Jo, H. Oh, Y. Lee, T. Le and B. An, "LED-to-LED Two Way Visible Light Communication System", Journal of the Institute of Electronics and Information Engineers, vol. 53, no. 1, pp. 79-85, 2016. Available: 10.5573/ieie.2016.53.1.079.

79. O. Z. Alsulami et al., “Optimum resource allocation in optical wireless systems with energy efficient fog and cloud architectures,” Philosophical Transactions of the Royal Society A Mathematics, Physics, Engineering and Science, vol. 378, No. 2169, pp. 1-11, March 2020.

80. Y. Zeng, S. H. Mohamed, T. E. H. El-Gorashi and J. M. H. Elmirghani, "Delay Adaptation Method for Relay Assisted Optical Wireless Systems," 2020 22nd International Conference on Transparent Optical Networks (ICTON), 2020, pp. 1-6, doi: 10.1109/ICTON51198.2020.9203126.

81. J. Beysens, Q. Wang, and S. Pollin, “Improving blockage robustness in VLC networks,” in Proc. 11th Int. Conf. Commun. Syst. Netw. (COMSNETS), Jan. 2019.

82. B. Guzman, A. Serrano and V. Gil Jimenez, "Cooperative optical wireless transmission for improving performance in indoor scenarios for visible light communications", IEEE Transactions on Consumer Electronics, vol. 61, no. 4, pp. 393-401, 2015. Available: 10.1109/tce.2015.7389772.

83. Guzmán, B.G.; Dowhuszko, A.A.; Gil Jiménez, V.P.; Pérez-Neira, A.I. Cooperative transmission scheme to address random orientation and blockage events in VLC systems. In Proceedings of the International Symposium on Wireless Communication Systems (ISWCS), Oulu, Finland, 27–30 August 2019; pp. 351–355.

84. A. Singh, G. Ghatak, A. Srivastava, V. Bohara and A. Jagadeesan, "Performance Analysis of Indoor Communication System Using Off-the-Shelf LEDs With Human Blockages", IEEE Open Journal of the Communications Society, vol. 2, pp. 187-198, 2021. Available: 10.1109/ojcoms.2020.3048954.

85. M. A. Dastgheib, H. Beyranvand, and J. A. Salehi, “Optimal visible light communication access point placement under stationary distribution of users’ mobility,” in Proc. 9th Int. Symp. Telecommun. (IST), Dec. 2018, pp. 96–101.

86. X. Nan, P. Wang, L. Guo, L. Huang and Z. Liu, "A Novel VLC Channel Model Based on Beam Steering Considering the Impact of Obstacle", IEEE Communications Letters, vol. 23, no. 6, pp. 1003-1007, 2019. Available: 10.1109/lcomm.2019.2908155.

87. F. R. Gfeller, and U. Bapst, “Wireless in-house data communication via diffuse infrared radiation,” Proceedings of the IEEE, vol. 67, pp. 1474-1486, 1979.

88. L. Niu, D. Wang, T. Jiang, S. Wu, A. Li and J. Song, "High fill-factor multilevel Fresnel zone plate arrays by femtosecond laser direct writing", Optics Communications, vol. 284, no. 3, pp. 777-781, 2011. Available: 10.1016/j.optcom.2010.09.066.

89. J. R. Barry, J. M. Kahn, W. J. Krause, E. A. Lee, and D. G. Messerschmitt, “ Simulation of Multipath Impulse Response for Wireless Optical Channels,”Selected Areas in Communications, IEEE Journal on, vol. 11, no. 3, April 1993, pp.367-379.

90. W. O. Popoola, Z. Ghassemlooy, J. I. H. Allen, E. Leitgeb, and S. Gao, “Freespace optical communication employing subcarrier modulation and spatial diversity in atmospheric turbulence channel,” Optoelectronics, IET, vol. 2, pp. 16-23, 2008

91. S. Jivkova and M. Kavehrad, “Indoor wireless infrared local access, multi-spot diffusing with computer generated holographic beam-splitters,” in Communications,1999. ICC '99. 1999 IEEE International Conference on, 1999, vol.1, pp. 604-608.

92. S. Jivkova, and M. Kavehard, “Multispot diffusing configuration for wireless infrared access,’’ Communications, IEEE Transactions on, vol. 48, pp. 970-978, 2000.

93. J. R. Barry, Wireless Infrared Communications. Boston: Kluwer, 1994.

94. A. C. Boucouvalas, “Indoor ambient light noise and its effect on wireless optical links,” Optoelectronics, IEE Proceedings-, vol. 143, pp. 334-338, 1996.

95. Z. Cui, P. Yue, and Y. Ji, ‘‘Study of cooperative diversity scheme based on visible light communication in VANETs,’’ in Proc. Int. Conf. Comput., Inf. Telecommun. Syst. (CITS), Kunming, China, Jul. 2016, pp. 1–5.

96. F. Alsaadi, M. Nikkar and J. Elmirghani, "Adaptive mobile optical wireless systems employing a beam clustering method, diversity detection, and relay nodes", IEEE Transactions on Communications, vol. 58, no. 3, pp. 869-879, 2010. Available: 10.1109/tcomm.2010.03.080361.

97. P. Pešek, S. Zvanovec, P. Chvojka, M. Bhatnagar, Z. Ghassemlooy and P. Saxena, "Mobile User Connectivity in Relay-Assisted Visible Light Communications", Sensors, vol. 18, no. 4, p. 1125, 2018. Available: 10.3390/s18041125.

98. R. Kizilirmak, O. Narmanlioglu and M. Uysal, "Relay-Assisted OFDM-Based Visible Light Communications", IEEE Transactions on Communications, vol. 63, no. 10, pp. 3765-3778, 2015. Available: 10.1109/tcomm.2015.2464815.

99. L. Feng, R. Hu, J. Wang and Y. Qian, "Deployment Issues and Performance Study in a Relay-Assisted Indoor Visible Light Communication System", IEEE Systems Journal, vol. 13, no. 1, pp. 562-570, 2019. Available: 10.1109/jsyst.2018.2869073.

100. O. Z. Alsulami, M. O. I. Musa, M. T. Alresheedi, and J. M. H. Elmirghani, “Co-existence of Micro, Pico and Atto Cells in Optical Wireless Communication,” in 2019 IEEE Conference on Standards for Communications and Networking (CSCN), 2019, pp. 1–5.

101. O. Z. Alsulami, M. O. I. Musa, M. T. Alresheedi, and J. M. H. Elmirghani, “Visible light optical data centre links,” in 2019 21st International Conference on Transparent Optical Networks (ICTON), 2019, pp. 1–5.

102. M. Safari and M. Uysal, "Relay-assisted free-space optical communication", IEEE Transactions on Wireless Communications, vol. 7, no. 12, pp. 5441-5449, 2008. Available: 10.1109/t-wc.2008.071352.

103. A. T. Hussein, M. T. Alresheedi, and J. M. H. Elmirghani, “Fast and Efficient Adaptation Techniques for Visible Light Communication Systems,” J. Opt. Commun. Netw., vol. 8, no. 6, pp. 382–397, 2016.

104. M. Schiess, E. Berglind, A. Karlsson and L. Thylen, "Pulse shape evolution and noise estimates in concatenated fiber links using analog optoelectronical repeaters", Journal of Lightwave Technology, vol. 14, no. 7, pp. 1621-1629, 1996. Available: 10.1109/50.507937.

105. P. V. Trinh, N. T. Dang, and A. T. Pham, “All-optical relaying FSO systems using EDFA combined with optical hard-limiter over atmospheric turbulence channels," J. Lightw. Technol., vol. 33, no. 19, pp. 41324144, Oct. 1, 2015.

106. J. Roch, J. Poizat and P. Grangier, "Sub-shot-noise manipulation of light using semiconductor emitters and receivers", Physical Review Letters, vol. 71, no. 13, pp. 2006-2009, 1993. Available: 10.1103/physrevlett.71.2006.

107. N. Olsson, "Lightwave systems with optical amplifiers", Journal of Lightwave Technology, vol. 7, no. 7, pp. 1071-1082, 1989. Available: 10.1109/50.29634.

108. A. T. Hussein and J. M. H. Elmirghani, “Mobile Multi-Gigabit Visible Light Communication System in Realistic Indoor Environment,” IEEE/OSA Journal of Lightwave Technology, vol. 33, no. 15, pp. 3293–3307, 2015.

109. M. T. Alresheedi and J. M. H. Elmirghani, “Hologram selection in realistic indoor optical wireless systems with angle diversity receivers,” IEEE/OSA Journal of Optical Communications and Networking, vol. 7, No. 8, pp. 797-813, 2015.

110. A. Al-Ghamdi, and J.M.H. Elmirghani, “Optimisation of a PFDR antenna in a fully diffuse OW system influenced by background noise and multipath propagation,” IEEE Transactions on Communication, vol. 51, No. 12, pp. 2103-2114, 2003.

111. A. G. Al-Ghamdi and J. M. H. Elmirghani, “Spot diffusing technique and angle diversity performance for high speed indoor diffuse infra-red wireless transmission,” IEE Proceedings Optoelectronics, vol. 151, no. 1, pp. 46–52, 2004.

112. K. L. Sterckx, J. M. H. Elmirghani, and R. A. Cryan, “Pyramidal fly-eye detection antenna for optical wireless systems,” Optical Wireless Communications. (Ref. No. 1999/128), IEE Colloq., pp. 5/1-5/6, 1999.

113. Lighting of Indoor Workplaces. (2015, Jan. 1). European Standard EN 12464-1.[Online]Available:http://www.etaplighting.com/uploadedFiles/Downloadable_documentation/documentatie/EN12464_ E_OK.pdf

114. J. Zhong, D. Chen, H. Xu, W. Zhao, J. Sun and Z. Ji, "Red-emitting CaLa4(SiO4)3O:Eu3+ phosphor with superior thermal stability and high quantum efficiency for warm w-LEDs", Journal of Alloys and Compounds, vol. 695, pp. 311-318, 2017. Available: 10.1016/j.jallcom.2016.10.211.

115. H.H. Chan, H.H., K.L. Sterckx, J.M.H. Elmirghani, and R.A. Cryan, “Performance of optical wireless OOK and PPM systems under the constraints of ambient noise and multipath dispersion,” IEEE Communications Magazine, Vol. 36, No. 12, pp. 83-87, 1998.

116. J.M.H. Elmirghani, and R.A. Cryan, "New PPM CDMA hybrid for indoor diffuse infrared channels," Electron. Lett, vol 30, No 20, pp. 1646-1647, 29 Sept. 1994.

117. Elmirghani, J., EL-GORASHI, T. and HAMMADI, A. "Passive optical-based data center networks," wO Patent App. PCT/GB2015/053,604, (2016).

118. L. Coelho, "Linearization of the product of two variables - Prof. Leandro C. Coelho, Ph.D.", Prof. Leandro C. Coelho, Ph.D., 2022. [Online]. Available: https://www.leandro-coelho.com/linearization-product-variables/. [Accessed: 12-Jan- 2022].

119. M. Lin, J. Carlsson, D. Ge, J. Shi and J. Tsai, "A Review of Piecewise Linearization Methods", Mathematical Problems in Engineering, vol. 2013, pp. 1-8, 2013. Available: 10.1155/2013/101376.

120. D. Karunatilaka, F. Zafar, V. Kalavally and R. Parthiban, "LED Based Indoor Visible Light Communications: State of the Art", IEEE Communications Surveys & Tutorials, vol. 17, no. 3, pp. 1649-1678, 2015. Available: 10.1109/comst.2015.2417576.

121. H. Marshoud, V. Kapinas, G. Karagiannidis and S. Muhaidat, "Non-Orthogonal Multiple Access for Visible Light Communications", IEEE Photonics Technology Letters, vol. 28, no. 1, pp. 51-54, 2016. Available: 10.1109/lpt.2015.2479600.

122. H. Marshoud, P. Sofotasios, S. Muhaidat, G. Karagiannidis and B. Sharif, "On the Performance of Visible Light Communication Systems with Non-Orthogonal Multiple Access", IEEE Transactions on Wireless Communications, vol. 16, no. 10, pp. 6350-6364, 2017. Available: 10.1109/twc.2017.2722441.

123. R. C. Kizilirmak, C. R. Rowell, and M. Uysal, “Non-orthogonal multiple access (NOMA) for indoor visible light communications,” in Proc. 4th International Workshop on Optical Wireless Communications (IWOW), Sep. 2015, pp. 98–101.

124. V. Dixit and A. Kumar, "An exact BER analysis of NOMA-VLC system with imperfect SIC and CSI", AEU - International Journal of Electronics and Communications, vol. 138, p. 153864, 2021. Available: 10.1016/j.aeue.2021.153864.

125. A. A. M. Hassan, A. A. Qidan, M. K. Aljohani, T. E. H. El-Gorashi, and J. M. H. Elmirghani, ‘‘Random linear network coding in NOMA optical wireless networks,’’ 2022, arXiv:2202.04123.

126. C. Chen, W. Zhong, H. Yang, P. Du and Y. Yang, "Flexible-Rate SIC-Free NOMA for Downlink VLC Based on Constellation Partitioning Coding", IEEE Wireless Communications Letters, vol. 8, no. 2, pp. 568-571, 2019. Available: 10.1109/lwc.2018.2879924.

127. H. Li, Z. Huang, Y. Xiao, S. Zhan and Y. Ji, "Solution for error propagation in a NOMA-based VLC network: symmetric superposition coding", Optics Express, vol. 25, no. 24, p. 29856, 2017. Available: 10.1364/oe.25.029856.

128. S. Ma, Y. He, H. Li, S. Lu, F. Zhang and S. Li, "Optimal Power Allocation for Mobile Users in Non-Orthogonal Multiple Access Visible Light Communication Networks", IEEE Transactions on Communications, vol. 67, no. 3, pp. 2233-2244, 2019. Available: 10.1109/tcomm.2018.2885352.

129. M. Janjua, D. da Costa and H. Arslan, "User Pairing and Power Allocation Strategies for 3D VLC-NOMA Systems", IEEE Wireless Communications Letters, vol. 9, no. 6, pp. 866-870, 2020. Available: 10.1109/lwc.2020.2973628.

130. B. Lin, Q. Lai, Z. Ghassemlooy and X. Tang, "A Machine Learning Based Signal Demodulator in NOMA-VLC", Journal of Lightwave Technology, vol. 39, no. 10, pp. 3081-3087, 2021. Available: 10.1109/jlt.2021.3058591.

131. M. T. Alresheedi, A. T. Hussein, and J. M. H. Elmirghani, “Uplink design in VLC systems with IR sources and beam steering,” IET Communications, vol. 11, no. 3, pp. 311–317, 2017.

132. J. Lindle, A. Watnik and V. Cassella, "Efficient multibeam large-angle nonmechanical laser beam steering from computer-generated holograms rendered on a liquid crystal spatial light modulator", Applied Optics, vol. 55, no. 16, p. 4336, 2016. Available: 10.1364/ao.55.004336.

133. A. Gomez, K. Shi, C. Quintana, G. Faulkner, B. Thomsen and D. O'Brien, "A 50 Gb/s Transparent Indoor Optical Wireless Communications Link With an Integrated Localization and Tracking System", Journal of Lightwave Technology, vol. 34, no. 10, pp. 2510-2517, 2016. Available: 10.1109/jlt.2016.2542158.

134. S. Kim and S. Kim, "Wireless visible light communication technology using optical beamforming", Optical Engineering, vol. 52, no. 10, p. 106101, 2013. Available: 10.1117/1.oe.52.10.106101.

135. K. Van Acoleyen, W. Bogaerts and R. Baets, "Two-Dimensional Dispersive Off-Chip Beam Scanner Fabricated on Silicon-On-Insulator", IEEE Photonics Technology Letters, vol. 23, no. 17, pp. 1270-1272, 2011. Available: 10.1109/lpt.2011.2159785.

136. A. Gomez et al., "Beyond 100-Gb/s Indoor Wide Field-of-View Optical Wireless Communications", IEEE Photonics Technology Letters, vol. 27, no. 4, pp. 367-370, 2015. Available: 10.1109/lpt.2014.2374995.

137. D. Halliday, R. Resnick and J. Walker, Fundamentals of physics. Milton: John Wiley, 2020.

138. J. Jahns and S. Walker, "Two-dimensional array of diffractive microlenses fabricated by thin film deposition", Applied Optics, vol. 29, no. 7, p. 931, 1990. Available: 10.1364/ao.29.000931.

139. D. Bolkas and A. Martinez, "Effect of target color and scanning geometry on terrestrial LiDAR point-cloud noise and plane fitting", Journal of Applied Geodesy, vol. 12, no. 1, pp. 109-127, 2018. Available: 10.1515/jag-2017-0034.

140. D. Kolev, K. Wakamori and M. Matsumoto, "Transmission Analysis of OFDM-Based Services Over Line-of-Sight Indoor Infrared Laser Wireless Links", Journal of Lightwave Technology, vol. 30, no. 23, pp. 3727-3735, 2012. Available: 10.1109/jlt.2012.2227456.

141. H. Xu, B. Davey, D. Timothy, D.Wilkinson, andW. A. Crossland, “Optically enhancing the small electro-optical effect of a fast-switching liquid crystal mixture,” Opt. Eng., vol. 39, no. 6, pp. 1568–1572, Jun. 2000.

142. E. Almohimmah and M. Alresheedi, "Error Analysis of NOMA-Based VLC Systems With Higher Order Modulation Schemes", *IEEE Access*, vol. 8, pp. 2792-2803, 2020. Available: 10.1109/access.2019.2962331.